SJOEM, the Simple Jacket Optimization Engineering Model

J. Antonissen

Delft University of Technology

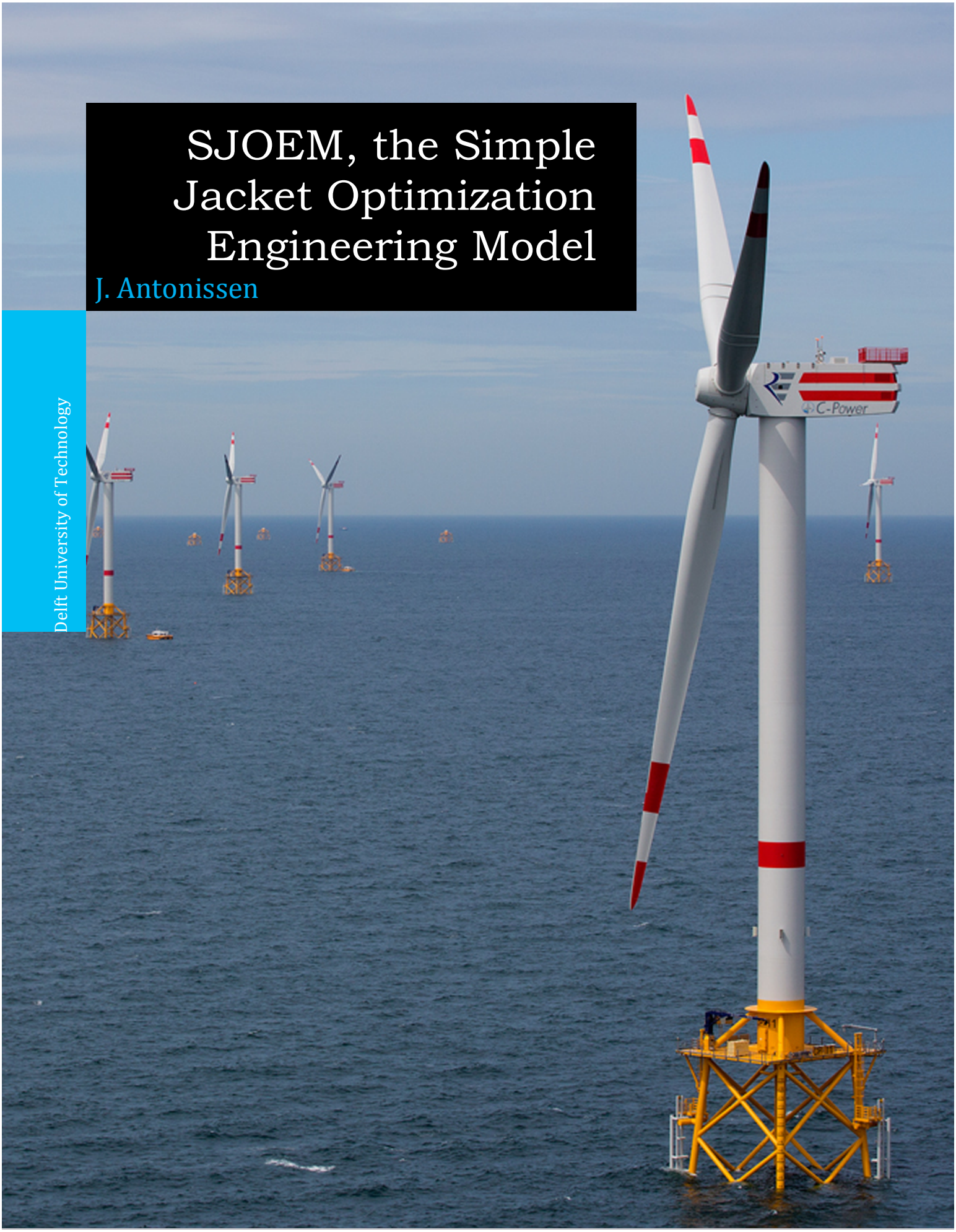

TU Delft Delft University of Technology

Challenge the future

Front-page image licensed to RWE

SJOEM, the Simple Jacket Optimization Engineering Model

A small tool to assist with large decisions

By

J. Antonissen

in partial fulfilment of the requirements for the degree of

Master of Science
in Applied Physics

at the Delft University of Technology,
to be defended publicly on Tuesday December 21, 2015 at 02:00 PM.

Supervisor:	Dr. M.Zaayer	TU Delft (AE)
Thesis committee:	Prof. Dr. G. van Bussel,	TU Delft (AE)
	Dr. M.Zaayer,	TU Delft (AE)
	Dr. E.Lourens	TU Delft (OE)

TU Delft Delft University of Technology

For my grandfather,

Foreword

Back in 2002, my interest for sustainable energy was ignited while listening to my all-time favorite album 'Geogaddi':

> *'Energy is becoming one of our country's greatest concerns. If we don't start working on energy conservation, there may not be enough energy to go around by the time I'm a parent. We're going to learn about how we can solve some of our problems through alternative energy sources. You can learn more about energy too. Call your county cooperative extension service for more information. Conserving energy is everyone's responsibility. Call 4H to find out how you can do your part.'* - Boards of Canada, Energy Warning

This text got me thinking; what is global warming?, is it really that dangerous?, can I be of any help to make the world a better place? Obviously the only logical path to answer these questions was trough education.

Therefore, after I completed my bachelor degree in mechanical engineering at the HRO, I started the master Sustainable Energy Technology (SET) at the TU Delft. Little did I know then, but this master completely changed my perception of the world. Starting this master degree has been the best choice I have ever made in my life.

This thesis is the fruit of five years of hardships. Times have been rough; often I have thought that I wasn't able to make it, that I wasn't intelligent enough. But I did it! And it was totally worth it.

The only thing that's left is wishing you, the reader, a pleasant journey. I invite you in the wonderful world offshore wind. This sustainable energy source is in my personal opinion the beacon of light that will show us the way out of the Dark Age of fossil fuel.

Let's put our heads together and become a Type I Kardashev civilization[1] as soon as possible!

2015, Johan Antonissen

[1] Type I Kardashev civilization: A civilization that is able to harvest all it's required energy from sustainable energy sources on it's own planet.

Executive summary

One of the main drawbacks of offshore wind energy is its high levelized cost of electricity (LCOE). One explanation for these high costs arises from the large amount of uncertainties that come with such complex projects. As a result of this complexity, it's difficult to foresee the course of events in advance. Decisions made during the preliminary design phase are often based on limited data while having a great impact on project outcome. A tool is needed to assist engineers during these early stages of design. This tool should deliver good results using limited input data and require little computational time. An example of such a tool is TeamPlay; an engineering model that evaluates offshore wind farm design using automated optimization techniques. In its current state, only a monopile type foundation is analyzed within this process. Since the current trend in the industry is to build larger farms further from shore, this foundation type will become less popular in the future. A jacket type foundation is better suited for far-shore application. In this thesis, a new stand-alone engineering model is created which can be added to TeamPlay's functionality to extend future use. The following goal is set:

Design of a simple and fast jacket optimization tool that aids offshore wind farm engineers with their decision making process of the preliminary design phase when only limited data is available.

This objective is tackled by engaging in three sub-tasks, after which conclusions are drawn and recommendations are made. First, the design process of the monopile and jacket foundation structure is submitted to a background analysis. Since automated optimization is, at the time being, not a part of the design process in practice, only a static design process is treated. The complex process of offshore support structure design is explicated by analyzing the following design steps: environmental data assessment, turbine selection procedure, design elevation estimation, natural frequency constrain evaluation, and lastly a support structure stress assessment where yield, buckling, fatigue and stress concentrations are taken into account. Furthermore, due to close resemblance with oil and gas space-frame structures, several rules of thumb are adopted from literature surrounding this topic.

After gaining this insight in support structure design, the engineering model is given a closer look. This model, which carries the name 'SJOEM' for Simple Jacket Optimization Engineering Model, is built on the foundations of the background analysis. At this point the concept of automated design optimization is introduced. Since structure cost is directly related to amount of material used, an optimum is found for the lowest structure volume to withstand each of three design load cases (DLC). These represent likely to occur extreme weather scenarios and are created from several of the 18 required model input parameters. Once load cases are assigned, the first physical representation of the structure is found by addressing design elevations. Then, using a four-step process, structure geometry is determined from top to bottom. Firstly, rotor nacelle assembly (RNA) loads are found. These loads are approximated by Blade Element Momentum (BEM) or drag theory, depending on the DLC in question.

Second, focus is put on tower geometry. Minimal tower volume is found by estimation of minimal cross-sectional areas for several locations along its height. Tower height itself is found as a function of the rotor diameter. Areas are estimated in an iterative manner by balancing drag and gravitation induced loads with internal stresses. This equilibrium is found by means of yield-, local- and global buckling- analysis and lastly a diameter over wall thickness penalty constraint. Implementation of this penalty constraint is required to restrain diameter size. This way geometry conforms more closely with practice. It is found that sole usage of buckling and yield constraints, based on current standards, are not suited for automated design. Especially buckling constraints are only useful for quick design checks rather than being design drivers.

For the third design phase, loads obtained from the tower assessment are combined with wave activity to address jacket geometry. Hydrodynamic loads are estimated iteratively using the Morison equation. Particle movement for the Morison equation is estimated using Airy wave theory. For each DLC, loads are determined for two inflow scenarios where wind and wave propagation is assumed uni-directional. For each bay, leg batter and brace angle are taken as equal and constant. Unfortunately, assuming leg batter as constant throughout the structure resulted in a lesser number of bays than is observed in practice. In order to address wave loading in a simple manner, bay members are combined into a single vertical pile. This single pile's geometry is taken such that it is exposed to equal wave loads. Then, using simple statics relations, these external loads are subdivided over nodes located at member edges. Internal member loads are found by balancing external loads for each

node located in two horizontal cross-sectional planes for each bay. For the fist plane, forces at a respective bay top are simply balanced with those aligned with the member's direction. For the second plane, which is located at the bottom of a bay, redistribution of loads is estimated from reactive loads. Reactive loads are found by calculating the difference between internal member loads from bay top with external loads at the bottom. To yield more accurate results, this load difference is incorporated in load assessment for following bays. Furthermore, as suggested by literature, bays are evaluated as being two dimensional rather than three dimensional. This simplification turned out to be the main source of error in the engineering model, for reasons that will become clear in the next paragraph. For each bay, optimal brace and leg geometry is estimated from equilibrium conditions for which the yield and both local and global buckling conditions are met. Unfortunately, a penalty limit is added again to push the design optimum towards reasonable values. Finally, Efthymiou theory is consulted to take into account failure as a result of stress concentrations. Using this theory, local increased member wall thicknesses are determined such that these failure modes do not occur.

Pile design marks SJOEM's final design phase. For each of the four foundation piles, minimal volume is estimated by balancing pile top loads with soil interaction. Top loads are obtained from jacket bottom base shear, overturning moment and load contribution from weight. Pile geometry is estimated in a two-phase process, each having two design constraints. For the first phase, optimal pile cross-sectional area is found at the equilibrium between yield stress and minimum required wall thickness to prevent buckling during pile driving. Second, the optimum area serves as input to find out required pile length for which axial and lateral soil resistance conditions are met.

In an attempt to show SJOEM's wide range of capabilities, three sample points are reviewed in the thesis's penultimate chapter. These represent possible sites ranging from light to extreme. Sample point 'Princes Amalia' marks the gentlest one. Its parameters are adopted from the existing farm located not far from the Dutch shoreline. A moderate sea and wind climate and low water depth mark the core attributes of this offshore wind farm, named after our King's firstborn. A somewhat rougher environment is found at the German farm 'Alpha Ventus'. This patch of sea provides a higher energy yield, but at the cost of greater structure loads. For the third farm 'SJOEM', an imaginary site is evaluated. This site is located in a very hostile environment in the outermost Northwest part of the Dutch territory. This farm is marked by extreme water depth, high wind speeds and violent wave patterns. Once sample points are established, the engineering model is put to the test. Optimal structure geometry is evaluated for each of the three sites. Internal and external load distributions are given and compared, and results are discussed.

Once results for each sample point are established, the engineering model's validity is checked by comparison to two ANSYS models. For the first model, the same set of assumptions as used for SJOEM is adopted. A three-dimensional model is constructed using truss elements. By merely placing loads at nodes located at member edges and letting joints in these edges rotate freely, an exact representation of the engineering model is achieved. One in which, analogous with SJOEM, only axial loads can form. Comparison of results shows a margin of error of about 6% per bay. However, an accumulative effect is observed resulting in a large increase in total error for jackets having multiple bays. The error is found to be the result of simplifications made to represent the space frame in two dimensions rather than three. As a result of taking small angles as being straight, an error is introduced in the load distribution between legs and braces. This accumulated effect arises due to load coupling by taking into account load relocation from reaction loads. Obviously, not taking reaction loads into account would result in an even greater error. For the second ANSYS model, a core model assumption is verified. For this second case, joint connections are taken as rigid rather than allowing them to rotate freely. By taking joint connections as rigid, formation of non-axial loads is allowed. Comparing results showed a small difference in member stresses. This difference is the result of the second model's greater accuracy compared to the model equipped with loose joints. Namely, for trusses only a single average cross section stress can be found. On the other hand, for the second ANSYS model on the other hand, a stress distribution is observed since non-axial loads can propagate here as well. When the average of this stress distribution is used, the same stress as for the truss elements is found. Thus, when using trusses with free rotation joint connection, only a loss of model precision is observed while the accuracy of results stays the same.

The research goal is fulfilled; a simple automated optimization engineering model is created. Main recommendations include; taking caution when copying rules of thumb from the oil and gas industry and paying attention to the impact of simplifications, especially when it comes to assuming small angles as being straight.

Table of contents

1

Introduction

Since 1990, with the completion of the 220 kW Norgensund turbine in Sweden, offshore wind energy has been in a slow but steady rise towards becoming a major part of the global renewable energy movement. In 1994 the Dutch company Lely commissioned the first offshore wind farm (OWF) consisting of 4 small 500 kW turbines located 750 meter of the coast of Medemblik (Noord-Holland). Since then, 6.6 Giga Watt has been installed in Europe providing a slight 0,7% of the European electricity demand (EWEA 2013). Nonetheless, offshore wind is up and coming. Currently, the rate of annually installed offshore energy grows much faster as that of onshore wind (Figure 1. 1). This number should, according to EU regulations, increase to a staggering 150 GW installed capacity by 2030 (EWEA 2014).

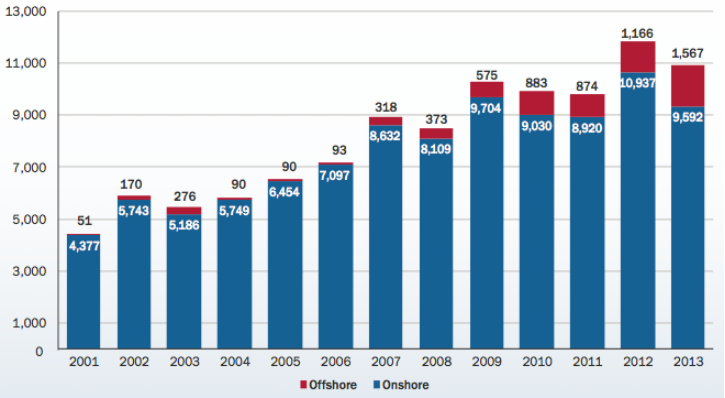

Figure 1. 1 – Annual onshore and offshore installed capacity [MW] (Ref: EWEA)

One of the major bottlenecks in offshore wind energy is its high price of energy compared to other renewables. A study by Fraunhofer ISE (FraunhoferISE 2012) on the 'levelized cost of energy' (LCOE) showed that offshore wind is, for the time being, the most costly way of generating electricity apart from biomass (Figure 1. 2). The LCOE is an often-used benchmark for fair comparison of energy sources. It represents the cost of electricity in price per unit energy, encompassing various factors such as initial capital, discount rate, continuity of operation, and fuel and maintenance cost.

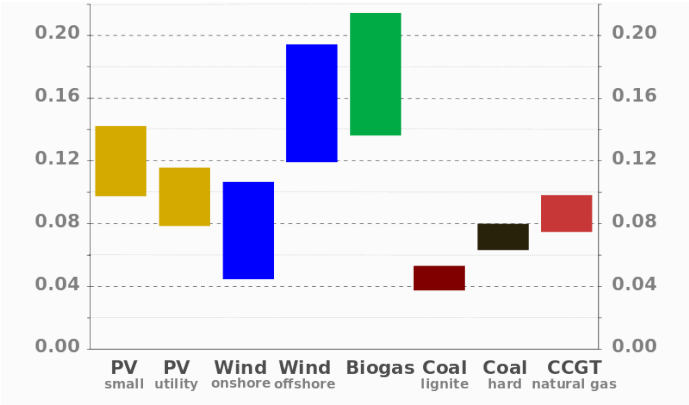

Figure 1. 2 - LCOE in euro/kWH (Ref: Faunhover ISE)

One solution for reducing offshore wind energy costs is found by streamlining the preliminary design phase. Specifically, decisions made during this design phase have a large impact on the course of the project but are often based on limited available data. If these decisions prove to be flawed, they can result in large additional unforeseen project costs. Furthermore, these early decisions often lay at the core of the project and are therefore difficult to rewind.

Offshore engineers need a tool that helps them evaluate the outcome of certain decisions that lie at the basis of the preliminary design phase. This tool should deliver detailed information using limited input data and require a small amount of computational time. Currently, two types of programs exist in the industry that could fulfill such a role. The first one uses the finite element method (FEM) to determine structure stresses from given boundary conditions. One example is the engineering software ANSYS. However, since ANSYS is not designed specifically for the offshore wind industry, extensive understanding of the field is needed in order to create a model that correctly describes reality. Furthermore, since ANSYS is a tool with a vast amount of capabilities, a large set of input data is needed and a lot of computational time is required before accurate results are obtained. Since time and resources are often scarce in the preliminary design phase, using ANSYS at this design stage would be like shooting a mosquito with a cannon. The second, more tailored, program type is an aeroelastic code such as BLADED. These programs are designed specifically for the wind industry and are able to provide results in a decent amount of time. However, while requiring less input data than FEM software, aeroelastic code does still require quite a large set of input parameters. A further disadvantage, which is true for both types of software, is that engineers still need to update input data after each design loop. This way numerous design loops are required before a design optimum is found. Since the engineer needs to intervene after each design loop, the process becomes very labor intensive and time consuming. In order to unburden the engineer, an automated design tool is needed that delivers quick results of decent accuracy (Muskulus 2014).

In contrast to the aerospace industry, automated design optimization is relatively new in the offshore wind industry. These types of optimization techniques involve non-linear programming problems and are often solved iteratively using sequential least square programming techniques. One of the few existing design optimization tools used especially for the offshore wind industry is TeamPlay. This model's engineering algorithm evaluates optimal wind farm design, ranging from offshore structure to park layout, and requires a limited set of input parameters. In its current state TeamPlay's automated optimization design addresses blades, rotor nacelle assembly (RNA), tower and a monopile type foundation. Since structure cost is directly related to material use, an optimal design configuration is found when the least material is used (Zaaijer 2013). The goal of this thesis is to create a stand-alone engineering model in which an additional support-structure is evaluated. In the future, this model can be added to TeamPlay to extend its current capabilities.

Figure 1. 3 shows the current state of development of the offshore market according to the European Wind Energy Association (EWEA 2013). Closer inspection of the chart shows that the monopile is by far the most used support structure, both in terms of accumulated and newly installed foundation structures. However, a difference arises when the second most favorable structure is given a closer look. In terms of currently existing support structures, a gravity based foundation (GBF) is the second most popular support structure. The foundation is, however, the least popular when it comes to being future proof. Namely, the GBF comes in last when ranked for newly installed capacity, where a jacket foundation comes first place.

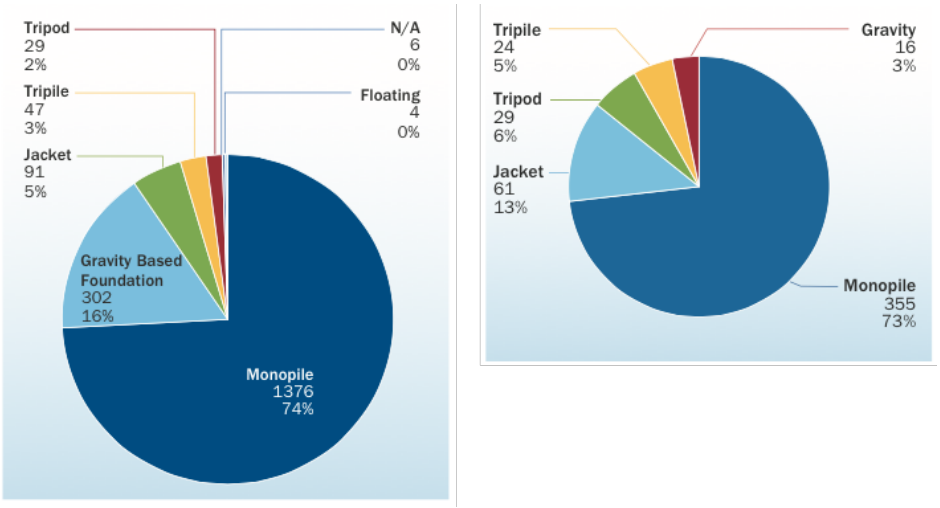

Figure 1. 3 - Support structure market share as of end 2012.
Left: Accumulated capacity, right: Newly installed capacity. (Ref: EWEA)

This large difference is explained by taking a closer look at market trends (Figure 1. 4). The European offshore wind market (and quite possible the global offshore wind energy market) is developing according to 'Texan' standards. Its size is continuously increasing along all facets of the market; turbines, larger farms, water depths and distance from shore. This is seen when average depth and distance from shore from online and under construction farms are compared to those of consented farms. The blue arrow in the figure emphasizes this effect. Since GBF structures are only suited for near-shore applications it follows that support structures of the jacket type are the most future proof.

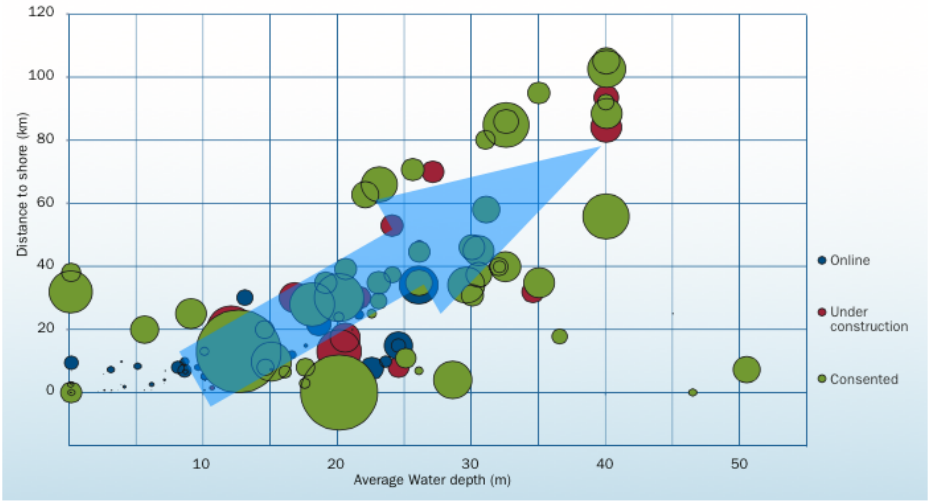

Figure 1. 4 - Market trends: Distance vs. depth (Ref: EWEA)

Taking the above into account, the following research goal was formed:

Design of a simple and fast jacket optimization tool that aids offshore wind farm engineers with their decision making process in the preliminary design phase when only limited data is available.

This research goal is addressed along the course of three chapters after which conclusions are drawn and recommendations are made. Firstly, the background of support structure design is given a closer look. This is done by means of going through the current design process for a monopile and jacket foundation structure. A static design process is conducted since automated design optimization is, at the time being, not used in practice. Both the monopile and jacket design processes are discussed to emphasize similarities of design procedures. By extensively treating the design process in advance, a deeper insight in engineering methods is granted. This should help the reader (and writer) distinguish a clearer distinction between important and less-important mechanics, thus resulting in a more clearly delineated model. As a final note concerning this chapter, since the discussed material is rather extensive, readers experienced with the topic could choose to skip it. Second, once a clear understanding of support structure design is achieved, focus is pointed towards SJOEM; the Simple Jacket Optimization Engineering Model. The model design is discussed along the pathway of structure design as followed by SJOEM's engineering algorithm; RNA, tower, support structure and foundation piles. Furthermore, since at this point automated design optimization becomes part of the design process, a detailed example of this procedure is given. Analogous to TeamPlay, for SJOEM the optimal design configuration is found for the lowest volume structure that is able to withstand likely to occur extreme weather scenarios. In the fore last chapter, the engineering model is put to the test and results are compared to two ANSYS models. In one of these the same set of assumptions is incorporated in the FEM model while for the other one correctness of core simplifications is given a closer look. By doing so two conclusions are drawn surrounding the model's correctness. Insight in margin of error is granted, while the validity of the simplifications that lay at its core is exposed. In the closing chapter of this thesis conclusions are drawn and recommendations are made.

2

Background

2.1 Introduction

In this chapter, a detailed breakdown of the jacket and monopile design process is discussed. In a first attempt to clarify support structure design, focus is put on the design process as if it where in practice. Emphasis is put on design procedures similarities between the jacket and monopile. Comparison between both structures is desired since at a certain point in the preliminary design phase jacket loads are estimated using an equivalent monopile structure. Furthermore, since this thesis revolves around assisting engineers in the preliminary design phase, the larger part of the discussion of this chapter revolves around this design phase as well. As a final note, in the current chapter the basics of offshore structure design are discussed. Since no new theory is discussed, the reader experienced with this topic can proceed to chapter three.

2.2 General design procedure

The general process for designing an offshore wind support structure is displayed in Figure 2. 1. Most often, these structures are not created from scratch but are rather by modification of existing designs. The design consists of two phases, the preliminary design and a detailed design phase. Firstly, in the preliminary design phase the structure's rough dimensions are estimated using simple calculations. Once the stress check step of the preliminary design phase is finished a more detailed model is constructed in specialized software, these models give insight in design interactions between the different parts of the structure (RNA, tower, substructure and foundation piles). The model is subjected to more detailed design steps along the course of the detailed design phase, which results in a design that better fits requirements. Multiple iterative loops are executed during the detailed design process to make sure changes in the design still converge with previous design steps. This iterative process is shown in the figure using feedback loops labeled 'not ok'.

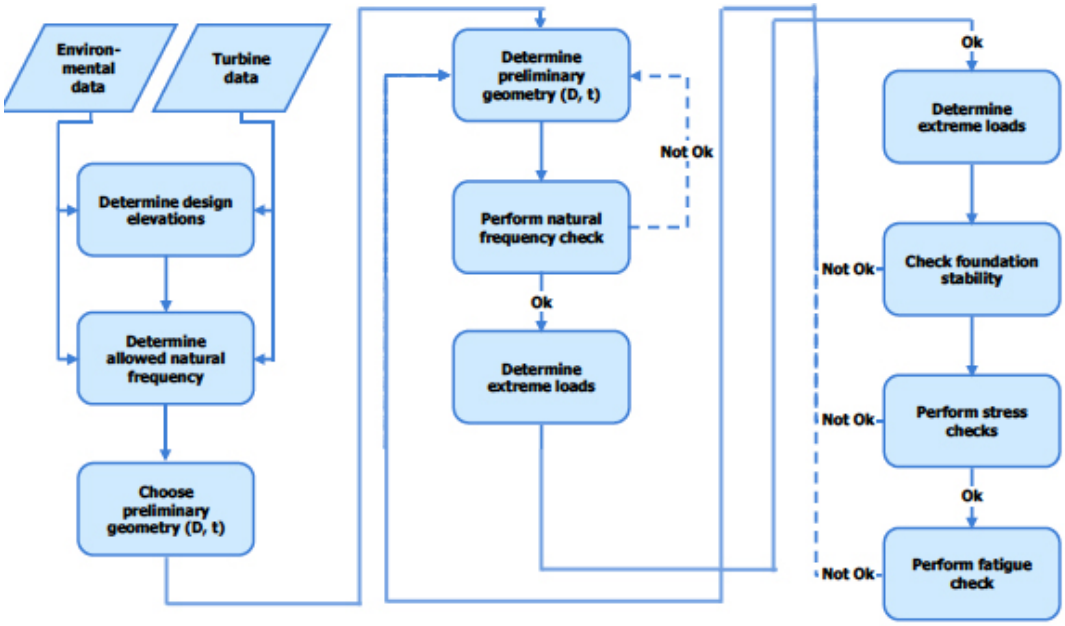

Figure 2. 1 - General design process in practice

2.3 Site selection

For the first step in the design process focus is put on selecting a suited site. This process is a get-together of requirements from internal and external stakeholders. Internal requirements are set by the park designer's own demands and wishes. These are generally set to achieve the highest 'bang for buck' or, in more general terms, the largest amount of produced energy for the least possible effort. Generally speaking, high winds accompanied with low hydrodynamic activity, low water depth, good soil properties and a negligible distance to shore are preferred environmental conditions for the park to achieve the most cost effective design. Additionally, market trends indicate that increasing the size of wind farms also proves to be helpful in reducing its cost per kilowatt-hour. Governmental institutions most often set external requirements in the form of rules and regulations. Their main goal is mostly preventing destruction mainly preserving nature and protecting wildlife. Additionally, companies can also enforce external requirements. A good example is seen in Oil and Gas firms in the North Sea, these rather not see wind farms being built near their platforms since these could interfere with their production of fossil fuel.

2.3.1 Environmental data

After the location of the site is determined, a more extensive examination of site properties is conducted. This data can be found by extrapolation of existing data or measuring. The most detailed information is acquired using on-site measurements done by meteomasts. These masts acquire information such as wind speed and direction, temperature and atmospheric saltiness. From this data Weibull diagrams, wind roses, turbulence intensities, wind profile (shear), gusts and extreme wind scenarios are created. Additionally measuring buoys, among others, gather information of current speed and direction, wave data, and water levels. The masts and buoys however, only provide short-term information since these only measure for as long as they're operational. Therefore measured data is compared with existing data from computer models to gain a more detailed insight in long-term weather effects. This process is, for example, used to compute 50-year extreme wind speeds, which are used to estimate ultimate stress scenarios that occur during 'extreme load cases'. In addition, soil data is obtained from borehole measurement tests such as cone penetration tests (CPT). Important soil parameters include: density/plasticity, skin friction, internal angle of friction, end-bearing pressure, peak strain and module of subgrade reaction. This data helps to model the soil as a system of springs to evaluate soil stability.

Wind

Wind characteristics are best explained using a wind energy spectrum of Figure 2. 2. Here the horizontal axis represents the return period of certain wind types and the vertical axis represents the amount of energy contained in the respective wind type (in m^2/s^2). The left hand side (from the blue line) of the image indicates the mesometeorological range. This range represents annual weather changes due to differences of irradiation from the sun plus (multi-) daily changes due to changing pressure in the atmosphere. Short-term effects are contained within the micrometeorological (turbulent) range. This spectrum reaches from approximately ten minutes to a second. Here solid line in the micrometeorological range represents turbulence for strong winds while the dashed line represents this for weaker wind speeds. Since weather is varies by location, wind energy spectra are site specific. From energy yield calculations are made from long data while short-term weather data is used for load calculations (Tempel 2006).

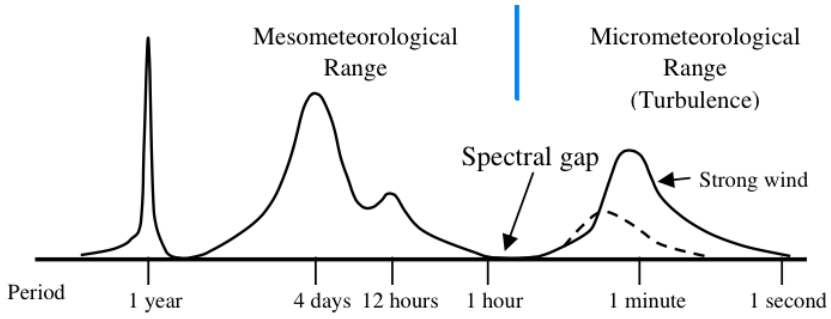

Figure 2. 2 - Wind energy spectrum

Energy yield calculations are made using the mesometeorological energy spectrum. These calculations are however made using a different type of cure; the Weibull distribution. In wind energy, curve is created using either hourly or 10-minute average wind speed data (e.q.(2.1)). Figure 2. 3 shows three typical Weibull distributions for onshore, coastal and offshore locations where k and A are the (dimensionless) shape and scaling factor, respectively.

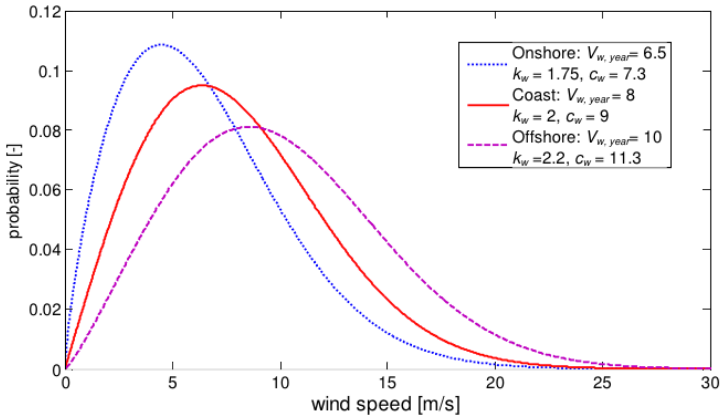

Figure 2. 3 - Weibull distributions

This shape factor represents an estimation of the average 'roughness' of the site's weather. For example, the shape factor for the OWEZ wind farm, located 18 km from the Dutch shore, is measured to be 2,35 at a elevation of 116 meter from sea level (Donkers 2010). The scaling factor is related to the site's annual wind speed and is found using the average wind speed and the shape factor (e.q.:(2.2)). For the OWEZ wind farm the shape factor is measured to be 11,68 for the same elevation.

$$f(v_i) = \frac{k}{A}\left(\frac{V}{A}\right)^{k-1} \cdot \exp\left(-\left(\frac{V}{A}\right)^{k}\right) \tag{2.1}$$

$$A = \frac{V_{mean}}{\Gamma\left(1+\frac{1}{k}\right)} \tag{2.2}$$

Additionally, the average wind speed (V_{mean}) is can be approximated using shape and scaling factor in the following approximation proposed by Lysen (Bendat and Piersol 1980):

$$V_{mean}[m/s] = A \cdot \left(0{,}568 + \frac{0{,}433}{k}\right)^{-k} \tag{2.3}$$

Micrometeorological information of the wind energy spectrum helps establish stresses in the structure. Wind speeds can locally and temporarily change with a factor of two or three as a result of Turbulence. These rapid changes in wind speed have dramatic effects on the (periodical) loading of the structure. Obviously, areas with fewer (or smaller) obstructions have in less turbulence.

The dimensionless 'turbulence intensity' factor is used for comparing wind speed with rapid changes due to turbulence. This factor is the ratio between the turbulence σ (m/s) and the average wind speed V (m/s) (e.q:(2.4)).

$$TI = \frac{\sigma}{V} \tag{2.4}$$

Most often, wind speed measurements are however only available in 10-minute intervals, these measurements are thus unable to provide information on turbulence. Several institutions have therefore created guidelines for estimating turbulence intensity as a function of average wind speed.

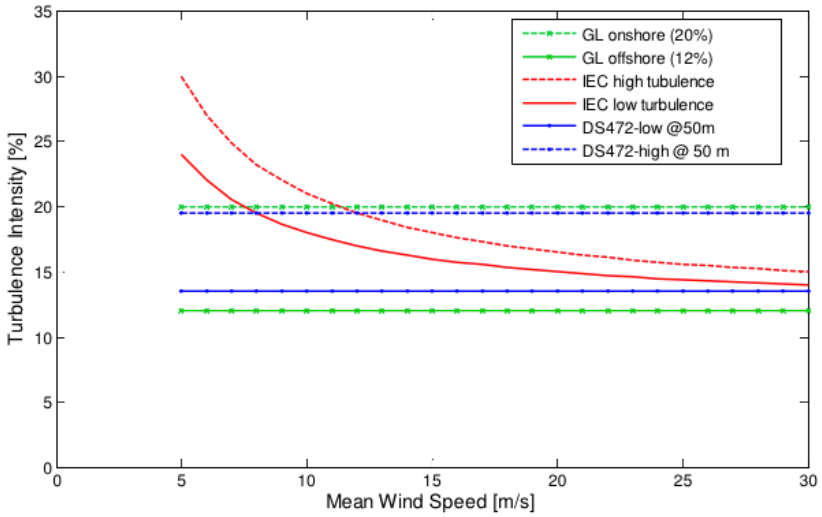

Figure 2. 4 - Turbulence intensity

In an effort to predict extreme weather, extreme winds and gusts with a return period of 50 or even 100 years are also given a closer look. This data can however often not be extrapolated from measurements but is rather predicted from short-term data using a Gumbel approximation. An example of such a curve is depicted in Figure 2. 5. Here black lines indicate the actually measured data and the red line shows the fitted Gumbel approximation. The resulting extreme weather conditions are used as input for ultimate load cases to find out the ultimate stresses (ULS) that would occur during extreme storm events.

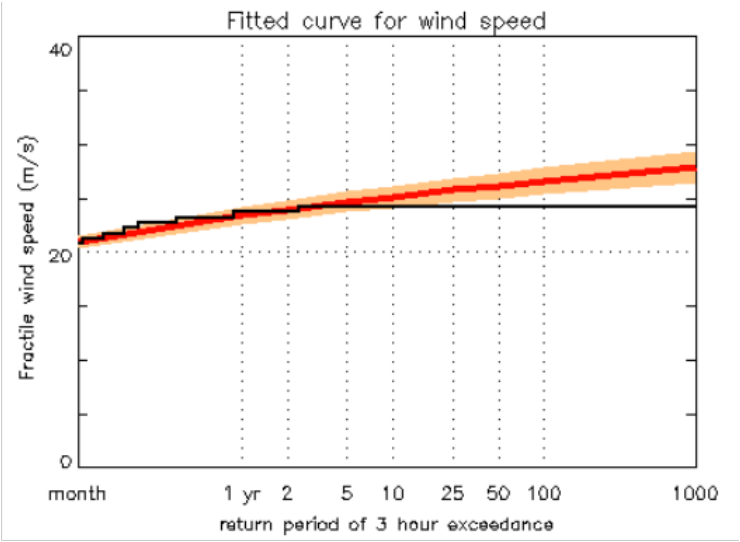

Figure 2. 5 - Gumbel approximation (red) of measured data (back)

One final parameter is still desired to estimate difference in wind speed loads due to change in elevation; wind shear. Wind shear is the increase in wind speed when one moves away from earth's surface, where wind speed is zero, up until the Ekman layer where wind speeds are constant. This layer, located about 100 meters from the mean sea level (MSL) is characterized by only having changes in wind direction instead of also having changing wind speeds. Wind shear profiles are hugely affected by surface roughness (Z_0). Typical values for surface roughness reach from a minimum at offshore locations of 0,0002 m to 1 m in urban environments which contain a lot of irregularities such as flats and high trees. Equation (2.5) gives the wind profile function as a function of height. Here V_{Ekman} and h_{Ekman} are the wind speed and height at the Ekman layer, respectively.

$$v(h)[m/s] = V_{Ekman}(h_{ref}) \cdot \frac{\ln(h/z_o)}{\ln(h_{ref}/z_o)} \tag{2.5}$$

Figure 2. 6 shows the large difference between several wind speed profiles for urban and offshore areas as a result of different surface roughnesses.

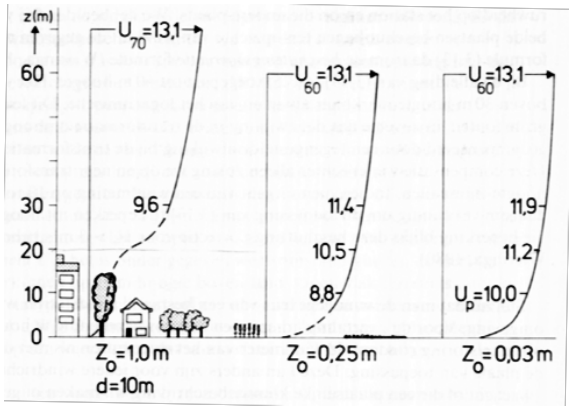

Figure 2. 6 - Wind shear

As a final note, wind shear can also be represented using a power law (e.q.:(2.6)). Here α_{shear} is the wind shear exponent, which is typically taken as 0,12 for calm sea (Donkers 2010).

$$v(h)[m/s] = V(h_{ref}) \cdot \left(\frac{h}{h_{ref}} \right)^{\alpha_{shear}} \tag{2.6}$$

Waves

Moving down from the top of the structure, the interface between air and water is reached. Ocean waves are formed from the friction between are particles and water as the exchange kinetic energy. Even though waves seem chaotic by nature, they are the result of several combined orderly processes. However, before these processes are discussed, a closer look in wave spectra is required.

Water levels are measured with the MSL as reference point. An example of wave elevation time series as recorded by a measuring buoy is depicted at the top of Figure 2. 7. From this data several parameters are extracted. Firstly, significant wave height (H_s), is the mean of the one-third highest measured values. Thus, if a measurement contains 10 waves, the significant wave height is the mean value of the highest three waves. Second, the mean-zero crossing period (T_z) is obtained from the time series by dividing the measurement time (here 200 s) over the number of zero-crossings with the MSL.

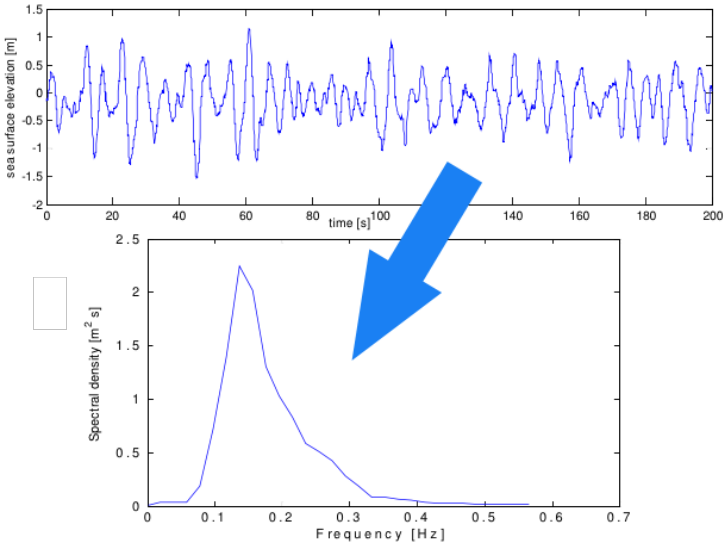

Figure 2. 7 - Water level in time domain (top) and frequency domain (bottom)

Time series however, remain difficult to interpret by just looking at it. A more convenient way of showing this information is obtained by converting these series to the frequency domain using a Laplace operator. The bottom part of Figure 2. 7 depicts the time domain measurement mapped to the frequency domain. When the wave pattern is 'fully developed' it can be approximated using the Pierson-Moskowitz (PM) spectrum. When this is the case, the spectrum can be approximated only with the significant wave height (H_s) and zero-crossing time (T_z) as a required input (e.q.:(2.7)). A wave pattern is fully developed when wave motion has come in equilibrium with a constant wind speed. A final noteworthy value in the PM spectrum is the peak frequency (T_p), which is located at $(1{,}41 \times T_z)^{-1}$ Hz.

$$S_{PM}(f) = \frac{H_s^2}{4 \cdot \pi \cdot T_z^4 \cdot f^5} \cdot \exp\left(-\frac{1}{\pi}(f \cdot T_z)^{-4}\right) \tag{2.7}$$

Once the waves are extrapolated to a clearer function using PM, the spectrum is converted back to sinusoids (in the time domain) to serve as an input for the well-known Morison equation to establish wave loads. Firstly, sinusoids are created using frequency and amplitude extracted from the PM spectrum. Wave particle kinematics for a fully developed (linear) flow are depicted in equation (2.8) for particle speed and (2.9) for particle acceleration. These are equations are referred to as Airy linear wave theory.

$$u(x,z;t)[m] = \zeta \cdot 2 \cdot \pi \cdot f \cdot \frac{\cosh(k_{wave}(z+d))}{\sinh(k_{wave} \cdot d)} \cdot \cos(k_{wave} \cdot x - 2 \cdot \pi \cdot f \cdot t) \tag{2.8}$$

$$\dot{u}(x,z;t)[m/s] = \zeta \cdot (2 \cdot \pi \cdot f)^2 \cdot \frac{\cosh(k_{wave}(z+d))}{\sinh(k_{wave} \cdot d)} \cdot \sin(k_{wave} \cdot x - 2 \cdot \pi \cdot f \cdot t) \tag{2.9}$$

Here x is the distance along the MSL [m], z is the distance from the MSL [m], t is time [s], ζ is the wave amplitude [m] (obtained from the PM approximation), k_{wave} is the wave number $(2\pi/\lambda_{wave})$ $[m^{-1}]$, f is the wave frequency [Hz], λ_{wave} is the wave length [m] (also obtained from PM) and d is the water depth [m]. Figure 2. 8 shows the application of these values graphically.

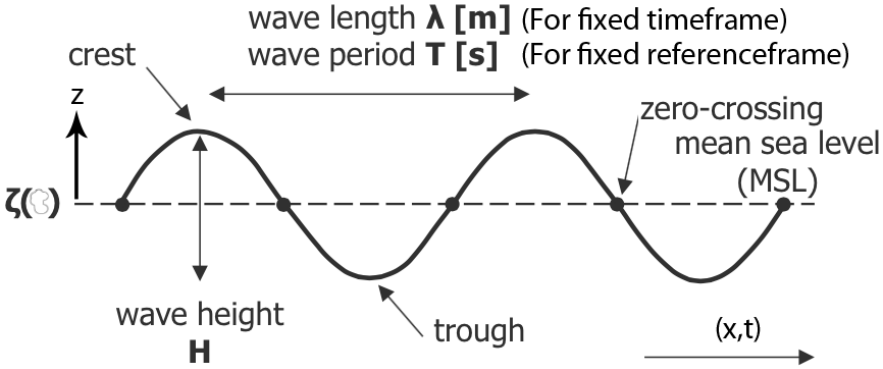

Figure 2. 8 - Wave characteristics

After the individual sinusoids are created for each frequency along the PM spectrum, a random generated phase angle is inserted in each of the sinusoids to convert the orderly wave structure back in the chaotic one observed in practice. All wave particle movements are summed to yield the approximated wave field as a function of time and space. The complete process is graphically represented in Figure 2. 9. Wave particle movement is now successfully converted to mathematical terms such that it can be used to evaluate structure loads.

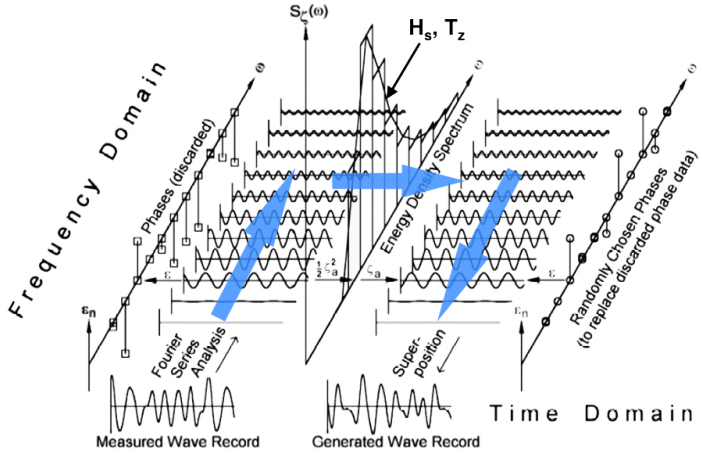

Figure 2. 9 - Analytical representation of waves

However, linear theory of the PM spectrum, is only valid in 'deep water'. A parch of water is considered 'deep' when its depth (d) is larger than half the wavelength (λ_{wave}). At locations with lesser water depth, for example near shore or at sandbanks, the subsurface influences wave movement results in the formation of breaking waves (Figure 2. 10). To address loads from these waves different theory is required.

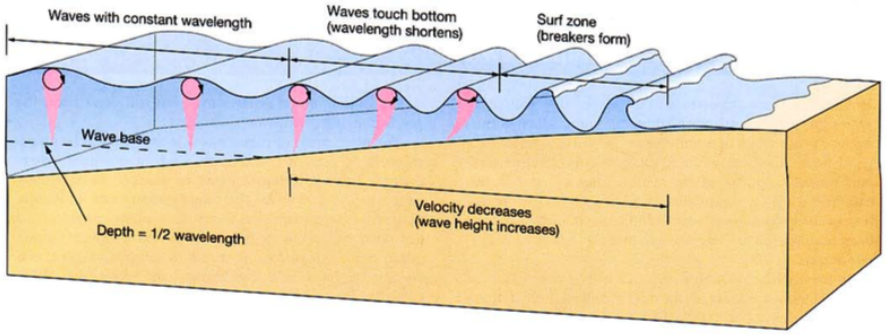

Figure 2. 10 - Subsurface influenced waves

Non-linear wave theory is applied for near shore regions. Due to the diversity of possible wave scenarios, there is however not a single governing non-linear wave theory that describes particle motion. Figure 2. 11 depicts the applicable regions for different wave theories as a function of wave height (H), wave period (T) and water depth (d). Since this theory is too complex for the preliminary design phase, its not discussed further.

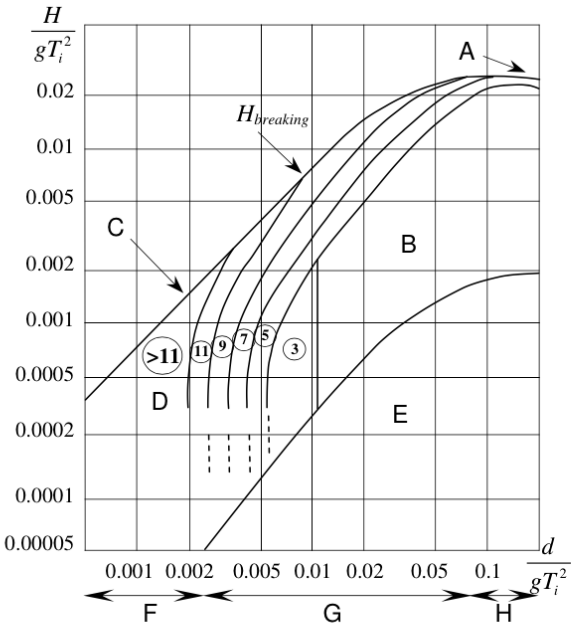

A Deep water breaking limit $H / \lambda_{wave} = 0.14$
B Stokes' 5th order, New Wave or 3rd order Stream Function
C Shallow water breaking limit $H / d = 0{,}78$
D Stream function (showing order number)
E Linear / Airy or 3rd order Stream Function
F Shallow water
G Intermediate depth
H Deep water

Figure 2. 11 - Wave theories

Sea level elevations

The largest drivers of sea level elevations are tides and storm surges. Firstly, tides are caused as a result of the magnetic origin of the water molecule due to its dipole moment. The magnetic force of the water particle is affected by the gravitational pull of the sun and moon. This results in the water 'following' the path of these astral objects. Additionally, there is a monthly cycle that changes the intensity of this tidal affect as a result of the sun and moon being aligned. Within this cycle, the maxima are referred to as 'spring tide' and are indicated as LAT for the lowest astronomical tide, and the HAT for the highest astronomical tide. Obstruction of tidal movement due to landmasses and bathymetry (underwater topography) also create certain tidal patterns, this pattern is known as the amphidromic system. Due to its particular bathymetry a very interesting amphidromic system has formed in the North Sea, as depicted in Figure 2. 12. In this image, red dots indicate locations without tidal effects (Coriolis effect). Furthermore, blue and red lines indicate respective the highest tide for the respective location locations that experience these at the similar times. Since tides are unaffected by weather conditions, information is easily extrapolated from metocean data. Typical values for North Sea tidal ranges are from 2 m, near the Dutch coast, to nearly 12 m in the English Channel.

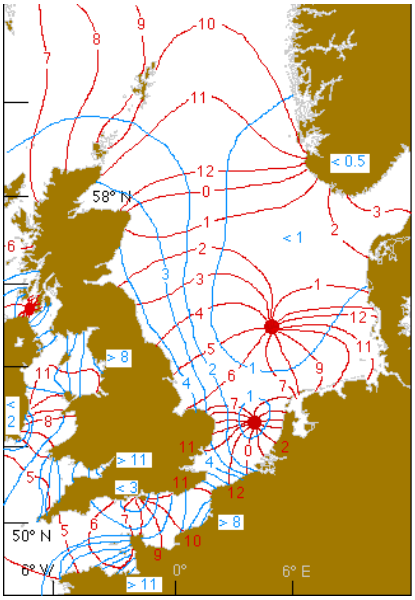

Figure 2. 12 - Amphydromic system North Sea

Second, storm surges are caused by water being pushed in a certain wind direction. These are however not extracted with such ease as tides are. Its spectra are found by monitoring water ranges obtained from measuring buoys and comparing this data to weather effects (storms) to chart water level differences that are not explained by tidal differences and waves.

Currents

Currents are mainly caused by tides and ocean circulation but are, in a lesser extent, also affected by storm surges and temperature and salinity differences. Since currents are largely affected by tides and ocean circulation the largest currents emerge where tides and ocean circulation is the strongest. Currents are often approximated using power law profiles, much like is done for wind shear profiles. However, as a result of the increased kinetic energy exchange in fluids compared to air, modeling of currents is challenging. Solely using power law profiles to address current speeds could prove to yield inaccurate results. However, for the preliminary design phase, current profiles still give a good insight. Three sorts of approximation are often used to model currents; a linear profile, bilinear profile or a power law profile as displayed in equation (2.10).

$$U_{current}(z)[m/s] = U_{Current0} \cdot \left(\frac{z+d}{d}\right)^{\alpha_{current}} \tag{2.10}$$

Figure 2. 13 depicts the three different current profiles. Here U_{c0} is the surface current [m/s], d is the water depth and $\alpha_{current}$ is the current exponent, which is usually taken as 1/7 according to Tempel (Tempel 2006).

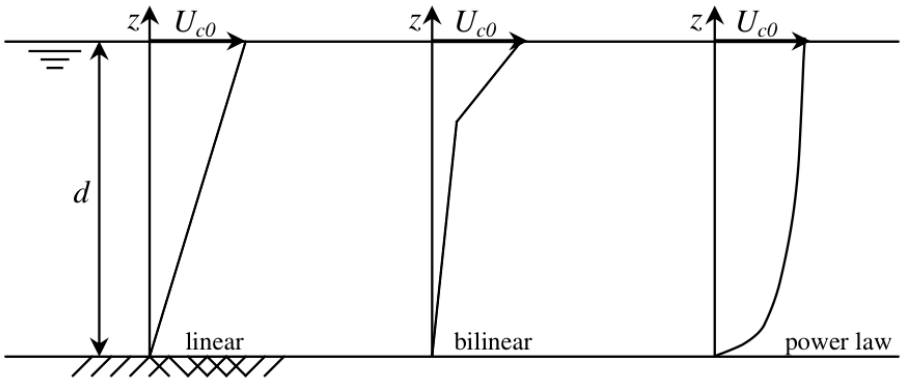

Figure 2. 13 - Different current profiles

Soil

Moving downward along the structure the mudline is reached. In contrast to the rapid change of propperties of water and air, changes in the soil occur over millions of years. In the North Sea, the top 500 m of soil is referred to as the Upper North Sea Group. This group mainly consists of sand and clay but also contains traces of gravel. In an effort to estimate foundation reactions of the substructure in the soil, its properties are measured in a laboratory or with the help of a cone penetration test (CPT). In a CPT a probe is lowered in a borehole that measures the resistance of the surrounding soil as it is slowly lowered in the ground. Apart from soil density, a different set of properties is extracted from sand and clay samples. Important parameters from clay include, undrained shear strength (s_u) [N/m²] and the required strain for 50% of peak stress (ε_{50}) [%]. For sand, the internal angle of friction (Φ) [°], relative density (D_r) [%] (which indicates how close the sand is packed) and N_q the dimensionless bearing capacity factor, are looked for.

These parameters are only obtained by physically extracting soil from the desired location. This is costly and time consuming thus it is evident that the data is not available during early stages of the design. Soil characteristics can also acquired using seismic surveys, a technique used to find out density and soil type with the help of sound waves (Oceania 2012).

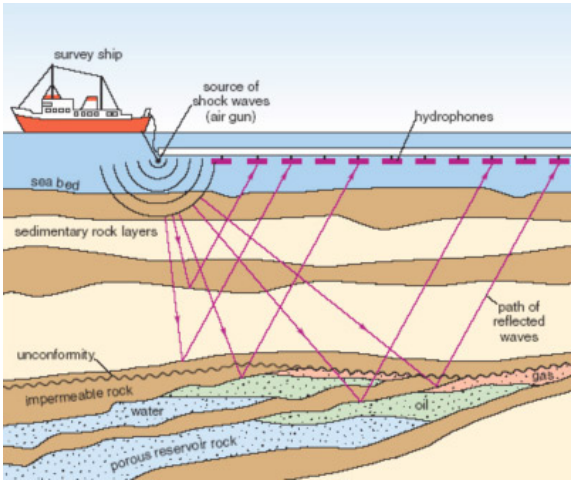

Figure 1 - Seismic survey

Examples of soil properties are combined in Table 2. 1 (Geotechdata 2014).

Clay	S_u [kPa]	ε_{50} [%]	Sand	D_r [%]	Θ [°]	N_q [-]
Soft	0-25	1,5	**V. loose**	< 20	< 30	8
Firm	25-50	1,5	**Loose**	20-40	30-35	12
Stiff	50-100	1	**Compact**	40-60	35-40	20
V. stiff	100-200	0,5	**Dense**	60-80	40-45	40
Hard	>200	0,5	**V. dense**	> 80	> 45	50

Table 2. 1 - Soil properties

2.3.2 Turbine data

Once the environmental data is acquired it serves as input to select a proper turbine. For turbine selection, the most important asset is obviously generating the largest amount of energy. This however does not necessarily mean that bigger is better. Larger turbines have higher internal resistances and often a bigger rotor diameter as well. The first step is selecting possible turbines based on secondary parameters. Here price, availability (η) (which is a function of reliability, maintainability and serviceability) and turbine's power curve (P) are of importance. Second, for each turbine, a Weibull diagram is created for each wind direction from acquired environmental data. Then, the annual output of a turbine (E_y) is calculated by multiplying the power curves of each turbine with the Weibull diagram for each wind direction, as displayed in Figure 2. 14.

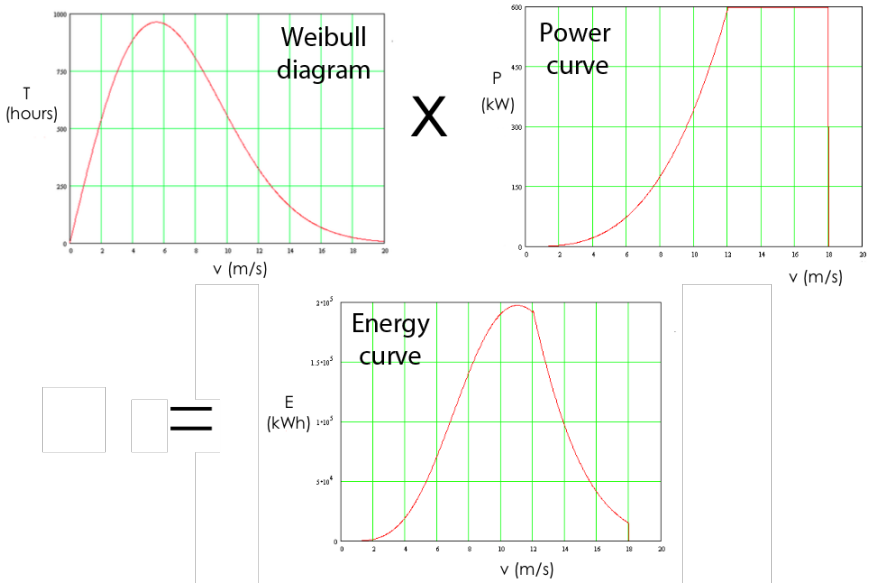

Figure 2. 14 - The energy curve

By summing up these curves for each wind directions and combining these with estimated availability, the annual energy production is found (e.q.: (2.11)).

$$E_y[KWh] = 8760 \cdot \eta \cdot \sum_{directions} \int_0^{V_{max}} T(v) \cdot P(v) dv \tag{2.11}$$

Finally, these values are converted to monetary terms by dividing them over the expected annual cost of the turbine. This results in the so-called levelized production cost, or LPC. The results do not only include investment cost of the turbine but are rather a function of investment costs (C_{Invest}), operation and maintenance costs ($C_{O\&M}$) and decommissioning costs (C_{Decom}) combined with financial effects such as discounting and interest (r) over the lifetime (L) of the project, which are incorporated in the annuity factor (a) (e.q.:(2.12)).

$$LPC[\frac{€}{KWh}] = \frac{C_{Invest}}{a \cdot L \cdot E_y} + \frac{C_{O\&M}}{L \cdot E_y} + \frac{C_{Decom} \cdot (1+r)^{-L}}{a \cdot L \cdot E_y} \tag{2.12}$$

Obviously, the turbine with the lowest LPC is selected for the site.

2.4 Design elevations

Now environmental conditions and the used turbine are known, the actual support structure design is given a closer look. Firstly, the height of the platform, which is located at the interface level, is calculated using equation (2.13). Again, the mean sea level (MSL) is taken as a reference point. The height of the platform is found using 50-year extreme values of lowest astronomical tide (LAT), tidal range (tide), surge and wave crest as obtained from the environmental data. Additionally, an air gap (Z_{air}) of 1,5 m is incorporated to prevent waves from ever reaching the platform.

$$Z_{\text{interface}}[m] = LAT + \Delta Z_{Tide} + \Delta Z_{Surge} + 0{,}65 \cdot \Delta Z_{Wave} + \Delta Z_{air} \tag{2.13}$$

Figure 2. 15 gives, a representation of the discussed platform height for a monopile. Obviously, for a jacket design the same elevation heights are used.

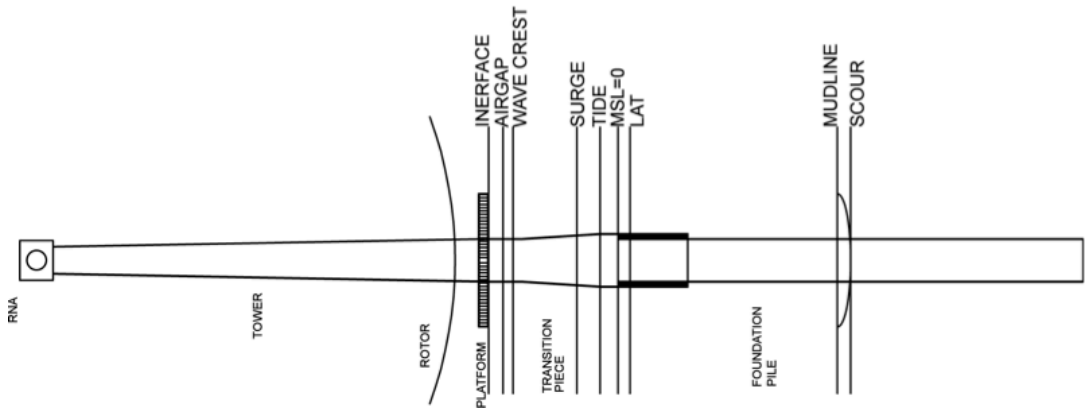

Figure 2. 15 - Elevation levels

Now the platform height is established the height of the rotor nacelle assembly (RNA), is found using equation (2.14). Here D_{rotor} and $Z_{clearacnce}$ represent the rotor diameter and an extra air gap respectively. $Z_{clearacnce}$ is usually chosen between 5 and 8 meter so that the rotor can never hit the platform

$$Z_{hub}[m] = Z_{Interface} + \Delta Z_{Clearance} + 0{,}5 \cdot D_{Rotor} \tag{2.14}$$

2.5 Allowed natural frequency

Massive fatigue damage or even abrupt collapse of the structure can occur when wave excitation or turbine rotational frequency approaches the turbine's natural frequency boundaries. For three bladed turbines, 1P and 3P rotational frequencies are particularly destructive. The structure is designed in such a way that these boundaries are never crosses. A design can either be of a soft-soft, soft-stiff or stiff-stiff type depending on the natural frequency range (Figure 2. 16).

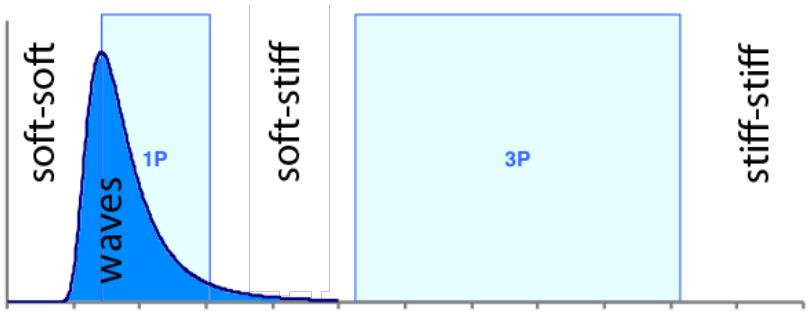

Figure 2. 16 - Natural frequency boundaries

Soft-soft and stiff-stiff structures are generally avoided in offshore engineering. A soft-soft design could still experience problems due to wave excitation while a stiff-stiff design has a high weight. Such a design is costly and can potentially lead to increased fatigue damage.

2.6 Preliminary geometry

Once design basics are found actual dimensioning of the support structure is commenced. Firstly, the tower's preliminary geometry is estimated from previous tower designs, obtained from former projects or reference turbines. Once the tower is defined, this process is repeated for the support structure using several rules of thumb. When both designs are established they are combined and subjected to the natural frequency and extreme load checks of the coming design process steps.

2.6.1 Tower

Tower geometry is defined before a closer look is attained at the subsurface support structure. Firstly, its wall thickness and top and bottom diameter estimated. Here the geometry is found either by simply obtaining the dimensions from the turbine manufacturer or by fitting earlier designs to known design elevations. A good source of information is, for example, the 5MW offshore NREL reference turbine (NREL 2009). Since the tower is only connected to the top of the support structure, its design is largely independent of the support structure design.

Deriving the preliminary dimensions for the monopile and jacket structure is wildly different in contrast to the tower. Their methodology is discussed in the following sections.

2.6.2 Monopile

The monopile exists of two parts, namely the foundation pile and transition piece. The foundation pile transfers loads to the soil. A transition piece is used to protect delicate pars that could be damaged during pile of the foundation pile. For the monopile design process firstly, general dimensions are estimated. Diameter, wall thickness and embedded pile length are main drivers for design. The dimensions must be sufficient to pass axial, lateral and foundation displacement tests but also be kept at a minimum to prevent possible natural frequency problems while keeping material costs at a minimum.

As a rule of thumb, the foundation pile diameter is estimated to be equal to the bottom diameter of the tower. Its wall thickness is determined by maintaining a diameter over wall thickness ratio of roughly 80 to 90 (Lourens 2014). Additionally, the foundation pile length is set to be equal to the distance from the MSL to the mudline plus a soil penetration depth of 10 times the pile diameter (Oord 2014).

Once the preliminary dimensions of both the tower and foundation pile are known, transition piece geometry is addressed. The transition piece is often connected to the foundation pile using grout. This is essentially a connection formed by sliding the transition piece over the foundation pile and creating a stiff connection by filling the gap with grout, a sort of cement. The main driver for the height of the transition piece is the length of the grouted connection, which itself is usually around 1,5 times the foundation pile diameter (Lourens 2014). Additionally, the distance from the top of the grouted connection to the tower bottom is also added to transition piece length. The inner diameter of the bottom of the transition piece obviously is equal to the foundation pile diameter plus total grout thickness. Its top diameter has to be equal to the bottom diameter of the tower to limit stress concentrations.

2.6.3 Jacket

Before the preliminary dimensions of the jacket structure are discussed, a closer look in the structure is needed to become more familiar with its components. Figure 2. 17 shows the basic design of the most common used type of jacket structure, the X-braced jacket. Other popular concepts include Z-braced and K-braced concepts. The main advantage of an X-braced jacket structure compared to the K-brace and Z-brace type is its increased redundancy and torsional resistance. The downside of X-bracing is however an larger number of required members in the design, which increases production and material cost (El-Reedy 2012). Since X-braced configurations are most common in offshore wind, only this concept is discussed within this thesis. Furthermore, for its design only a four-legged structure is discussed, which is currently the most common configuration.

Preliminary dimensions of the jacket structure are mostly based on experience. Dimensions are fitted to certain rules of thumb. These rules of thumb however don't result in immediate design parameters but are rather fitted to industry-standardized pipe sizes. When designing offshore wind support structures, using horizontal members in the splash zone (the vertical range where waves can hit the structure) is avoided to prevent load peaks that result from wave slamming. Commonly a mud brace, a horizontal brace located at the mudline, is applied to prevent structure deformation during transportation and installation. Additionally, legs are placed at an angle (batter) to provide a larger base at the mudline, which is beneficial for load distribution and provides increased resistance against overturning moments.

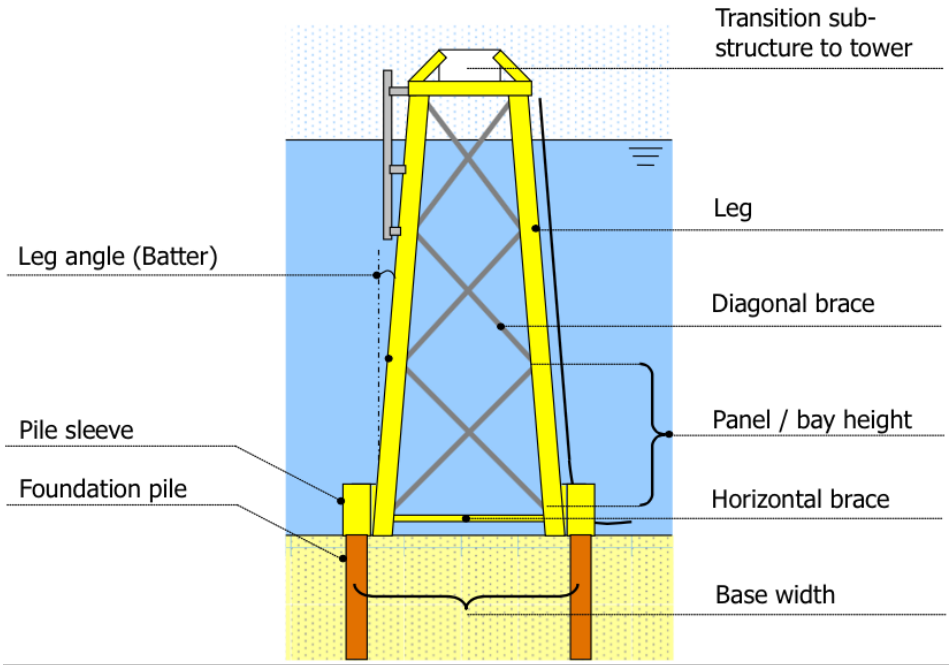

Figure 2. 17 - Jacket structure

The width of the platform located at the interface level is set equal to the tower diameter plus an extra 3,5 to 4,5 meter on either side of the base (El-Reedy 2012). This provides sufficient room for the maintenance crew to maneuver. From here the base with of the structure is determined using a leg batter slope of 1:7 to 1:8 (El-Reedy 2012). Additionally, a leg diameter between 1 and 1,5 meter is picked as a fair preliminary size (ABS 2011). Brace diameters are kept within a slenderness ratio (KL/r) of between 70 and 90, according to industry-accepted practice (ABS 2011). Here however, sticking to the higher end of the range is recommended since this results in large wall thicknesses, which is beneficial against buckling. For wall thicknesses of both braces and legs a diameter over wall thickness (D/t) ratio between 19 and 60 us used (ABS 2011). Larger ratios will most-likely result in local buckling problems while tubes with ratios lower than 19 are difficult to obtain. Finally bay height is estimated from leg angles of 40 to 50 degrees for efficient loading distribution (Lourens 2014).

The bottom of the support structure is connected to four foundation piles. These foundation piles can either be pre- or post-piled. The penetration depth of the pile found using a pile length over diameter ratio of 10, as is also the case in monopile design. This results in a lower penetration because jacket foundation piles usually have a diameter of only 2 to 2,5 meter (ABS 2011). This is sufficient since the geometry of the jacket provides a much larger resistance against overturning, as would've been the case in a monopile. Additionally, since jackets are equipped with multiple foundation piles, lateral pile resistance is not as much of a problem compared to monopiles.

2.6.4 Structure natural frequency

As discussed early in this chapter, natural frequency problems could result in abrupt structure failure. Therefore whenever changes are made to the design, natural frequency is checked again. Two types of natural frequency analyses are possible, static or dynamic. Here the difference origins in the nature of external forces, analyses where external forces are time dependent are coupled within the analysis and are considered dynamic. Static analyses either have external forces that are independent of time or might even be entirely neglected.

Commonly, for the preliminary design phase static analysis are performed. Once environmental data is acquired, finite element method (FEM) software yields a more precise natural frequency for a dynamic analysis in the detailed design phase. Since the scope of this thesis focuses on the preliminary design phase only static methods are addressed. In general either the Rayleigh or direct method is used to obtain structure natural frequency. These methods are based on the energy principle and equation of motion respectively. In both cases the natural frequency is estimated using linear single degree-of-freedom (1 DOF) structural models or by coupling multiple single DOF's to form a multiple DOF system to yield a more accurate result. The model of a single DOF is displayed in Figure 2. 18, here the structure is described as a mass connected to a infinitely stiff surface using a spring (k) and viscous damper (c). Excitation by an external force (F) will result in a certain response of structure (x).

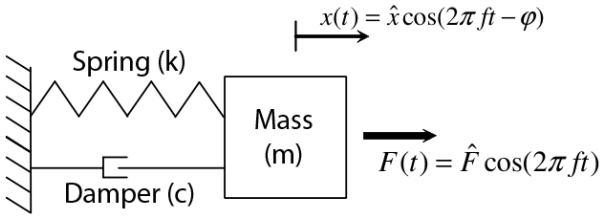

Figure 2. 18 - Single DOF spring-damper system

Using general equation (2.15) leads to the natural frequency of the structure, this would be in the form of equation (2.16) for a 1 DOF system. Here k^* and m^* represent the generalized stiffness and mass respectively.

$$[M]\cdot\{\ddot{x}\}+[C]\cdot\{\dot{x}\}+[K]\cdot\{x\}=[F(x)] \tag{2.15}$$

$$\omega_n[rad/\mathrm{s}]=\sqrt{\frac{k^*}{m^*}} \tag{2.16}$$

Finally, frequencies are compared to the 1P and 3P rotor rotational frequencies which where determined earlier. If the values coincide, structure dimensions are updated.

2.7 Extreme loads

2.7.1 Load cases

Once all physical attributes are acquired these help estimate the extreme loads on the structure. Firstly however, several ultimate load cases (ULC) are constructed from selected design load cases (DLCs) as described in design standards (e.g. (DNV 2013), (GL 2012), (IEC 2009)). For the detailed design phase, the structure is tested against all the prescribed DLCs from the standards ranging from normal power production (DLC1.x in (DNV 2013)) to transport, assembly and repair (DLC6.x in (DNV 2013)). Assessing the structure for all extreme environmental conditions (wind/wave) occurring at the same time is not desired since a situation like this is very unlikely to occur during the lifetime of the structure and result in a conservative design.

2.7.2 Safety factors

Generally, a loading (safety) factor (Υ_{le}) of 1,35 is applied for environment-induced loading. For static loading, which for example is caused by structure weight, a safety factor (Υ_{ls}) of 1,25 is applied. These safety factors are adopted according to those prescribed by DLCs in standards

2.7.3 Turbine

Blade-element and momentum theory (BEM) is often used for estimation of the thrust force on the RNA. Equation (2.17) gives the expression for this trust force. Here A_D is the area of the imaginary actuator disk with equal radius as blade length in m², U_∞ is the unobstructed airflow before the turbine at the height of the nacelle in m/s and C_T is the dimensionless thrust coefficient that describes the portion of kinetic energy exchange to the blades by the air particles. This factor is greatly affected by blade geometry and pitching angle of the blade, it's maximum when the turbine is operating at rated wind speed and assumed zero at cut-out wind speed, when blades are fully pitched.

$$F_{thrust}[N] = \frac{1}{2} \cdot \rho_{air} \cdot A_D \cdot U_\infty^2 \cdot C_T \tag{2.17}$$

However, for a complete analysis, loads induced by the turbine also need to be known for when it's not operational. For DLCs concerning these scenarios, drag theory is used to get a sense of RNA loads. Blade drag is estimated for multiple blade configurations with respect to the airflow to simulate possible scenarios ranging from the turbine being parked (blades fully pitched) to system failures where blades are not pitched and therefore experience a maximum drag load.

2.7.4 Tower

Loads on the tower are a combination of forces on the nacelle plus the drag force exerted by air passing along it. For the preliminary design phase, drag force is often modeled for an exponential wind shear profile that passes a conic tower. Equation (2.18) gives tower drag as a function of its height (z). For the detailed analysis this model is expanded such that a better description from turbulence and tower shadow is considered.

$$F_{drag}[N] = \int_{x_0}^{x_1} \frac{1}{2} \cdot C_d(x) \cdot \rho_{air} \cdot A(x) \cdot (U_{10} \cdot \frac{\ln(x / z_0)}{\ln(10 / z_0)})^2 dx \tag{2.18}$$

2.7.5 Substructure

Methods to establish structure dimensions for monopile and jacket greatly diverge at this point. Therefore both structures are discussed separately. Firstly, the design procedure of a monopile is discussed. Second, the general design procedure for a jacket is treated.

Monopile

The monopile is exposed to horizontal loads from the environment plus vertical loads from its own weight plus, obviously, all loads acting on the RNA and tower. Since the transition piece crosses the waterline, the largest portion of hydrodynamic loading induced by currents and (breaking) waves is experienced by it. For the preliminary design phase waves are often either be described using Airy/Stoke linear theory for deep water (Figure 2. 11). Once the wave particle velocity field is known, appropriate drag and mass coefficients (C_D and C_M) are estimated using the Reynolds number. Note that these coefficients are not only estimated from the foundation pile itself, but also by marine growth and secondary steel such as the boat landing. Combining the acquired coefficient with the velocity field of waves and structure geometry result in the input for Morrison theory, where f_d and f_m represents Morison drag and mass terms respectively (e.q.:(2.19) to (2.21)).

$$f_{Morison}(x,z,t)[N] = f_d(x,z,t) + f_m(x,z,t) \tag{2.19}$$

$$f_d(x,z,t)[N] = \frac{1}{2} \cdot C_d(x) \cdot \rho_{water} \cdot D(x) \cdot |u(x,z,t)| \cdot u(x,z,t) \tag{2.20}$$

$$f_m(x,z,t)[N] = C_m(x) \cdot \frac{\rho_{water} \cdot \pi \cdot (D(x))^2}{4} \cdot \dot{u}(x,z,t) \tag{2.21}$$

For each selected DLC the wave type with highest spectral energy density as obtained from the wave spectra is used to establish these loads. Loads are evaluated for the highest water level that occurs within the boundaries of the respective DLC plus scour depth. Structure weight and buoyance forces are also addressed. In the detailed design phase, this methodology is repeated but now for combination of multiple combined velocity fields obtained from the PM spectrum and for different wave heights.

Then, currents are modeled using a current profile as discussed earlier. Its induced loading on the structure is estimated using drag theory.

As a final step, acquired external monopile forces are summed over the height of the structure. This results in a complete mapping of force and moment distribution along the structure's height. Results serve as input when foundation reactions and internal stresses are addressed in the forthcoming design steps.

Jacket

Since both monopile and jacket structure have the same super structure, these are exposed to equal top loads. Furthermore, the jacket structure is subjected to the same velocity field of waves and currents. However, to find out hydrodynamic loads on the jacket, a different approach is needed. In an attempt to convert de complex geometry of the jacket to a form that can be easily handled, an equivalent monopile is determined for each bay using Figure 2. 19. For this method, several members are thus converted to one single larger member that is subjected to an equal hydrodynamic loads.

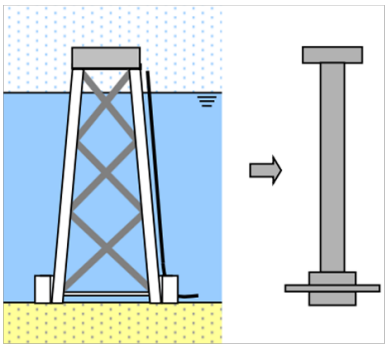

Orientation	Parallel to wave direction		Perpendicular to wave direction	
	drag	***inertia***	***drag***	***inertia***
Vertical	$D_{eq} = D$	$D_{eq} = D$	$D_{eq} = D$	$D_{eq} = D$
Horizontal	0	0	$D_{eq} = L$	$D_{eq} = \sqrt{DL}$
Diagonal	$D_{eq} = D$	$D_{eq} = D$	$D_{eq} = D/\sin\theta$	$D_{eq} = D/\sqrt{\sin\theta}$

Figure 2. 19 - Equivalent diameter

Formulae needed to establish the size of these equivalent diameters are given in equations (2.22) and (2.23). When these diameters are evaluated, the effect on diameter size due to marine growth and secondary steel items should not be neglected.

$$D_{Drag,equivalent}[m] = \sum_{i=1}^{n} D_{member,i} \tag{2.22}$$

$$D^2_{Mass,equivalent}[m] = \sum_{i=1}^{n} D^2_{member,i} \tag{2.23}$$

This method however does not take into account that members that are placed behind each other along the flow direction and therefore experience different flow patterns as a result of the disturbed flow. Although this method is flawed it's still widely accepted in offshore engineering and is used in both the preliminary as the detailed design phase.

The equivalent diameter is dependent of water particle inflow angle. Therefore different inflow angles are considered each DLC (Figure 2. 20).

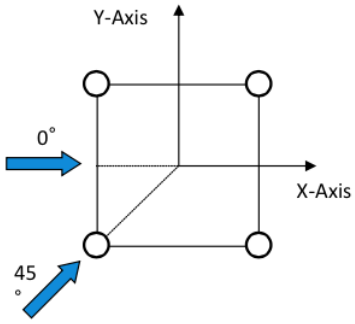

Figure 2. 20 - Different inflow angles

Finally, internal forces from structure weight and buoyant members are incorporated in the design for both the preliminary as detailed phase.

2.8 Foundation stability

When addressing foundation stability, the fist meters of pile should always be neglected from the analysis to take into account the effects of scour, even when scour protection is applied.

Monopile and jacket foundation stability analyses have different approaches. However, criteria for both cases are similar. These include; axial pile stability, lateral pile stability and natural frequency check. Additionally, due to the larger base of the jacket structure, the over tipping moment and forces are calculated to estimate the load distribution over the foundation piles. Commonly, a combination of the methods as described by the American Petroleum Institute (API), Det Norske Veritas (DNV) and Germanischer Lloyd (GL) are used for foundation pile design. For this chapter the method comprised of API, DNV and GL as proposed by van Oord (Oord 2014) is discussed.

Firstly, axial pile stability for a monopile or a jacket is checked using the same method (API 2000), results often don't call for design alterations since axial displacement is most often not design driving. Second, lateral stability is checked. This can, among others, be done using the American Petroleum Institute (API) guidelines (API 2000), which uses the 'P-Y method' to find out soil behavior, or by using Germanischer Lloyd (GL) rules and regulations (GL 2012), which addresses the 'vertical tangent criterion'. Both methods are discussed in this paragraph; GL is used for the monopile and API for a jacket. Finally, once axial and lateral stability are addressed, the effect of changes in natural frequency of the structure are checked which resulted from alteration of its geometry.

2.8.1 Axial stability

For axial pile stability the method can be used for the monopile and jacket structure. The foundation pile's axial stability check is successful if axial forces caused by structure weight and external loading are smaller as the axial bearing capacity of the soil in contact with the foundation pile. Equation (2.24) is used for estimation of the soil's axial bearing capacity. Here Q_S represents shaft skin friction, acting either only on the pile's outside area for a plugged pile or both the outside and inside areas for unplugged piles and is found using the unit skin friction capacity (f) and side surface area of the pile (A_s). Q_P, which is a function of the unit end bearing capacity (q) and the gross end area of the pile (A_p), addresses either the pile's end area bearing capacity if it's plugged or area of annulus for unplugged piles. A plugged pile is one where the soil inside the pile does not contribute to axial stability but rather moves freely with the pile. This occurs when inner friction of the pile is larger as its end bearing. Thus in order to establish if the pile is either plugged or unplugged, the outcome of both analyses are compared.

$$Q[N] = Q_S + Q_P = f \cdot A_s + q \cdot A_p \tag{2.24}$$

Different approaches are required when shaft skin friction (Q_S) and end bearing (Q_P) are addressed for sand and clay. These are discussed on the next page.

For clay, shaft skin friction capacity is found using equation (2.25). Here the dimensionless α is a function of undrained shear strength and the effective overburden pressure p'_0. This is the increased pressure at the investigated location due to overlying soil and fluid pressure.

$$f_{clay}[N/m^2] = \alpha \cdot S_u \tag{2.25}$$

$$\alpha = \begin{cases} 0{,}5 \cdot \psi^{-0{,}5} & \text{for } \psi \leq 1{,}0 \\ 0{,}5 \cdot \psi^{-0{,}25} & \text{for } \psi \leq 1{,}0 \end{cases} \tag{2.26}$$

$$\Psi = \frac{S_u}{p'_0} \tag{2.27}$$

$$p'_0[N/m^2] = p_0 + g \cdot \int \rho_{soil}(x)dx \tag{2.28}$$

Establishing end bearing capacity is straightforward:

$$q_{clay}[N/m^2] = 9 \cdot S_u \tag{2.29}$$

For sand, shaft friction is found using equation (2.30). Here K is the coefficient of lateral earth pressure that is usually taken as 0,8 in driven piles that are subjected to tension and compression (API 2000). Additionally, θ is the internal friction angle between the soil and pile wall.

$$f_{sand}[N/m^2] = K \cdot p'_0 \cdot \tan(\theta - 5) \tag{2.30}$$

The end bearing capacity for sand is a function of the effective overburden pressure and a dimensionless bearing capacity factor N_q.

$$q_{sand}[N/m^2] = p'_0 \cdot N_q \tag{2.31}$$

In the detailed assessment axial pile stability is investigated further by modelling the soil layers as coupled non-linear spring systems in the form of axial load pile displacement, or t-z, curves. Here interactions between soil layers are observed, which yields a more detailed result as the linear method discussed in the preliminary phase. Coupled t-z curves furthermore help provide useful information about the bending shape of the foundation pile, which is used to determine the minimal required foundation pile length, which is needed for cost reduction purposes.

2.8.2 Lateral stability

For lateral foundation stability, soil resistance and bending shape of the foundation pile are of importance. Both analyses require the use of P-Y curves. These curves represent the displacement and reactions of the soil in the form of a non-linear spring. Figure 2. 21 depicts a typical (coupled) soil spring system; here the red dots indicate the displacement Y of the curve under loading P of a certain DLC. Additionally, the top P-Y curve shows displacement in the non-linear area. Here thus plastic deformation of the soil occurs, which is undesired. Plastic deformation will however always occur just below the mudline, this effect is referred to as wedging.

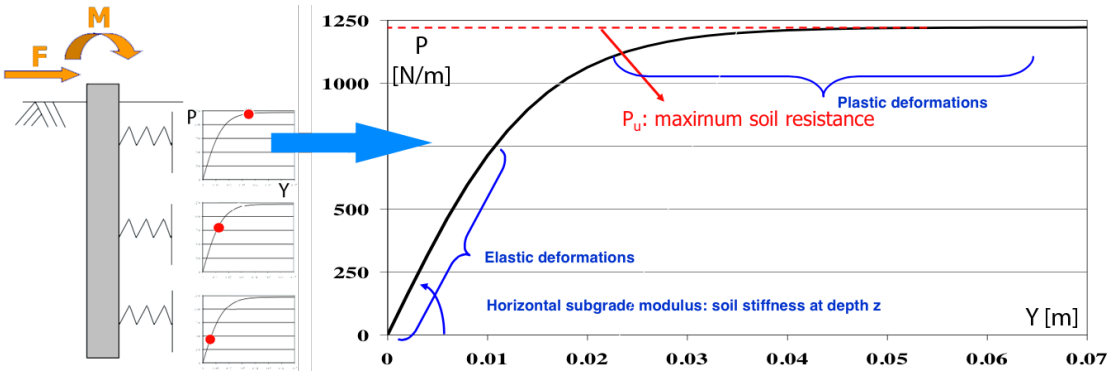

Figure 2. 21 - Soil-spring system

When borehole P-Y curves from the CPT are not available, the P-Y is approximated from general soil properties. For clay, P-Y curves are drawn based on the maximum soil resistance P_u and Y_c (Y_c is the location where half P_u occurs). The formula for maximum soil resistance is shown in equation (2.32). Here γ is the effective soil weight [kN/m^3], X is the depth below the mudline [m], J is a dimensionless empirical constant between 0,25 and 0,5 and D is the diameter of the foundation pile in question. Furthermore Y_c is calculated in equation (2.33). The shape of the curve is fitted to the prescribed shape of a clay P-Y curve.

$$P_u[N/m] = 3 \cdot S_u + \gamma \cdot X + J \cdot \frac{S_u \cdot X}{D} \tag{2.32}$$

$$Y_c[m] = 2{,}5 \cdot \varepsilon_{50} \cdot D \tag{2.33}$$

P/P$_u$	Y/Y$_c$
0,00	0,00
0,50	1,00
0,72	3,00
1,00	8,00
1,00	∞

Table 2. 2 - P-Y curve for clay

For sand a different approach is required. The ultimate lateral bearing capacity of sand depends on the depth where it is located. Therefore, firstly the ultimate bearing capacity of both shallow and deep sand are evaluated in equations (2.34) and (2.35) respectively using Figure 2. 22 (left). Here H is the depth of the respective layer. Whichever value is lowest is used as the ultimate bearing pressure for sand.

$$P_{u,shallow}[N/m] = (C_1 \cdot H + C_2 \cdot D) \cdot \gamma \cdot H \tag{2.34}$$

$$P_{u,deep}[N/m] = C_3 \cdot D \cdot \gamma \cdot H \tag{2.35}$$

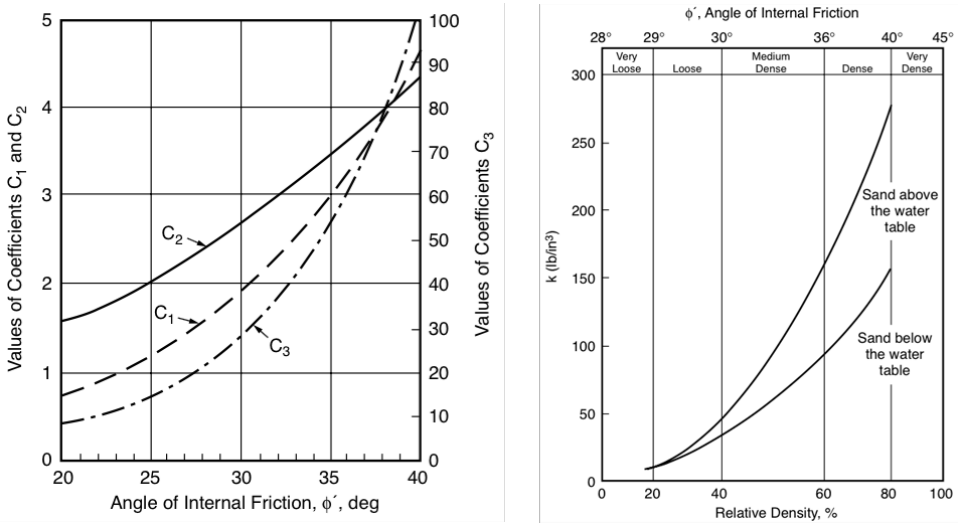

Figure 2. 22 - Coefficients ad function of friction angle (left)

and spring coefficient as function of relative density of friction angle (right)

Once the ultimate bearing pressure is known the P-Y curve is plotted using equation (2.36) where k is the initial modulus of subgrade reaction obtained from Figure 2. 22 (right).

$$P(y)[N/m] = 0{,}9 \cdot P_u \cdot \tanh\left(\frac{k \cdot H}{0{,}9 \cdot P_u} \cdot y\right) \tag{2.36}$$

Once P-Y curves for the soil layers are acquired they are used to estimate the foundation stability of the pile. Here both the soil resistance as the bending behavior of the foundation pile are of importance. Lateral stability can be estimated in the preliminary design phase using equal method as axial stability, the average pile displacement for a certain length and diameter of a foundation pile is found by summing up P-Y curves for every soil layers. This effectively maps the different soil springs from the soil layer on one single soil spring. Hooke's law is used to find the average displacement of the pile for a certain load extracted from a DLC.

This does however not predict if plastic deformation occurs in the soil, answering this question requires insight in the bending behavior of the foundation pile, which is achieved from P-Y curves. This can either be modeled in the detailed or preliminary design phase in a simplified manner. Simplifying the model for the preliminary design phase is achieved by merging several adjacent soil springs that have similar P-Y curves.

Once the foundation pile is modeled and subjected to a selected DLC, deflection curve on the left side of Figure 2. 23 is found when connecting the red dots in Figure 2. 21.

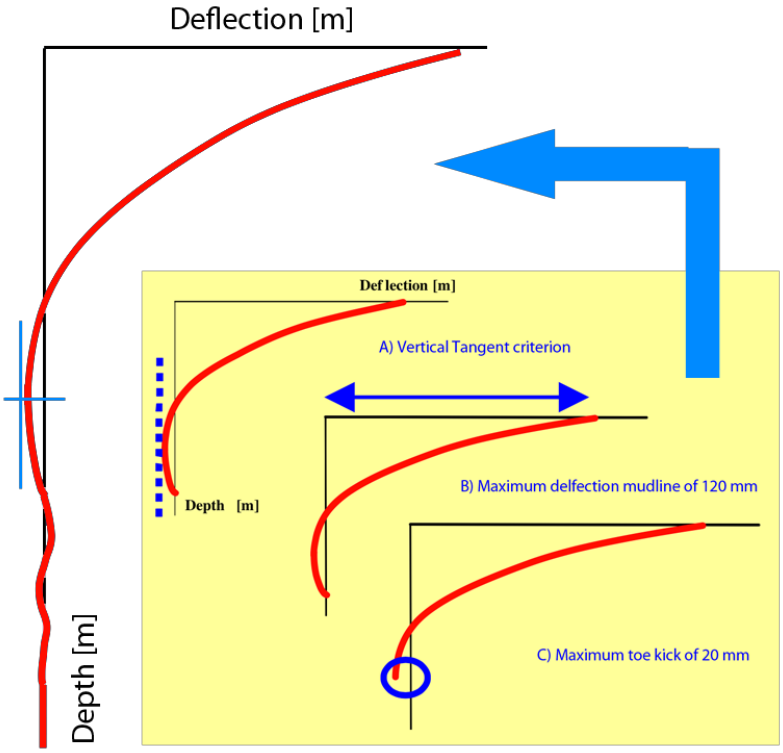

Figure 2. 23 - Foundation pile subjected to modelling criteria

Now the foundation pile is shortened using the three criterion of Figure 2. 23. Firstly the foundation pile is cut off below the highest location where a vertical line can be drawn tangential to the displacement curve (A). Since this is a drastic geometry change a new displacement curve is calculated for the adjusted length since. Second, the vertical tangent criterion is checked in addition to a maximum mudline deflection check and tie kick check of 120 and 20 mm respectively.

If all three tests pass, the natural frequency of the structure is checked once again, if these fall within the 1P and 3P zone the diameter of the foundation pile is changed to increase structure stiffness.

2.9 Structure stresses

This fore last design step evaluates three failure types; Yield, stability and punching. Firstly, internal stresses in the structure are discussed for both the monopile as the jacket structure. Second, global and local buckling is examined to address structure stability. Finally joint punching is reviewed for the jacket. Here, among others, stress concentration factors (SCF) are discussed. These SCFs are used to factorize increased loading in structure joints as a result of sudden changes of geometry.

2.9.1 Yield

To evaluate structure internal stresses a yield check is performed using classic mechanics. Yield checks are performed for ultimate limit states (ULS), these evaluate extreme environmental scenarios as described in DLCs. Here a material safety factor (γ_M) of 1,25 is used to take into account material impurities in addition to the load factor discussed earlier. Equation (2.37) shows the general formula used for yield calculation. The evaluation is successful once the allowed material yield strength (σ_{yield}) is smaller as the combined stresses from forces and moments in a respective member.

$$\frac{\sigma_{yield}}{\gamma_m}[N/m^2] > \frac{F \cdot \gamma_l}{A} + \frac{M \cdot \gamma_l}{W} \tag{2.37}$$

If stresses prove to be larger as the yield stress of the material, firstly the wall thickness of the structure is increased and only if that proves insufficient more the rigorous geometrical changes, such as a change of diameter, are made. Wall thickness changes are preferred at this stage of the design since these have a limited effect on the external loading and structure's stiffness with respect to, for example, a changed diameter.

2.9.2 Buckling

Once all members are checked for yielding, buckling is addressed in a two-step process; global and local. Most often the buckling analysis is the design driver for the brace's diameter. For both global and local buckling checks a material and load factor of 1,1 and 1,25 respectively are used. In global (Euler) buckling, instability resulting rapid collapse of the whole structure is addressed. Global buckling is said to not take place when axial forces and in- and out-of-plane moments are smaller as maximum allowable forces and moments for the specific geometry.

$$\frac{N_d}{\kappa \cdot N_p} + \frac{\beta \cdot M_d}{M_p} + \triangle n \leq 1 \tag{2.38}$$

Here N_d and M_d are the occurring factored normal force and in- and out-of-plane bending moments for the DLC, respectively. These are compared with the maximum allowable plastic compression resistance (N_p) and plastic resistance moment (M_p), resulting from the member's geometry.

In contrast to global bucking, which evaluates deformation of a complete structure due to loading exceeding buckling loads, local bucking is used for checking the possibility of local rippling in the structure caused by stresses that locally exceed limits. Local buckling is addressed using equation (2.39), here axial and circular compressive stresses, σ_x and σ_φ, are compared to the maximum allowable ultimate buckling stresses as defined by the structure's geometry.

$$\left(\frac{\sigma_x}{\sigma_{x,u}}\right)^{1,25} + \left(\frac{\sigma_\varphi}{\sigma_{\varphi,u}}\right)^{1,25} \leq 1 \tag{2.39}$$

If local and/or global analyses indicate structure failure firstly wall thickness of the respective member is increased, only if that proves insufficient other changes are made to the structure. This is done for equal reasons as discussed in the last paragraph.

2.9.3 Punching

Punching refers to joint failure as a result of sudden geometry change. The sudden changes prohibit the stress field from flowing fluently and result in stress concentrations. In this paragraph the punching analysis as proposed by the API RP2A standard of 2007 (API 2007) is used. The punching analysis is conducted in a multi-step process. Firstly the joint in question is classified as K, X, Y or combination joint. Second the joint's geometry is given a closer look to make sure spacing between the individual components and member sizes are optimal, effectively reducing effects of stress concentration. Finally, a tubular joint calculation is executed to find out if the structure holds for the chosen geometry.

Joint classification

Joints are classified under axial loading as it where in the structure. Joints are subdivided in three groups; K, X and Y. In these joints all members in the same plane are evaluated, thus a joint is effectively two-dimensional. If two planes can be drawn in a single joint an analysis is required for each individual plane in the joint. Figure 2. 24(A, B, C) show the classification for K, Y and X joints respectively.

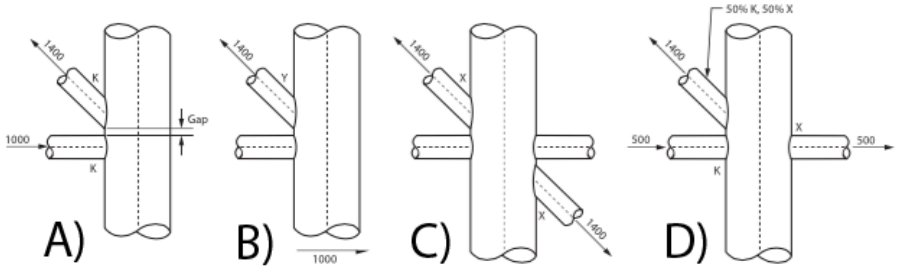

Figure 2. 24 - Joint types

In this image, the large member represents the leg on the side of the jacket and the small members are the braces that form the connection between the legs.

A brace is considered to be of the K-type (A) if axial stresses on the same side of the leg are transferred between members. In the Y-type (B) the axial stresses in the braces are transferred to shear stresses in the leg. X-joints (C) are those where the axial stresses are transferred to braces on the other side of the leg. Joint D in the respective image shows a KX joint. Here the diagonal brace is 50% K and 50% X because 50% of the stresses is converted to a member on the same side of the leg (K) and 50% of the stresses are intercepted by the horizontal member on the other side of the leg (X).

Joint detailing

Once joint types are established a closer look at the joint's geometry is needed. In the joint detailing process, effects of stress concentration are reduced as much as possible. Methods that result in lower SCFs include; keeping space between brace connections to legs, locally increasing member/leg wall thickness and maintaining reasonable brace-to-chord ratios (β). Figure 2. 25 shows the joint dismemberment used for joint detailing.

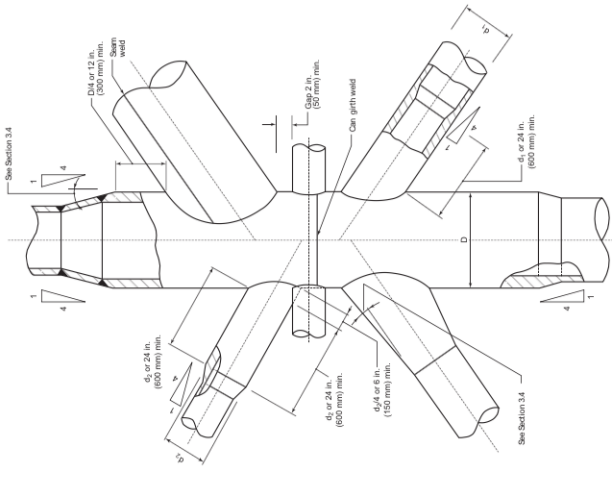

Figure 2. 25 - In-plane joint detailing

In the following paragraph, the general methodology for joint detailing is discussed. At this point 'simple joint calculation' as shown by El-Reedy (El-Reedy 2012) is treated, as this methodology is sufficient for the preliminary design phase. For more detailed joint detailing please refer to chapter 3 and 4 of the API standard (API 2007).

First, the length of local wall thickening (reinforcement) should be used as indicated in the image for each respective member. If two dimensions could constrain the reinforcement the largest one is used. Second, a minimum gap of 50 mm should exist between adjacent braces. This holds for both in-plane and out-plane braces.

Joint calculation

Basic tubular joint calculations are valid within the following criteria:

Validity of joint calculations			
	From	To	Unit
β	0,2	1	-
γ	10	50	-
θ	30	90	Degree
F_s		500	MPa
g/D		-0,6	-

Table 2. 3 - Joint calculation validation

Here β, γ and θ are found using Figure 2. 26:

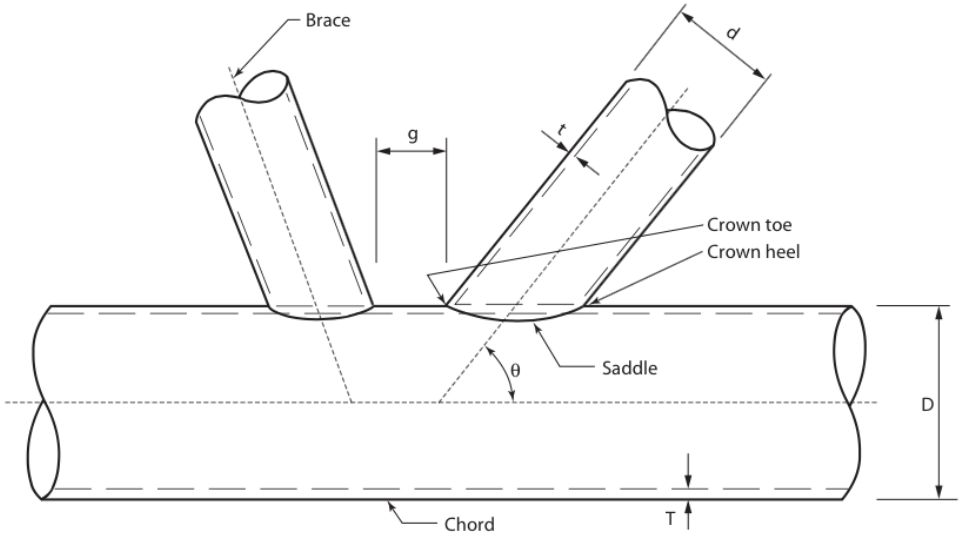

Figure 2. 26 - Joint parameters

Basic tubular connections are joints without brace overlap and having no gussets, diaphragms, grout or stiffeners. The maximal allowable stresses in the joint are a function of allowable capacity for axial brace load (P_m) and allowable capacity for brace bending moment (M_a).

$$P_a[N] = Q_u \cdot Q_f \cdot \frac{F_{yc} \cdot T^2}{FS \cdot \sin(\theta)} \tag{2.40}$$

$$M_a[Nm] = Q_u \cdot Q_f \cdot \frac{F_{yc} \cdot T^2 \cdot d}{FS \cdot \sin(\theta)} \tag{2.41}$$

Here F_{yc} is the yield stress of the chord member, FS is the safety factor, which is taken here as 1,6, T is the chord wall thickness and d is the brace diameter. Additionally, Q_u and Q_f are the respective strength and chord load factor that depend on the brace-to-chord ratio (β), their attributes are discussed on the following page.

The strength factor (Q_u) is a function of joint and loading type. Its equation for a respective loading situation is found using Table 2. 4.

	Loading	
Joint type	**Axial tension**	**Axial compression**
K	$(16+1{,}2\cdot\gamma)\cdot\beta^{1,2}\cdot Q_g$ but ≤ $40\cdot\beta^{1,2}\cdot Q_g$	
Y	$30\cdot\beta$	$2{,}8+(20+0{,}8\cdot\gamma)\cdot\beta^{1,6}$ but ≤ $2{,}8+36\cdot\beta^{1,6}$
X	$23\cdot\beta$ for β≤0,9 $20{,}7+(\beta-0{,}9)\cdot(17\cdot\gamma-220)$ for β>0,9	$[2{,}8+(12+0{,}1\cdot\gamma)\cdot\beta]\cdot Q_b$
Joint type	**In-plane bending**	**Out-of-plane bending**
K, Y, X	$(5+0{,}7\cdot\gamma)\cdot\beta^{1,2}$	$2{,}5+(2{,}5+0{,}2\cdot\gamma)\cdot\beta^{2,6}$

Table 2. 4 - Strength factor Q

Where Q_g is the gap factor that is defined by:

$$\begin{aligned} Q_g &= 1+0{,}2\cdot[1-2{,}8\cdot g/D]^3 \quad \text{for } g/D \geq 0{,}05 \\ Q_g &= 0{,}13+0{,}65\cdot\theta\cdot\gamma^{0,5} \quad \text{for } g/D < -0{,}05 \end{aligned} \tag{2.42}$$

Additionally Q_b is the geometric factor that is defined by:

$$\begin{aligned} Q_b &= \frac{0{,}3}{\beta\cdot(1-0{,}833\cdot b)} \quad \text{for } \beta > 0{,}6 \\ Q_b &= 1 \quad \text{for } \beta \leq 0{,}6 \end{aligned} \tag{2.43}$$

Once the strength factor is known, the chord load factor (Q_f) is calculated. This factor is, in contrast to the previous factor, a function of the loading. It addresses how much extra loading the chord can bear from the braces.

$$Q_f = \left[1+C_1\cdot\left(\frac{FS\cdot P_c}{P_y}\right)-C_2\left(\frac{FS\cdot M_{ipb}}{M_p}\right)-C_3\cdot\left[\left(\frac{FS\cdot P_c}{P_y}\right)^2+\left(\frac{FS\cdot M_c}{M_p}\right)^2\right]^{0,5}\right] \tag{2.44}$$

In this equation P_c and M_c are the respective nominal axial load and bending moment in the chord. Addition, P_y and M_p are the yield axial capacity and plastic moment capacity of the chord. FS is an additional safety factor, which is taken as 1,2 for the strength factor. Finally, the C coefficients 1 trough 3 are determined using Table 2. 5.

Joint type	C_1	C_2	C_3
K joint under brace axial loading	0,2	0,2	0,3
Y joint under brace axial loading	0,3	0	0,8
X joint under brace axial loading β≤0,9	0,2	0	0,5
X joint under brace axial loading β=1	-0,2	0	0,2
All joints under brace moment loading	0,2	0	0,4

Table 2. 5 - Coefficients

Now both axial force and bending induced loads are known, they are combined to find the joint interaction ratio (IR). If the value is smaller than one, the joint is tough enough to bear the loading induced by the load case in question.

$$IR = \left|\frac{P}{P_a}\right| + \left(\frac{M}{M_a}\right)^2_{ipb} + \left|\frac{M}{M_a}\right|_{opb} \leq 1 \tag{2.45}$$

Joint with locally increased wall thicknesses, overlap and grouted connection are evaluated in the detailed assessment. Their attributes are beyond the scope of this thesis. For further information about these analyses the reader is referred to the API standard (API 2007).

2.9.4 Fatigue

Due to the dynamic nature of loading induced by wind, waves and current the fatigue assessment is an important part of the structure analysis. Additionally, due to the salinity of the environment, corrosion will also promote crack growth. One way of addressing fatigue damage is by using rain flow counting. Here firstly stress intensity cycles over the lifetime of the structure are counted. Second, cycles of similar size are counted and classified according to intensity. In the third step the amount of cycles that would cause failure for a selected loading intensity are extracted from the material's S-N curve. Now, the fraction of counted cycles is calculated by dividing the amount of cycles that would cause failure over the actually counted amount of cycles. This ratio provides the inflicted damage for the evaluated stress range. Finally, the damage resulting from each different stress range is summed up to find-out the total structure damage over the lifetime of the project, failure is not expected if the resulting damage (D) is smaller than unity. These last two steps are known as the Miner's rule.

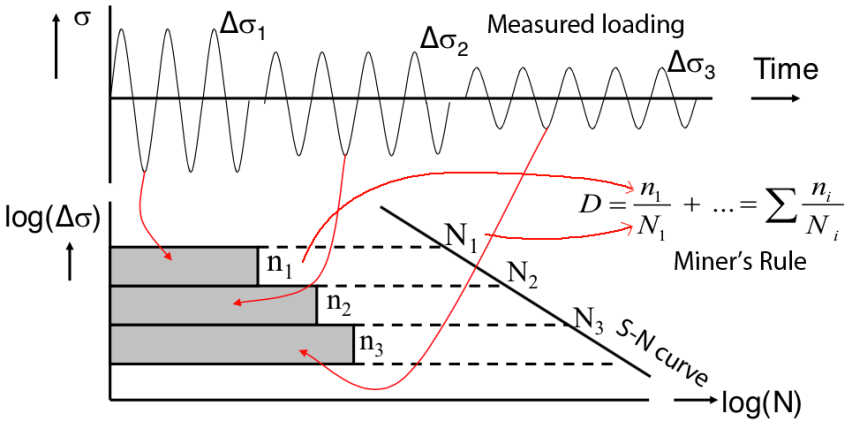

Figure 2. 27 - Fatigue assessment

However, a more careful look is required at welds due to stress concentrations. As was discussed in the last paragraph, stress concentrations are caused by sudden changes in geometry that prohibit the stress field from flowing continuously. Therefore, for each weld, a SCF is calculated for several locations along the path of the weld. These SCFs are found using Efthymiou equations, which estimate the stress intensities as a function of the joint's geometry. Additionally, SCFs can also be found using finite element method (FEM) software. Detailed environmental information is required to yield a result that converges with the actual fatigue damage that would occur along the lifetime of the project. Therefore the fatigue assessment can only be conducted once a detailed insight is granted in later stages of the design.

2.10 Roundup

The design methodology as depicted in Figure 2. 1 is completed using several iterative loops to check if design alterations did not affect the outcome of previous project steps, the geometry of the structure is finally known.

3

Engineering model

3.1 Introduction

In the previous chapter the design process for the monopole and the jacket structure are discussed. Implementation of the engineering model using this methodology is however far too extensive. A simpler model still provides results of accuracy comparable to that of TeamPlay. Furthermore, a more basic model is able to deliver results from less input data and require less computational time. These additional advantages make the model useful for the preliminary design phase, when there's still very little known of the environmental aspects of the (possible) wind farm site.

In this chapter the methodology used for the Simple Jacket Optimization Engineering Model (SJOEM) is discussed. Firstly however, design boundaries are established. These consist of load cases, safety factors and a description of the design procedure. Second, tower design is described followed by that of the jacket and foundation piles. For each of these structure parts (tower, jacket and foundation piles) its respective dynamic interaction with the environment is explained. Load interaction between parts is treated as static.

3.1.1 Model exclusions and simplifications

To maintain the limited timeframe of this thesis the following analyses are excluded or simplified:

- Natural frequency analysis (exclusion)
- Fatigue analysis (exclusion)
- Dynamic loads (simplification)
- Torsional loads (simplification)

This obviously has consequences for the accurateness of results, especially regarding the natural frequency. The writer nonetheless chose to exclude natural frequency from the thesis since on the one hand implementing a simplified analysis (like Rayleigh's stick method) would possibly not yield a result of desired accuracy. On the other hand, implementation of a more complex model lies outside the boundaries of this thesis. For completeness however, implementation of a natural frequency analysis is the main priority for future model versions. Finally, fatigue is addressed by implementation of an additional safety factor of 1,5. Which is analogue to the manner fatigue is addressed in TeamPlay.

Assuming static design loads rather than loads of dynamic nature excludes effects of time-dependency. This greatly simplifies the analysis but obviously at the cost of neglecting all time dependent events such as gusts and wave slamming loads. In an attempt to incorporate these effects alterations are made to the prescribed safety factors. These alterations are discussed in paragraph 3.1.3 Safety factors.

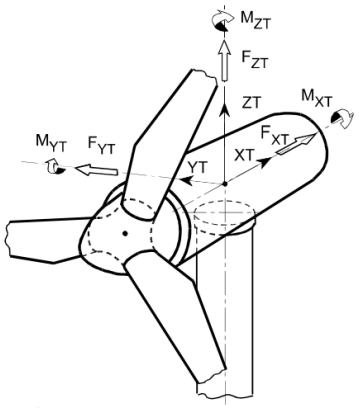

Figure 3. 1 - Global coordinate system

As already briefly mentioned on the previous page, torsional loads are excluded from the current analysis. These loads result form sideways shifting of the RNA's center of mass due to rotor movement. Not taking into account torsion effectively eliminates all F_y, M_x and M_z loads as displayed in the global coordinate system of Figure 3. 1. Forces in y-direction (F_y) are neglected as well due to not taking into account sideways movement. Obviously from here it follows that moments caused by these loads (M_x and M_z) are excluded as well. When all load simplifications are combined, the remaining loads are (global) forces in x-direction due to environmental loads (F_x), forces in z-direction due to the structure's weight (F_z) and (global) moments caused by environmental loads (M_y) plus (global) moments induced by the RNA's center of mass not being aligned with the tower's center axis (M_y).

3.1.2 Load cases

When an offshore structure is designed in practice, it's subjected to numerous load cases representing possible weather scenarios. For the engineering model however, three design load cases (DLC) are selected. These represent likely to occur extreme weather scenarios and are taken according to the International Electrotechnical Commission (IEC) (IEC 2009). In an effort to incorporate most design driving weather scenarios, three DLCs are selected. Table 3. 1 depicts load cases used to test the structure for ultimate limit state (ULS). These are picked analogue to TeamPlay to retain coherence. According to the IEC a ULS is: 'a state beyond which the structure no longer satisfies the design (performance) requirements'. However, if boundaries formulated by an ULS are breached this does not necessarily mean the structure will fail, it only means that it is unknown whether the structure will fail or not.

DLC	Turbine	Wind scenario	Wave scenario
1 (IEC1)	Operation	Rated wind speed	Maximum wave in one-year extreme sea state
2 (IEC6)	Parked	Reduced gust in 50-year average wind speed	Maximum wave in 50-year extreme sea state
3 (IEC6)	Parked	Maximum gust in 50-year average wind speed	Reduced wave in 50-year extreme sea state

Table 3. 1 - Design load cases as used in SJOEM

As a final note, loads formed as a result of sea currents are not taken into account. Sea current induced loads are excluded to retain analogy to TeamPlay. For the used jacket design procedure a monopile-like representation of the structure is created. Since a similar design method is used, it's expected that neglecting current does not have a larger impact than it would've for the monopile structure as evaluated in TeamPlay.

3.1.3 Safety factors

Parallel to the procedure for load cases, safety factors are implemented according to IEC standards as well. Since only ULSs are evaluated, their respective safety factors are adopted from the standard. Safety factors are applied separately for both environmental and gravitational loading. For gravitational loads the partial material safety factor, dynamic amplification factor and partial gravitational safety factor are used. The environmental safety factor is comprised of the material partial safety factor, dynamic amplification factor, fatigue safety factor and partial safety factor for environmental loads. The respective size of these factors is displayed in Table 3. 2.

Symbol	Name	Size
γ_m	Partial material safety factor	1.10
γ_{DAF}	Dynamic amplification factor	1.00
γ_{fat}	Fatigue safety factor	1.50
γ_{env}	Partial environmental safety factor ULS	1.35
γ_{grav}	Partial gravitational safety factor ULS	1.10

Table 3. 2 - Design safety factors adopted from IEC

As briefly mentioned in paragraph 3.3.1, fatigue is taken into account using an additional safety factor of 1.5. Furthermore, a dynamic amplification factor (DAF) of 1.5 is taken to address thrust force on the rotor nacelle assembly (RNA). For the rest of the structure a DAF of 1.0 is used, analogue to TeamPlay. Further research is needed for a better description of these factors.

3.1.4 Optimization procedure

At this point a more detailed understanding of automated design optimization is needed to understand core methodologies used in this thesis. In order to make the concept of design optimization somewhat less abstract, its application is explained using the following (simplified) example. Optimal tower dimensions are discussed for a very basic set of parameters.

Firstly, to help form a clear problem description, unnecessary parameters are eliminated. Let's assume for the example's sake that the tower only consists of one single constant diameter and constant wall thickness tube. This tube is subjected to a constant wind speed profile along its height. Furthermore, to eliminate any moments as a result of mass misalignment, the RNA's center of mass is assumed to be located directly above the center axis of the tower.

As mentioned in the introduction of this thesis, the lowest-cost structure is found for one that has the least volume. Since tower height is constrained by the rotor diameter (this is discussed extensively in paragraph 3.3), the lowest volume is found for the smallest required cross-sectional area to withstand all DLC. For this simple analysis, only external tower loads are caused by drag and its own weight. If densities of air and metal are taken constant, these forces are only a function of diameter and wall thickness. Since largest tower loads are found at the tower base, optimal area is estimated for this location. This multi variable problem is now reduced to a function with only variable being diameter and wall thickness.

Second, a closer look is given to design constraints. Obviously, the most straightforward being yielding. In order for the structure not to fail due to yield, internal stresses resulting from external loads (drag and gravitational forces) need to be lower as the material's yield stress (e.q.:(3.1)).

$$\sqrt{\left(\frac{F_x}{A}\right)^2+\left(\frac{F_z}{A}+\frac{M_y \cdot r}{I_y}\right)^2} \leq \gamma \cdot \sigma_{yield} \tag{3.1}$$

Here F_x, F_z are forces in respective x-, z- direction and M_y is the moment around the y-axis using the global coordinate system. These loads are a result of environmental (drag) and gravitational loads on the structure. Internal stresses are found by combining external loads with the tower's geometric properties: radius (r), cross-sectional area (A) and area moment of inertia (I_y). These stresses need to be equal or smaller as the material's yield stress (σ_{yield}) times a certain safety factor (γ) (smaller than one). The next criterion takes into account failure due to a sudden decrease of the structure's stiffness: buckling. The most straightforward, but rather inaccurate, relation used to describe this phenomenon is to keep the diameter over wall thickness ratio below a certain constant. This buckling criterion thus constrains the minimum allowable wall thickness for a certain diameter. The final design constrain is a rather obvious one of physical nature: the tower's wall thickness cannot be larger its radius.

Combination of these design constraints results in a range off possible diameter and wall thickness combinations for which no failure occurs. The result of this example scenario is displayed in Figure 3. 2. Here yellow striped lines indicate combinations of diameter and wall thicknesses that have in an equal cross-section area. The white area represents diameter and wall thickness combinations for which all three constrains are met. The black dot at the bottom of the image shows the diameter and wall thickness combination that passes all criteria while resulting in the lowest cross-section area. This is the solution for this particular optimization problem.

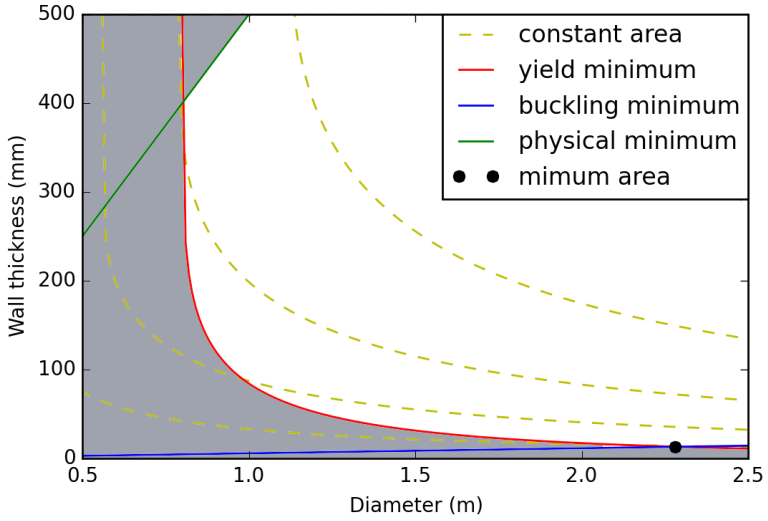

Figure 3. 2 - Minimum area

Note that dimensions calculated in the above example are actually only is a solution for the bottom of the tower. A huge volume reduction is gained if this analysis is done along different heights of the tower, resulting in a tower design with a variable diameter and wall thickness along its height.

3.1.4 Design procedure

The offshore wind support structure (OWS) evaluated in this engineering model is designed using a four-stage design process. Starting at the top (RNA), trough the bottom of the structure (foundation piles) (Figure 3. 3). For each of these stages, optimal geometry is estimated by combination of loads from the overlaying structure with environmental interactions on the respective segment. Apart from the RNA, segment geometry is found iteratively by balancing stresses from external loads allowable internal stresses. Since structure costs is proportional to material use, the lowest cost structure is found at one having the least volume (Zaaijer 2013).

To further clarify structure interactions we revert back to Figure 3. 3. In this figure blocks on the left-hand side represent the source of environmental interactions while block on the right-hand side represent OWS segments on which these loads act. Arrows indicate whether load interactions are assumed being either of dynamic (double arrow) or static (single arrow) nature. By dynamic nature it's implied that a design optimum can be found at the equilibrium between both blocks. For example, drag load on the tower is a function of both the wind speed (wind block) and the tower diameter (tower block). If optimal tower geometry is found for a certain drag load this geometry again has an effect on the initial drag load. There is thus an infinite feedback loop between the drag load and tower geometry. However, for each new iteration difference between the new and old result become smaller. A constraint is put on this iterative process to break the infinite loop. If difference between old and new results is smaller than 1 percent, the answer is accurate enough and the iterative process is terminated.

As denoted by the single arrow, no load interaction between OWS segments is assumed. This is of course not the case in practice. But since connections between segments are very stiff, the accuracy loss resulting from this assumption should be small.

SJOEM's design process is commenced as follows. Firstly, starting at the top, loads on the RNA are estimated. RNA load interaction is beyond the scope of this thesis and is therefore only a simple (static) evaluation is conducted. For DLC1, environmental loads are estimated using blade element momentum theory (BEM). RNA loads for the other two load cases are approximated by estimation of drag induced on three cylinders subjected to cross flow. Vertical loads are estimated directly from RNA mass, which is a requested model input. Second, tower loads are addressed from both RNA and wind blocks. As discussed earlier, induced drag forces on the tower are a function of both environmental conditions as structure dimensions. Optimal geometry is found iteratively. Thirdly, tower loads are combined with wave induced hydrodynamic loads. Tower loads are at this point being treated as static. Finally, both super- as substructure findings are the input to address foundation pile dimensions. Geometry found at the equilibrium of pile top loads and soil interactions.

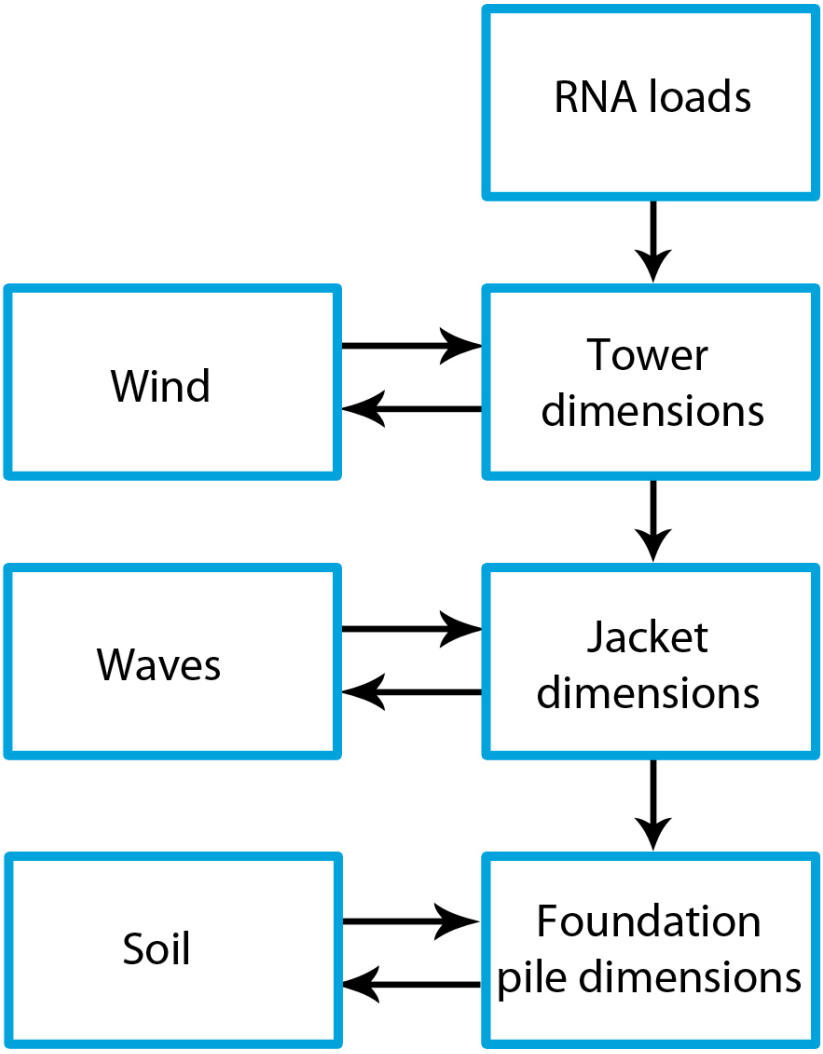

Figure 3. 3 - OWS design procedure

3.2 Design parameters

The main advantage of TeamPlay is its ability to provide good results using a limited set of input parameters. Table 3. 1 lists required input parameters as used in SJOEM. Depths are taken with respect to the still water level (SWL).

Symbol	Description	Unit
D_{rotor}	Rotor diameter	m
M_{rna}	Mass rotor nacelle assembly	kg
$C_{d\text{-}rotor}$	Drag coefficient rotor	-
V_{rated}	Turbine rated wind speed	m/s
W_{scale}	Weibull scale factor	m/s
W_{shape}	Weibull shape factor	-
H_{ref}	Reference wind speed height	m
α	Wind shear exponent	-
H_{depth}	Deepest water depth	m
HAT	Highest astronomical tide	m
H_{surge}	Maximum storm surge	m
H_1	1 year significant wave height	m
H_{50}	50 year significant wave height	m
ρ_{water}	Density of (salt) water	kg/m3
θ_{soil}	Soil friction angle	degree
ρ_{soil}	Density of submerged soil	N/m3
σ_{yield}	Yield strength of steel	Mpa
E_d	Elasticity of steel	Gpa

Table 3. 3 - Input parameters as required by SJOEM

3.2.1 Design elevations

Addression of design elevations marks the first step for evaluation of optimal structure geometry. All following equations are with respect to the SWL (H_{swl} = 0 m). Platform height (H_{int}) is found using equation (3.2) (Journée (Journée and Massie 2001)). Here 50-year maximum wave height (H_{max50}) is a function of the 50-year significant wave height (H_{50}) using expressions adopted from TeamPlay. An additional air gap ($H_{clearance\text{-}interface}$) of is added prevent any waves from reaching the platform.

$$H_{int} = H_{swl} + H_{HAT} + H_{surge} + 0,55 \cdot H_{max\,50} + H_{clearance-interface} \tag{3.2}$$

After platform height is found, nacelle height is simply determined as a function of rotor diameter plus an additional clearance of 5 meter ($H_{clearance\text{-}RNA}$).

$$H_{RNA} = H_{int} + \frac{D_{rotor}}{2} + H_{clearance-RNA} \tag{3.3}$$

3.3 Rotor nacelle assembly

For the RNA design, only a simple load assessment is conducted to address impact on the substructure. For a more detailed assessment the reader is referred to TeamPlay documentation.

RNA loads are examined for each of the three DLCs described in paragraph 3.1.2 Load cases. For DLC 1, the turbine is assumed operational at rated wind speed (V_{rated}). At this instance, the thrust force (F_t) experienced by the nacelle is at its maximum. Using an induction factor (a) of 1/3, the thrust force is simply estimated from blade-element momentum theory (BEM). In this theory, the rotor blades are described by means of an actuator disk. The disk's area (A_{disk}) is estimated from the rotor diameter (D_{rotor}).

$$F_T = \frac{1}{2} \cdot C_T \cdot \rho_{air} \cdot U_{rated}^2 \cdot A_{disk} \quad with\ C_T = 4 \cdot a \cdot \left(1 - a\right) \tag{3.4}$$

For the DLC2 and DLC3, which represent a storm scenario, a parked turbine is considered. For this scenario, blades are fully pitched and rotation is obstructed. Blades are assumed as three cylinders subjected to cross-flow. The cylinders themselves have their length set equal to half the rotor diameter and a width of 5 percent of that amount. Axial force on the nacelle is found using drag theory (e.q.: (3.5)) with a drag coefficient (C_D) of 1,2. Obviously wind speed ($U_{nacelle}$) is taken at the nacelle height, and is calculated using the power law formula introduced in chapter two. In an effort to incorporate any moments from load imbalnce, equation (3.6) is formed.

$$F_D = \frac{1}{2} \cdot C_D \cdot \rho_{air} \cdot U_{nacelle}^2 \cdot 3 \cdot \left(\frac{D_{rotor}}{2} \cdot \frac{D_{rotor}}{20} \right) \tag{3.5}$$

$$M_{T/D} = \frac{1}{3} \cdot F \cdot \frac{D_{rotor}}{3} with\ F = F_T\ or\ F_D \tag{3.6}$$

Additional RNA bending moment ($M_{y\text{-}RNA}$) as a result of mass missalignment is found using an approximation for maximal blade deflection (D_{blade}), tower bottom diameter (D_{tower_base}) and an additional constant gap of 5 meter. Equation (3.8) and (3.9) are derived using equations proposed by Zaaijer (Zaaijer 2014).

$$M_{y-RNA} = \frac{M_{RNA} \cdot g \cdot D_{overhang}}{2} \tag{3.7}$$

$$D_{overhang} = D_{blade} + \frac{D_{tower\_base}}{2} + 5.0 \tag{3.8}$$

$$D_{blade} = \frac{1}{500} \cdot \left(\frac{D_{rotor}}{2} \right)^2 \tag{3.9}$$

At this point however, the tower base diameter is still unknown. Actual calculation for $M_{y\text{-}RNA}$ is addressed during the tower design phase, which is discussed next.

3.4 Tower

3.4.1 Design procedure

After establishing RNA loads data is, except for moments due to mass misalignment, treated as static input for the tower design. The tower is split in ten segments of equal height. Then, for each of these segments, minimal required cross-sectional area is determined using yield, buckling, physical and penalty constrains. Since loads increase for every segment as one moves towards sea level, cross-sectional area increases as well. Analogue to the example procedure discussed in 3.1.4 Optimization procedure, maximal tower wall thickness is constrained to not become larger as its radius. A final constraint limits the maximal reachable diameter over wall thickness ratio. This 'penalty constraint' prevents run-off to very large diameters and very small wall thicknesses due to limitations of used buckling theory. This phenomenon is discussed more extensively along the course of this paragraph.

3.4.2 Yield assessment

For any segment i, geometry is firstly tested for material strain limits. Segment top loads are combined with drag and weight loads to establish bottom loads. Obviously, loads for the first segment are adopted from the RNA assessment. For each other segment, top loads are equal to bottom loads of the one above it (segment i-1). In an effort to reduce model complexity, gravitational loads on an arbitrary segment are estimated using parameters obtained from the former segments rather than determining them iteratively. Since diameter and wall thickness changes are rather small from element to element only a small error is expected as a result of this assumption.

The equations used for one single element analysis are displayed in equations (3.10) to (3.13). Subscripts x-, y- and z- represent loading direction in the global coordinate system introduced at the beginning of this chapter. In these equations, segment height ($H_{segment}$) and diameter ($D_{segment}$) are combined with material properties (ρ_{steel} for density of steel) and previously introduced constraints to find out loads using equation (3.1). Wind speed for each segment is determined as a function of height and DLC using drag equations similar to those introduced for DLC2 and DLC3 of the RNA assessment. In these equations segment diameter ($D_{segment,i}$) is evaluated iteratively since its required as input to address drag loads.

$$F_{x,i} = F_{x,i-1} + \frac{1}{2} \cdot C_d \cdot D_{avg,i} \cdot \rho_{air} \cdot U^2_{segment,i} \cdot H_{segment} \tag{3.10}$$

$$F_{z,i} = F_{z,i-1} + g \cdot \rho_{steel} \cdot \frac{\pi}{4} \cdot \left(D^2_{avg,i} - \left(D_{avg,i} - 2 \cdot t_{segment,i-1} \right)^2 \right) \cdot H_{segment} \tag{3.11}$$

$$M_{y,i} = F_{x,i-1} \cdot H_{segment} + \frac{1}{4} \cdot C_d \cdot D_{avg,i} \cdot \rho_{air} \cdot U^2_{segment,i} \cdot H^2_{segment} + M_{y-RNA} \tag{3.12}$$

$$D_{avg,i} = \frac{D_{segment,i} + D_{segment,i-1}}{2} \tag{3.13}$$

However, in order to find out moments induced by misalignment of the RNA's center of mass with the tower's center axis ($M_{y\text{-}RNA}$), tower bottom diameter needs to be known. For every segment, this value is estimated by predicting tower base diameter using linearization with tower top diameter (D_{tower_top}) of 3 meter, tower height (H_{tower}) and segment height:

$$D_{tower\_base} = H_{tower} \cdot \frac{D_{segment,i} - D_{tower\_top}}{H_{segment,i}} + D_{tower\_top} \tag{3.14}$$

At this point above-discussed loads result in the combination of segment diameter and wall thickness to withstand yield. For example, using equation (3.1), a curve similar to the red one in Figure 3. 2 is found. Connecting mass misalignment with tower diameter effectively puts a new constrain on the diameter. This results in smaller tower diameters, thus confirming more geometry as found in practice. There is however a trade off; on the one hand a small diameter reduces segments loads due to less inflicted drag (3.10) *plus* RNA to tower mass misalignment (3.7) while on the other hand larger diameters have a higher stiffness, making the structure better able to withstand these loads.

3.4.3 Buckling assessment

As discussed at the introduction of this paragraph, each segment is subjected to a buckling analysis in addition to a yield check. As discussed in chapter 2, two phenomena can cause the structure to buckle. These are 'global' and 'local' buckling. Global buckling problems arise whenever the 'slenderness' of a structure falls below a certain limit. This causes the complete structure to collapse (hence 'global'). Slenderness a function of the structure's geometry and the way it's connected to the outside world. Local buckling on the other hand is caused by (local) structure imperfections. Examples of such imperfections are sudden geometry changes, welds and even material imperfections. These local changes in geometry create stress concentrations that cause the structure to collapse.

DNV proposes a method wherein both failure modes are addressed (DNV 2013). Using this method, axial forces and moments are combined and compared to a certain (Euler) critical buckling stress. This critical buckling stress is, among others, dependent of the tower's geometry (slenderness) rather than from only the materials yield stress. This method does however not completely describe the actual case since it does not take into account any effects of transversal loads. This procedure is nonetheless a widely accepted (preliminary) design approach.

For each segment, it's assumed that its bottom is clamped in a vice, prohibiting both movement and rotation. For length, the total tower height is taken rather as the distance from the RNA to the bottom of the segment. Using the distance from the RNA to the segment's bottom would result in the theory not being valid due to exceeding the slenderness limits a proposed by the standards. Finally, the sum of axial loads (3.11) and moments (3.12) previously calculated for the bottom of the segment is assumed to act at the top of the tower. These assumptions are obviously very conservative but are the only way bucking can be addressed without the use of finite element methods (FEM) or other extensive methods.

Unfortunately, implementation of theories discussed above resulted in large diameter and small wall thickness combinations. One would expect that for larger diameters, local buckling criteria would push wall thickness size. This should effectively create a boundary for the optimization approach such that a minimum area is found. Multiple buckling theories as proposed by other standards ((ABS 2011), (API 2007) and (GL 2012)) produced similar results. Therefore against expectations, buckling theory as proposed in these standards does not serve as a suitable design driver but should rather be used as a quick check for correctness.

Since buckling theory proved unfulfilling an additional local buckling (penalty) constraint is implemented using equation (3.15).

$$\frac{D_{segment}}{t_{segment}} = 200 \tag{3.15}$$

This is an altered version of TeamPlay's local buckling criterion of 175 for a (submerged) monopile structure. The slightly altered ratio is chosen over the original one because hydrostatic loads on the submerged monopile are not present on the tower.

3.4.4 Optimization approach

Optimal area of any cross section is found using the 'basin hopping' algorithm form Python's Scipy module. Basin hopping theory uses the sequential least square method to find multiple local minima of a certain function range. Once all minima are found, the global minimum is selected and forwarded as solution. Basin hopping is chosen over the function minimizing sequential least squares module 'fmin_slsqp' as used in TeamPlay because this method provided inaccurate result due to convergence to local minima. Obviously the minimum area is not found by solely varying a diameter, a second parameter should be addressed; wall thickness.

For each diameter, an accompanied wall thickness is calculated using Brent's theorem. By using Brent's theorem the value of a certain variable (in this case the wall thickness) is found when the function solution is zero. This zero implies a balance is found. This is, in this case, the balance between external stresses and material yield strength. For each inserted diameter, this theorem is consulted three times: for yield, buckling and the penalty function. For these functions, required wall thickness is calculated for each load case. The largest one among answers finally is forwarded as the solution of that particular optimization step. This procedure is graphically represented in Figure 3. 4.

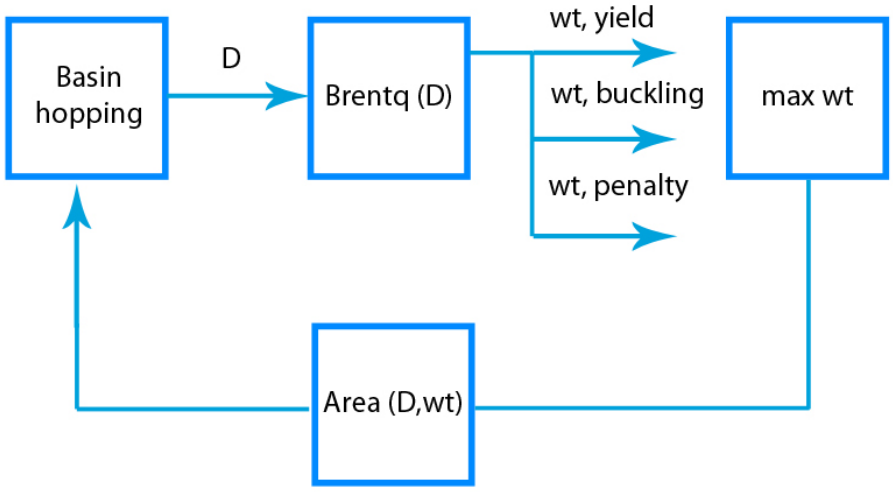

Figure 3. 4 - Simplified optimization procedure for diameter (D) and wall thickness (wt)

As a final note the importance of discussed penalty functions is emphasized. Without the use of these functions, solutions result in segment geometry with very large diameters and very small wall thicknesses. One such an example is depicted in Figure 3. 5. For clarity reasons, only procedure for DLC1 is depicted here. Since this DLC 1 is the most severe for the tower; these results can often be viewed as design driving. In the figure, yellow dotted lines indicate diameter and wall thickness combinations resulting in equal area.

In the figure it's found that, without the using the penalty function, resulting tower diameter would be more than nine meter with a wall thickness of two centimeter. With penalty limit, the tower base would have a diameter of six meter, which confirms more to practice.

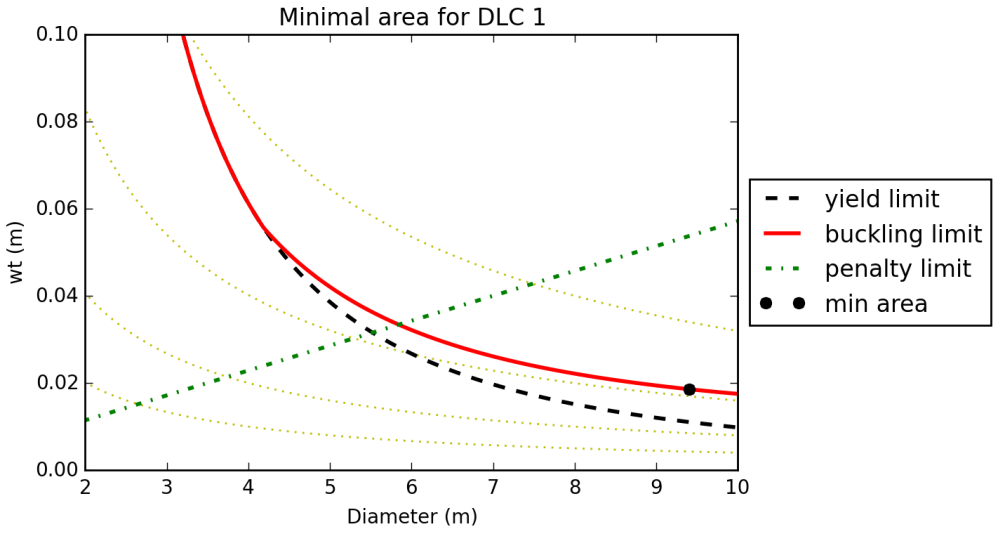

Figure 3. 5 - Minimal area optimization

3.5 Jacket

3.5.1 The quasi-static model

For the jacket a 'quasi-static in-place behavior for a steel space frame structure' design is used as proposed by Vugts (Vugts 2002). Here 'quasi-static' refers to the element of time only being partially (quasi) addressed. Quasi-static behavior is governed by the following equation:

$$\vec{F}(t) = [K] \cdot \vec{x}(t) \tag{3.16}$$

Where [K] is the stiffness matrix, x is the vector for structural deformations and F is the vector for applied external loads. Both x and F are time dependent. This assumption implies that loads acting on the structure are, at all times, equal to loads experienced by the jacket and result in a certain deformation. Since gravitational forces are constant in nature, they are concerned as static rather than quasi-static. According to Vugts (Vugts 2002) loading of the addressed type of space frame can be described using the proposed simplified model rather than a dynamic one: 'Most offshore structures are comparatively stiff in relation to the range of wave frequencies present in natural seas, which is the most relevant and most important source of environmental excitation, i.e. at any point in time the response is simply proportional to the load acting at that time'.

3.5.2 Space frame configuration

In an effort to further reduce complexity, the space frame is addressed as a plane frame, thereby effectively reducing the analysis from three to two dimensions. All loads are assumed to act only in the plane of the frame. As for load directions, environmental loads are assumed to act fully horizontal on the plane while gravitational loads are assumed to be of vertical nature. Using these assumptions loading of the jacket's members can firstly be addressed separately for the environmental and gravitational loading and then simply be combined to find out combined loading for the respective load case.

Furthermore, in contrast to the monopile structures where load direction is irrelevant due to rotational symmetry, the jacket is reviewed for two directional loading scenarios: 0 degree and 45 degree, with respect to (horizontal) environmental load direction. For both these scenarios, aerodynamic and hydrodynamic loads are assumed to be parallel and uni-directional, thereby making them additive. This results in the most extreme environmental loading scenario per load case. For clarity reasons, this loading scenario is shown on the left-hand side in Figure 3. 6. Each arrow represents added loading from aerodynamic and hydrodynamic origin for either the 0 degree or the 45 degree inflow scenario. The right-hand side of the figure depicts the resulting 2D plane frames that are used per load assessment. Furthermore, note the leg numbering on the left side of the image. This numbering is used later in this chapter.

The frame itself is modeled using well known idealized line elements along the center axis of all members. The connection points between braces and legs, the joints, are taken as hinges and thus do not transfer moments. Loads on the frame exclusively takes place at these joints and are referred to as being nodes in further mathematical description of the model.

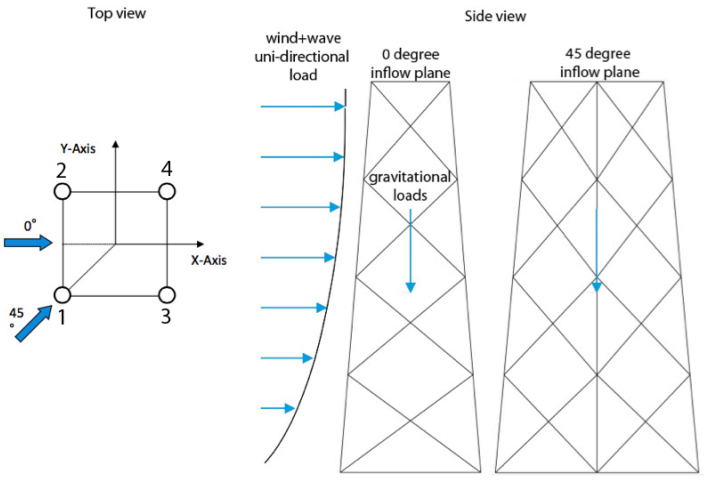

Figure 3. 6 - Directional jacket planes

3.5.2 Optimization constants

In order to find out optimal jacket configuration for given environmental conditions, an iterative process is again used to find out respective optimum leg/brace diameter and wall thicknesses for each bay. The goal here is to keep structure costs at a minimum by estimating the least amount of required material to withstand all DLCs. The number of legs, bracing type and leg batter is currently not addressed in the optimization process. A four-legged X-bracing type configuration is chosen with a 1:7 leg batter angle (θ_{batter}) as displayed in Figure 3. 7. These are commonly used design parameters according to industry practice as explained by Reedy (El-Reedy 2012).

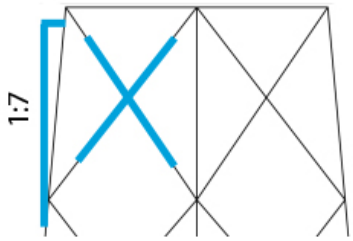

Figure 3. 7 - Leg batter and bracing type for 45-degree view

A wireframe structure is constructed using parameters introduced above. These serve as the backbone of the rest of the sequence. The wireframe is not part of the automated optimization procedure.

The wireframe structure is created as follows. Firstly, top and bottom width of the jacket are determined using design elevation height, tower diameter and constants discussed in this sub-paragraph. A wireframe of large width is desired to achieve high structure stiffness. However having a too large width would result in a larger overturning moment and unnecessary costs. A commonly used industry rule of thumb is to set the jacket top width (L_{TOP_jacket}) equal to the tower diameter plus an extra three-meter maneuver space for the maintenance crew ($L_{manouvre}$) on either side of the platform (e.q.: (3.17)). Bottom width (L_{BOT_jacket}) is found using the top width, leg batter and jacket height (H_{jacket}) (e.q.:(3.18)). Jacket height is equal to the distance from the mudline to interface level. This relation is found in the previous chapter using wave elevation levels and water depth (e.q.:(3.2)). Note that the batter angle is divided by the square root of two to since it's denoted at a 45-degree angle (Figure 3. 7).

$$L_{TOP\_jacket} = D_{tower\_base} + 2 \cdot L_{manouvre} \tag{3.17}$$

$$L_{BOT\_jacket} = L_{TOP\_jacket} \cdot H_{jacket} \cdot \frac{2 \cdot \theta_{batter}}{\sqrt{2}} \tag{3.18}$$

Second, the number of bays is estimated from the brace angle that comes closest to 40 degrees for each bay. This angle is desired according to industry proven rules of thumb (El-Reedy 2012). A smaller brace angle would result in large punching loads while a larger angle has a negative effect on loading caused by wave slamming. For the current model, each bay has a constant bay angle and height rather than changing ones. It's however recommended that future model versions incorporate changing bay height to confirm with designs in practice.

Since brace length is simply estimated using geometric relations, the only remaining unknowns are member diameter and wall thickness. Discovering their combination is the core task of the engineering model.

3.5.3 Initial-guess parameters

Before loads on the jacket can be determined some initial guess dimensions are needed. According to industry practice, a preliminary leg diameter of one meter is used. Brace diameter is determined as a function of leg diameter. To avoid large stress concentrations as a result of leg-to-brace diameter differences, brace diameter is simply set to 60 percent of leg diameter. This ratio is maintained throughout the optimization process. The only remaining unknowns are now the leg and brace wall thickness. Their initia guess values are found by maintaining a respective diameter over wall thickness (D/wt) ratio. This is 60 for jacket legs and 40 for braces, as proposed by oil and gas literature.

3.5.4 Optimization sequence

Leg and brace geometry is determines using a process that closely resembles that is used to address tower geometry. Hydrodynamic loads acting on a member are found using the Morison equation (eq.: (3.19)). Where the first term in the equation describes inertia loads as a result of obstructed wave momentum as waves are prohibited to move in preferred direction. The mass coefficient (C_m) is set to two, analogue to TeamPlay. Note that this term is a function of wave particle acceleration ($\dot{u}$) rather than wave particle speed (u). Furthermore, obstructed water particle volume ($V_{morison}$) is needed. The second term of the equation describes drag load caused by water particles exerting friction on the structure's occupied space as they move along it. The distance particles have to move around the object characterizes drag load. Hence, here not the volume is required but rather the projected area ($A_{morison}$), which is perpendicular to the flow direction. However, using only the projected area there would be no distinction between flow along a square slab or a cylinder. Namely, for equal width these would have the same projected area. To take into account these differences the drag coefficient (C_d) is introduced. Since all members are circular they have an equal coefficient of 0.4, which is taken equal to that of TeamPlay.

$$F_{morison} = \rho_{water} \cdot C_m \cdot V_{morison} \cdot \dot{u} + \frac{1}{2} \cdot \rho_{water} \cdot C_d \cdot A_{morison} \cdot u \cdot |u| \tag{3.19}$$

Inspection of the Morison equation implies an optimum can be found between external loads and internal stresses. On the one hand, increasing member diameter will result in a lower structure weight due to a smaller required wall thickness for the same area moment of inertia, but on the other hand also have a negative effect since it would result in larger induced wave loads. This is exactly the same balance problem as that of tower segment optimization. Obviously, wave loading exerted by water particles is obviously much larger as those of drag loads caused by air because their respective densities vary by a factor of 1000.

The respective optimization dimensions for legs and braces are, among others, found using yield and buckling analyses. For each bay, yield stresses are determined using the largest compressive and tensile stresses. Since buckling does not occur in members subjected to tensile loads this check is only performed for members subjected to compressive loads.

3.5.5 Design procedure

Designing an optimal support structure for minimal required mass is a somewhat more challenging task than as the tower. The following four stages govern jacket design. In an effort to get a clearer insight in these stages they're broken down further to in eight steps. These are discussed extensively during the course of this paragraph.

The jacket structure is designed according to the following stages:

1. Estimate external loads on structure
2. Determine internal member loads
3. Update dimensions from internal loads
4. Revert back to step one until optimal solution is found

These stages are further broken down to the following eight distinct steps:

1. Applied external loads (stage 1)
2. Section forces along height of structure (stage 1)
3. Nodal loads (stage 1)
4. Internal forces in frame members (stage 2)
5. Member dimensions from yield and buckling checks (stage 3)
6. Sleeve dimensions to prevent punching effects (stage 3)
7. Update dimensions and repeat steps one trough five until differences between results become 'small' (stage 3)
8. Gather loads and geometry to determine mudline loads for foundation pile assessment.

Step 1: Applied external loads

As quick recap, external structure loading is addressed per load case. Furthermore, as a result of the jacket's symmetric character, for each load case environmental loading is addressed for both the 0- and the 45-degree inflow angle. Additionally, gravitational and environmental loads are assumed to have no interaction and are investigated separately. Thus, per load case three load assessments are considered; environmental loading for 0 and 45 degree inflow *plus* gravitational loading. Resulting in a total of 9 investigated cases. Once separate cases are known, environmental and gravitational loads are combined to yield total load scenario per inflow angle per load case.

Gravitational loading

Gravitational load is the most straightforward among the three considered cases since it's independent of time and place; it's only function geometry. Gravitational loads are estimated per bay and assumed to act along the center of the structure, eliminating induced moments in the global analysis. For the local member load analysis, gravitational loads obviously would cause moments in the members. However, since the local effects of member weight are small with respect to global structure loads, this effect is neglected. This results in bay weight only having only affecting the bay below it.

Loads are estimated using the following equation where bay volume (V_{bay}) is the space occupied by metal for any bay consisting of 4 legs and 8 braces:

$$F_{BAYgrav} = g \cdot \rho_{steel} \cdot V_{bay} \tag{3.20}$$

Furthermore, an extra weight term is introduced at the interface level to take into account the additional weight of the access platform. The platform is approximated as a square slab with length equal to the top of the jacket and a height of 25 centimeter:

$$F_{INTgrav} = g \cdot \rho_{steel} \cdot \frac{L^2_{TOP\_jacket}}{4} \tag{3.21}$$

Environmental loading

External loads are estimated using the Morison equation, which requires input from both the structure geometry and wave kinematics. The procedure proposed in this paragraph is a combination of Vugts (Vugts 2002) and Vugts (Vugts 2001). The first reference proposes a simple model to describe complex jacket geometry a single (mono) pile experiencing equivalent hydrodynamic loads. Then, using the second paper, Morison loads for the equivalent pile are found using Airy wave theory.

Figure 3. 8 depicts the process used to estimate hydrodynamic loads. In this simplified model, wave velocity (u) and acceleration (ů) are found as a function of depth (d), wave height (H) and period (T) and are combined with pile diameter (D) to find out induced loads.

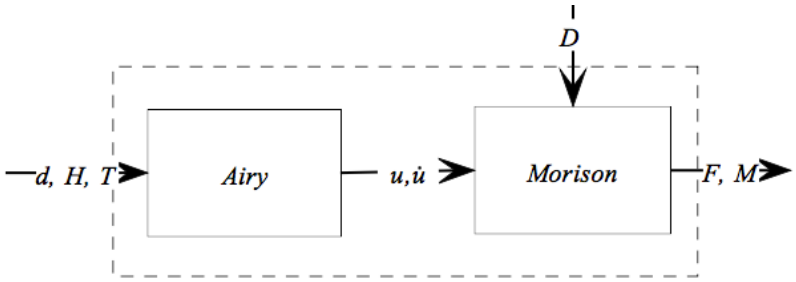

Figure 3. 8 - Steps to determine hydrodynamic forces and moments

In an effort to reduce load complexity, the jacket's legs and braces are represented per bay as an assembly of vertically stacked tubes aligned with the center of the structure. Each tube segment has its diameter set such that it would have an equal drag/inertia load exerted as if it where the original assembly of 4 legs and 8 braces. Here the objective is to only estimate horizontal induced wave loading over the height of the structure, this method would not be successful for representation of non-horizontal loads.

Obviously, the ultimate assumption here is that members are placed at the center of the structure. This neglects effects of spatial separation. However, according to Vugts (Vugts 2002) this assumption results in a more conservative load estimation. Loads found using this procedure are thus always higher than actual loads. Thus no failure is expected as a result of this assumption.

Both drag and inertia equivalent diameters (D_{eq}), as required for the Morison equation, are approximated as a function of each member's diameter (D), brace angle (θ_{brace}) and its position with respect to the particle flow direction (Table 3. 4). The total equivalent diameter is the sum of all members per bay (e.q.(3.22) and (3.23).

Orientation	**Parallel to wave direction**		**Perpendicular to wave direction**	
	Drag	Inertia	Drag	Inertia
Vertical	$D_{eq} = D$	$D_{eq} = D$	$D_{eq} = D$	$D_{eq} = D$
Horizontal	0	0	$D_{eq} = L$	$D_{eq} = \sqrt{D \cdot L}$
Diagonal	$D_{eq} = D$	$D_{eq} = D$	$D_{eq} = \frac{D}{sin(\theta_{brace})}$	$D_{eq} = \frac{D}{\sqrt{sin(\theta_{brace})}}$

Table 3. 4 - Member equivalent diameter

$$D_{eq\_drag,tot} = \sum_{i=1}^{n} D_{eq,member-i}\Big|_{Drag} \tag{3.22}$$

$$D_{eq\_inertia,tot} = \sqrt{\sum_{i=1}^{n} D^2_{eq\_inertia,member-i}}\Big|_{Inertia} \tag{3.23}$$

For example, the resulting equivalent drag ($D_{eq\_drag,tot}$) and inertia ($D_{eq\_inertia,tot}$) expressions, for a 0 degree inflow angle of a certain bay, are displayed in equation (3.24) and (3.25) as a function of brace angle, leg- and brace diameter and flow alignment. In the following two equations, perpendicular and parallel signs are used to emphasize member alignment with respect to flow direction.

$$D_{eq\_drag,tot} = 4 \cdot D_{leg} + \frac{4 \cdot D_{brace}}{sin(\theta_{brace})}\Big|_{\perp} + 4 \cdot D_{brace}\Big|_{//} \tag{3.24}$$

$$D_{eq\_inerta,tot} = \sqrt{4 \cdot D^2_{leg} + 4 \cdot \left(\frac{D_{brace}}{\sqrt{sin(\theta_{brace})}} \right)^2 \Bigg|_{\perp} + 4 \cdot D^2_{brace}\Big|_{//}} \tag{3.25}$$

However, for the 45-degree inflow angle, wave direction is neither parallel nor perpendicular to the members. Therefore, for this particular case, a new formulation for inclined members is created. This new term is approximated as half the parallel term plus half the perpendicular term.

Graphically the representation from a multiple member structure to a single member structure with varying diameter (per bay) would look something like that of Figure 3. 9.

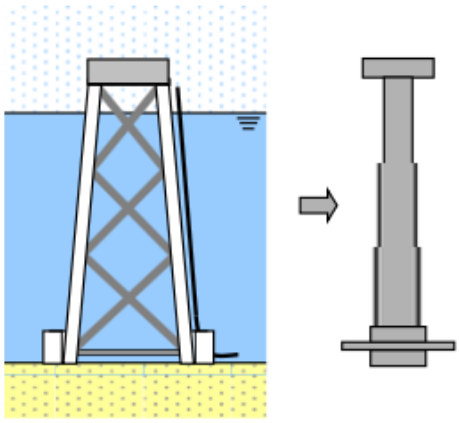

Figure 3. 9 - Equivalent stick model

Since the equivalent stick has a form equal to that of a monopile, the Morison load estimation can directly be adopted from TeamPlay instead having to create a new set of equations. Starting at the top bay, drag and inertia loading is estimated using the new equivalent stick model. Water particle velocities are determined per load case and vary as a function of depth, wave height and wave number. Finally, since drag and inertia terms are ninety degrees out of phase, the root sum square is taken to yield maximal occurring Morison loads (Zaaijer 2013).

Step 2: Section loads along the height of the structure

Once external loads are established, a closer look is given to the space frame load distribution as a first step to determine individual member loads. At this point external forces and moments are known. However point of engagement of these loads is still unknown. These are however found by examining the relation between force and moment of the expressions adopted from TeamPlay.

Cross-section method

In the following steps the 'cross-section method' as proposed by Vugts (Vugts 2002) is applied to find out individual member loads. This method helps estimate loads using several cross-sections along horizontal planes. Then using these cross-sections, individual (internal) member loads are found by balancing them with external loads. This method requires all external loads to be relocated at the nodes at top and bottom of a respective bay rather than being distributed over it, as is the case in the physical world. Finally, additional cross-sections just above and below the vertical plane where external and internal loads are balanced to reveal individual member loads. This final step will be discussed more extensively in step three. For now, focus is attainted to find-out what loads act on cross-sectional planes such that they are equal to external forces and moments of a respective bay.

Load relocation

For any bay 'i', the following external loads are found as a result of step one:

1. Morison force in x-direction ($F_{morison,i}$)
2. Morison moment induced by the forces of bullet 1 ($M_{morison,i}$)
3. Bay weight ($F_{gravity,i}$)

When observing Figure 3. 10, in order to achieve a moment balance at the bottom bay cross-section, the top load times the bay height needs to be equal to the moment induced by hydrodynamic loads (eq.:(3.26)). Evidently bottom load is thus equal to the Morison load minus the bay top load (eq.:(3.27)). The moment induced by hydrodynamic activity is fully experienced by the bottom of the bay thus is completely transposed here (eq.:(3.28)). Finally the bay weight is transposed to the bottom as well using the same analogy (eq.:(3.29)).

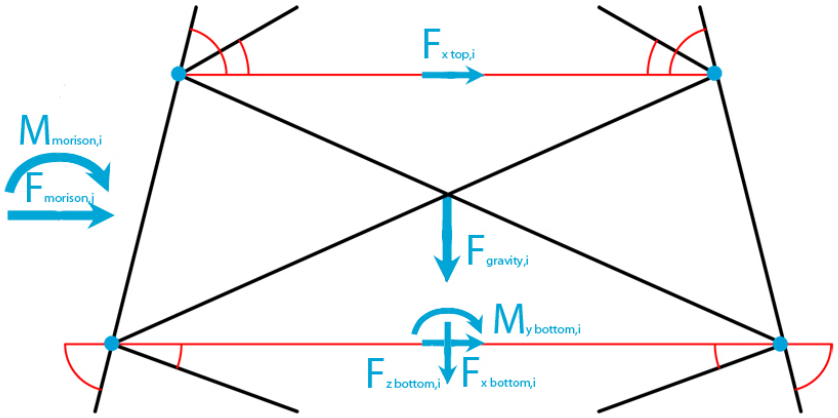

Figure 3. 10 - Load distribution to bay sides

$$F_{x\_top,i} = \frac{M_{morison,i}}{H_{bay}} \tag{3.26}$$

$$F_{x\_bottom,i} = F_{morison,i} - F_{x\_top,i} \tag{3.27}$$

$$M_{y\_bottom} = M_{morison,i} \tag{3.28}$$

$$F_{z\_bottom} = F_{gravity,i} \tag{3.29}$$

Note that the loading description as displayed above is that of a single bay. The total loading scenario is achieved by adding these single bay loads to their respective counterparts of previous bays. By doing so, the loading situation as displayed in Figure 3. 11 is found for environmental loads. Note that here, as previously discussed, all vertical forces are assumed to only act at cross sectional planes between bays (black dotted lines). In the figure, red lines indicate newly made cross-sections to estimate individual member loads from these section loads. This is the main topic of the following section. When summing all external forces the bottom loads are found. The sum of horizontal forces at the base is referred to as base shear (F_b). The sum of moments at the mudline is the overturning moment (M_{oe}).

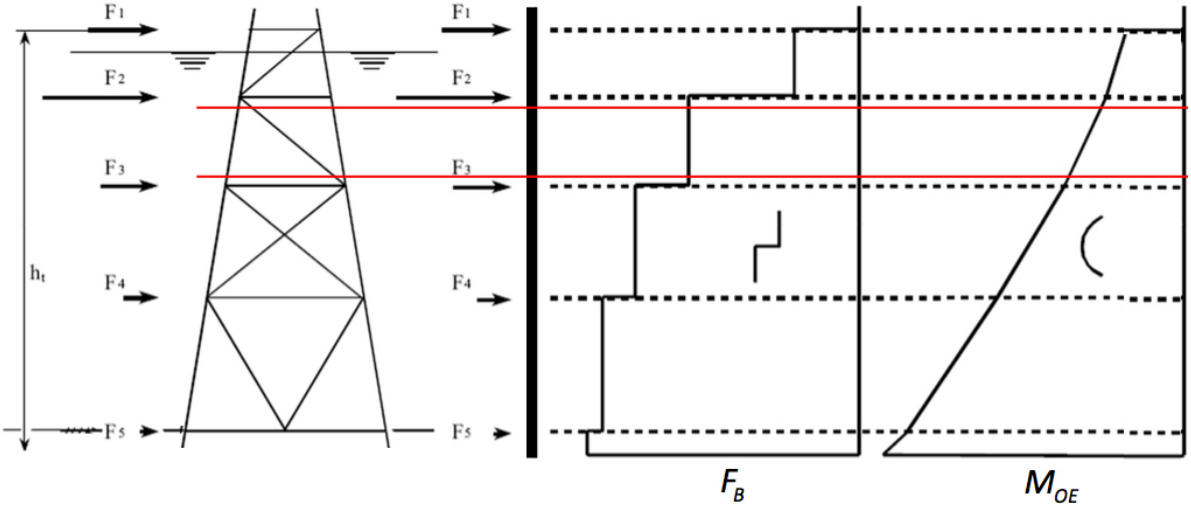

Figure 3. 11 - Load distribution along jacket

Step 3: Nodal loads

Member loads are determined using new horizontal cross sections slightly spaced outside the location of section loads (back dotted lines). These are located at the red lines in Figure 3. 11. At this point external loads are balanced with internal member forces for each of the four members crossing such a plane (one red line). This however raises a problem; the system is over determined because it's connected at four locations (the members) rather than two, which is required to estimate load distribution. Therefore the following set of assumptions is created such that member loading can be addressed correctly:

1. Equal load distribution between the front and back node.
2. All joints (nodes) are assumed to be connected using hinges.
3. Loads only act in axial direction

The first assumption effectively separates load interactions between the front and back node of a cross-section. Where 'front' and 'back' is taken with respect to the stream direction (Figure 3. 6). By doing so, only a single load balance is required at each node, rather than one for the whole cross section plane. Second, by assuming members are connected using hinges all moments are effectively converted to forces, reducing the system's required degrees of freedom (DOF). At this point the system is still underdetermined since the direction of internal loads is unknown. By assuming load transfer is only in axial direction of a member (assumption 3) the required DOF of the system is again reduced by one, this time making it fully determined. Using the previous set of assumptions, the problem is now effectively reduced from a two-dimensional undetermined model to a one-dimensional determined one.

Frame conversion

For the sake of comparing each inflow angle situation, both inflow scenarios are represented in equal 2D form. Obviously the easiest representation of the frame is for the 0 degree inflow angle (Figure 3. 6). To obtain the desired two-dimensional loading situation, loads are spread over the structure using symmetry relations. Figure 3. 12 shows the top view of an arbitrary vertical cross-section with node numbering one trough four (introduced in Figure 3. 11). From left to right, the image shows steps taken to convert external Morison forces to equivalent nodal loads. Thus, for the Morison load in x-direction acting on this plane (F_x), a quarter of force is exerted on each of the four nodes. Since a member only experiences axial loading these loads are not transferred to members perpendicular to these. This effectively decouples the two bottom nodes (1 and 3) from the two at the top (2 and 4), allowing the whole jacket being modeled by a single 2D side view plane.

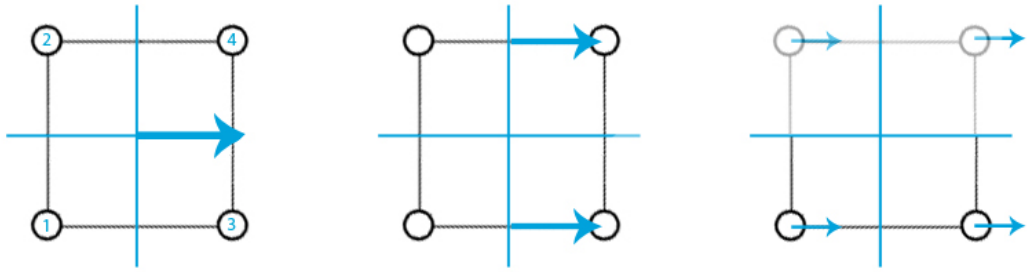

Figure 3. 12 - Steps taken to convert loads in the 3D space frame to single equivalent nodal ones for the 0-degree inflow scenario: 1) Horizontal (Morison) shear force acting on the plane, 2) Shear force spread to sides of the cross-section, 3) Forces applies to single nodes as used in force balance

Using the same procedure, vertical load on a single node is equal to one fourth of the total external vertical force acting on the cross-sectional plane (F_z). For bending (or overturning) moments (M_y) experienced by a plane, a slightly different approach is needed. Firstly, the bending moment is equally divided over the two top (2 and 4) and bottom (1 and 3) nodes of the plane of Figure 3. 12. The moment is converted to equivalent loads at the two top/bottom nodes; one on the left (node 1 and 2) and one on the right side (node 3 and 4). The left nodes (1 and 2) experiences a pulling force equal to the moment acting on that side divided by the width of the bay cross-section (W_{bay}). Obviously, the right nodes (3 and 4) experience an equal force but in the opposite direction.

Equations (3.30) trough (3.31) display the resulting load contribution on each of the four nodes. Loads are taken absolute; notation 'Morison' and 'gravity' indicate respective load origin and subscripts 0 (and in the following section 45) represent inflow direction case. Subscripts F_x, F_z and M_y indicate the origin of nodal loads from external loads. For example, F_{Fx} is the load experienced by a node as a result of the external force induced by hydrodynamic activity on a certain cross-sectional plane.

$$F_{Fx,1234} = \left.\frac{F_{x0}}{4}\right|_{morison} \tag{3.30}$$

$$-F_{Fz,1234} = \left.-\frac{F_z}{4}\right|_{gravity} \tag{3.31}$$

$$F_{My} = F_{My,12} = -F_{My,34} = \left.\frac{M_{y0}}{2 \cdot W_{bay}}\right|_{morison} \tag{3.32}$$

The resulting horizontal and vertical forces are displayed below. Subscripts indicate loading direction either being horizontal (h) or vertical (v). Numbering 1 trough 4 link the node to the equation that it is used for. Using a local coordinate system, where positive values indicate vectors pointing either upwards or to the right, it follows that for node 1 and 2 the resulting force is the difference between the gravitational and moment induced force component. For node 2 and 3 the sum is taken for the two components. This hints that, for this situation, the back of the frame (node 3 and 4) is exposed to a greater loading as the front (node 1 and 2).

$$F_{h,1234} = F_{Fx,1234} \tag{3.33}$$

$$F_{v,12} = -F_{Fz,1234} + F_{My} \tag{3.34}$$

$$F_{v,34} = -F_{Fz,1234} - F_{My} \tag{3.35}$$

Second, the 45-degree inflow configuration is addressed. For a certain shear force, the procedure as displayed in Figure 3. 13 is encountered for any cross section parallel to the mudline. Obviously, the same procedure is adopted for a moment distribution corresponding to the one formerly discussed. Evidently this method is slightly different to the one for shear force distribution. Only the outermost two nodes (1 and 4) are affected by the overturning moment since the respective lever arm is zero at the other two nodes (2 and 3). Additionally, since original shear loading is neither parallel to perpendicular an additional division by the square root of two is used to align loads with member directions.

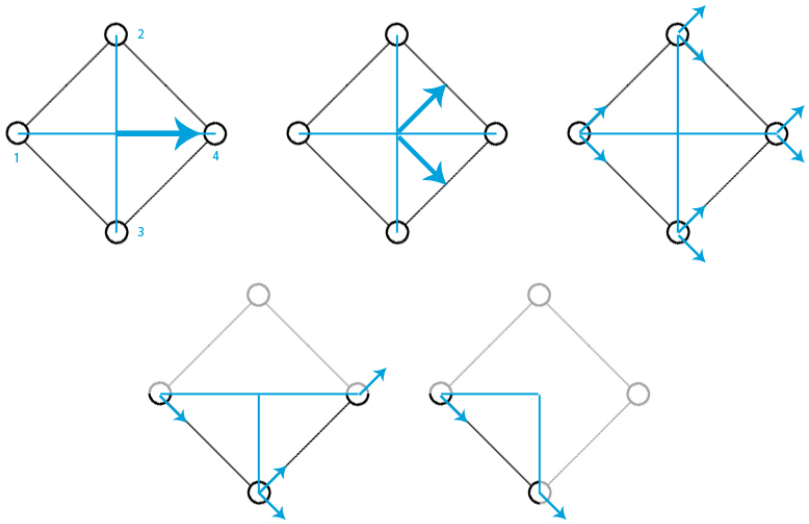

Figure 3. 13 - Steps taken to convert loads in the 3D space frame to single equivalent nodal ones for the 45 degree inflow scenario. From top left to bottom right: 1) Original loading situation, 2) vector components aligned with structure, 3) vector components equally spread over nodes in leg-brace connection, 4) discarding half the system due to symmetry, 5) single situation for analysis of leg-brace load assessment

Since constructing nodal loads for this second case is a bit more challenging, the following example illustrates the procedure for shear force of a certain cross section. The procedure is graphically depicted in steps 1 trough 5 in the figure shown above. A similar procedure, as discussed for the 0-degree inflow angle, is required to address loads as a results from gravitational forces and overturning moments. These are not discussed here.

After the original shear force (1) is broken down into its respective components and aligned with member directions (2), it's equally divided over the four nodes (3). As a result of symmetry, nodes 1 trough 4 experiences an equal shear- or compressive force from horizontal environmental or vertical gravitational forces, respectively. There is an equal loading situation about the symmetry line between nodes 1 and 4 from which is follows that only half of the structure has to be analyzed (4). Finally, the two remaining sides at the bottom of the cross section are split. Each part only houses loads parallel to a plane aligned with the two nodes of that plane (5). A separate load analysis is performed for the front (node 1 and 3) and back (node 3 and 4) plane, one of which is shown at the bottom right of the figure. The complete loading situation is converted to two single 2D plane scenarios. These are now similar to that of the 0 degree inflow plane as shown in Figure 3. 6. The extra subdivision of each node is needed to be able to differentiate between loads experienced by legs and members. Legs experience loads on both sides of the node while braces only experience loads on half such a node part.

After similar steps have been followed to find respective nodal loads induced by the structure weight and moment acting on the plane, external loads are broken down to 2D plane loads (Figure 3. 14). Horizontal and vertical components are found, where subscripts 'a' and 'b' indicate respective side of nodal split.

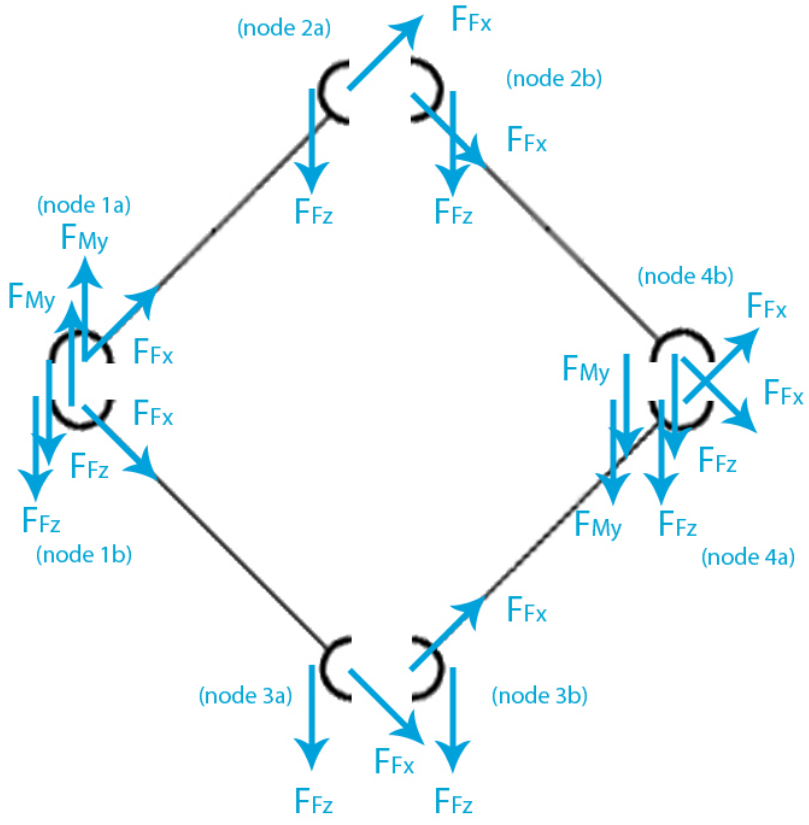

Figure 3. 14 - Nodal load distribution of horizontal cross section for 45-degree inflow case

Equation (3.36) trough (3.43) show derivation of nodal forces in Figure 3.14 from external loads.

$$F_{Fx,1234} = \left.\frac{F_{x45}}{4 \cdot \sqrt{2}}\right|_{morison} \tag{3.36}$$

$$-F_{Fz,1234} = \left.-\frac{F_z}{8}\right|_{gravity} \tag{3.37}$$

$$F_{My,1} = -F_{My,4} = \left.\frac{M_{y45}}{2 \cdot \sqrt{2} \cdot W_{bay}}\right|_{morison} \tag{3.38}$$

$$F_{My,2} = F_{My,3} = 0 \tag{3.39}$$

$$F_{h,1ab2ab3ab4ab} = F_{Fx,1234} \tag{3.40}$$

$$F_{v,1ab} = F_{My,1} - F_{Fz,1234} \tag{3.41}$$

$$F_{v,2ab3ab} = -F_{Fz,1234} \tag{3.42}$$

$$F_{v,4ab} = F_{My,4} - F_{Fz,1234} \tag{3.43}$$

At this point, all external loads are represented in their horizontal and vertical components for each node. Furthermore, by representing the 45-degree inflow case in 0-degree inflow case form, a standardized frame configuration is formed.

Step 4: Internal frame member loads

Using the frame conversions discussed in step three, inflicted member loads are found using two cross-sections per bay (Figure 3. 15). Firstly, the top-cross section is considered. Internal member loads are estimated by balancing external loads with loads aligned in member direction. For each node in the cross-section, internal leg (F_{leg}) and brace (F_{brace}) forces are found by balancing these loads with external horizontal ($F_{external}$) and vertical ($F_{external}$) forces (e.q.:(3.44)). For following notations subscripts 'h' and 'v' indicate respective load direction being horizontal and vertical. Additionally, subscripts 'top' and 'bot' indicate respective location of cross-section. Note that top and bottom counterparts are not necessarily equal for reasons discussed in step two.

$$\begin{bmatrix} cos(\theta_{batter}) & cos(\theta_{brace}) \\ sin(\theta_{batter}) & sin(\theta_{brace}) \end{bmatrix} \cdot \begin{pmatrix} F_{leg} \\ F_{brace} \end{pmatrix} = \begin{pmatrix} F_{external,h,top} \\ F_{external,v,top} \end{pmatrix} \tag{3.44}$$

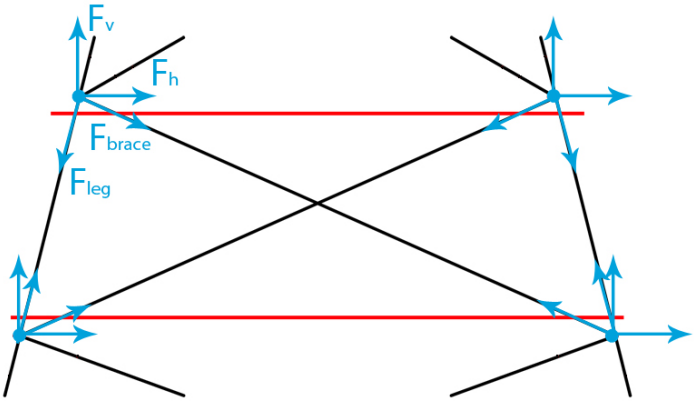

Figure 3. 15 – Member loads obtained using from cross sections

Second, these member loads serve input to estimate load relocation due to coupling of the front and back of a bay. Namely, nodes at the bay front and back of a cross section are exposed to a different load as a result of change in direction of forces caused by the overturning moment. Since braces connect the bay back to the front, the external load at the back of the bay also effectively affects the front of the bay. This relation obviously also holds for loads at the top, they have a similar affect to loads distribution at the back.

To establish the effects of load coupling, new horizontal and vertical load balances are constructed for the bottom bay cross-section. Equations (3.45) and (3.46) show the relations used to find these residual loads ($F_{residual}$) for horizontal and vertical equilibrium as a result of coupling of bay sides.

$$\sum F_{horizontal,bot} = 0 \rightarrow F_{external,h,bot} = F_{leg} \cdot cos(\theta_{batter}) + F_{leg} \cdot cos(\theta_{batter}) + F_{residual,h} \quad (3.45)$$

$$\sum F_{vertical,bot} = 0 \rightarrow F_{external,v,bot} = F_{leg} \cdot sin(\theta_{batter}) + F_{leg} \cdot sin(\theta_{batter}) + F_{residual,v} \quad (3.46)$$

For each node at the bottom cross section, these residual loads serve as an additional load increment for the top cross section of the underlying bay. This way a more accurate load description is achieved rather than by solely balancing external loads with internal member loads at the top cross-section of a bay.

Once member loads are established for each plane (as shown in Figure 3. 12 through Figure 3. 14), loads are combined to reveal total member loading. In an effort to keep a to-the-point model description, only the essence of these combinations is discussed below. In SJOEM, more detailed geometric relations are used.

An additional simplification is to assume that the planes are completely vertical rather than being at a slight angle. Thus, the plane as observed in Figure 3. 15 is assumed to be vertical rather than being at a slight angle, equal to the jacket's batter. In reality a plane is at a slight angle thereby creating a small vector perpendicular to the plane when broken down in its basic components. By assuming these planes are vertical rather than at a slight angle a two-dimensional analysis can be conducted rather than a three-dimensional one since for this instance vertical forces are aligned with the plane.

For clarity reasons this difference is emphasized in Figure 3. 16. Here 'A' shows the two-dimensional plane used to evaluate member loads while 'B' shows the actual case under a slight angle. The blue lines in the image show the difference in plane geometry if this effect would not be taken into account.

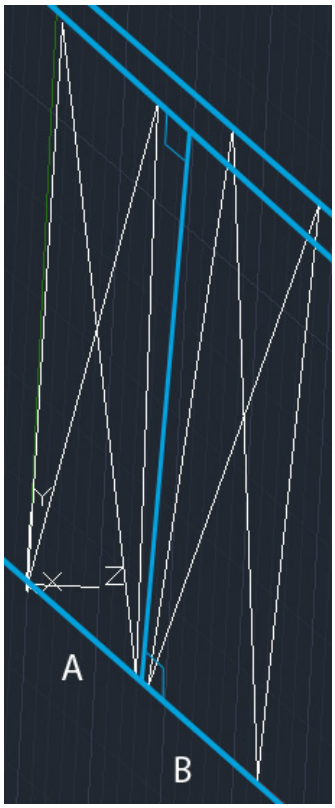

Figure 3. 16 - Taking into account plane alignment

As noted in step two, due to symmetry only a single plane evaluation is required for the 0-degree inflow scenario. When looking back at Figure 3. 12 it's evident that member sides connected to node 1 experience the same load as members connected to node 2. Obviously this relation also holds for nodes 3 and 4. For the 45-degree scenario however, an extra step is required. Split nodes need to be brought together again. Since all loads are in axial direction of a member, total loads are found by simply adding member loads for each plane. Note that leg member loads have to be taken double since they experience loads from the two planes they connect. This is obviously not the case for brace loads, since these are not split over two planes. For example, reverting back to Figure 3. 14, members connected to node 1 experience the following forces. Here subscript 'tot' is used to indicate the total summed load a member is experiencing.

$$F_{tot-leg,h} = 2 \cdot F_{leg,h} \tag{3.47}$$

$$F_{tot-brace,h} = F_{brace,h} \tag{3.48}$$

$$F_{tot-leg,v} = 2 \cdot F_{leg,v} \tag{3.49}$$

$$F_{tot-brace,v} = F_{brace,v} \tag{3.50}$$

At this point, all member loads are known for each of the six loading scenarios. That is, for three load cases and two inflow angles. In order to determine the required member diameter and wall thickness, the largest tensional and compressive load is selected, per bay, from all six loading scenarios. The resulting maximum tensile load is tested for yield while the maximum compressive load is subjected to both a buckling and yield analysis.

Step 5: Wall thickness

Now maximum brace and member loads are known, these are used to determine required wall thicknesses of a diameters selected by the optimization algorythm. For each bay, minimum brace and leg wall thickness is found in a three-phase process. These phases are similar to those used to determine tower cross-section parameters and therefore only briefly discussed.

Firstly, as mentioned at the end of the step four, the largest brace/leg tension and compression forces are selected from all load cases and subjected to a yield test. Using the Brent's theorem (Brent 1973), the minimum required wall thickness (wt) is estimated for given diameter (D) and member load (F_{member}). This optimum is found at the balance between internal member stresses and material yield limit (e.q.(3.51)).

$$\frac{F_{member}}{\frac{\pi}{4} \cdot (D^2 - (D - 2 \cdot wt)^2} = \sigma_{yield} \rightarrow wt \tag{3.51}$$

Second, using the largest compressive leg and brace load, minimum wall thickness to withstand global (Euler) buckling is found using the buckling method as proposed by Vugts (Vugts 2002). Using this simplified global bucking method, occurring stress is compared to a certain Euler buckling stress rather than to the yield stress of the material. The allowable critical buckling stress is a function of member geometry, connection to surroundings and material properties. All members are assumed connected by hinges and exposed to a single axial compressive load. For equal reasons as discussed for the tower, this case again does not fully describe the actual loading satiation. However since this method is widely accepted in the engineering community, it's also used here.

Global buckling is however not the only failure mode. Local buckling needs to be addressed as well. In contrast to the tower's local buckling analysis, this time buckling theory according to GL (GLrenewables 2012) is used. This method is preferred since for this analysis the effects of hydrostatic pressure on buckling are taken into account as well.

From each of the failure mode (yield, global- and local buckling) the maximum wall thickness is selected for given input diameter. Finally using diameter and wall thickness, the cross sectional area is found. This area is forwarded back to the basin hopping function minimizer up until the diameter and wall thickness combination is found that results in a minimal cross sectional member area.

At this point however, structure weight is still a function of the initial rule of thumb wall thickness since the actual required wall thickness was not yet known. There is therefore still a margin of error in the estimated gravitational loading and the new gravitational load estimated using the actual wall thickness. Therefore the newly found 'real' wall thickness is replaced with the old one and the load estimation is repeated from the point where the jacket's weight is determined. This loop includes the whole procedure for determining environmental loads since the new optimum area could have a different diameter. The loop continues to re-iterate member geometry up until the difference in resulting optimal cross-sectional area differs less than one percent from the old one.

Step 6: Sleeves

Internal frame member loads addressed during the previous steps only represent average member load. Stress concentrations occur when stresses 'flow' from one member to another as a result of changes in member geometry. These increased stresses have a large impact on failure modes and can even cause a member to punch a hole in another (punching). In an effort to prevent failure as a result of these loading modes, protective sleeves are placed either outside or inside member connections. Thereby locally increasing wall thickness, reducing material stresses.

For SJOEM, the amount of additionally required material is estimated as follows; Firstly, a stress concentration factor (SCF) is determined as a function of joint geometry using Efthymiou equations for an axially loaded K-brace according to API standards (API 2000). SCFs are determined at each horizontal cross section that was previously used to determine internal member loads. This results in four SCFs per bay; two at the top (one for the leg and one for the brace) and two at the bottom. Second, for each bay top and bottom, largest leg and brace loads are selected among load cases and inflow angles. These loads are multiplied with their respective SCFs to find-out stress concentrations. Using these increased stresses, a new yield check is performed, resulting in a larger required wall thickness. Sleeve thickness is simply found by taking the difference between the original and new wall thickness. Furthermore, sleeve length is taken as 5 percent of total member length. Finally, increased wall thickness is assumed added internally, thereby not affecting wave loads.

Step 7: Repeat

As extensively discussed during paragraph 3.5.4 Optimization sequence, wall thicknesses found for its accompanying diameter are used to estimate minimal area required to withstand all DLCs. This optimization process continues until the minimum diameter and wall thickness configuration for each bay's legs and braces is found. When this is the case, the data resulting from this structure configuration is collected for the following design phase, this can either be the underlying bay or the foundation pile design.

Step 8: Data collection for pile analysis

For each DLC per inflow scenario loads are expressed in its three basic components; base shear (F_b), overturning moment (M_o) and gravity (F_g). Base shear is the sum of all horizontal external loads on the structure; this includes horizontal RNA, tower and jacket loads. Overturning moment is the sum of moments induced by these vertical loads plus additional moments caused by misalignment of the RNA enter of mass with the tower center axis. Obviously the gravitational component is the sum of all vertical loads caused by structure's weight above the mudline.

In addition to these three mudline load components, the distance between piles has a huge impact on pile loading situation. For the current model however, pile distance is determined as a function of the (constant) leg batter. The further piles are placed apart the better the structure's geometry helps resist loads. Quite possible, a structure cost reduction can still be achieved if leg better where treated as a variable rather than a constant.

3.6 Foundation piles

3.6.1 Design procedure

The foundation pile assessment marks the final phase of the engineering model. Optimal pile volume is found as a function of (mudline) base shear (F_b), overturning moment (M_o), gravitational load (F_g) and pile distance (W_{piles}). These three-mudline load components where are found by combining horizontal or vertical loads as a result of environmental interactions or structure weight respectively. The spatial distribution of foundation piles is found using elevation heights and (constant) rule of thumb leg batter.

For the current engineering model, foundation piles are assumed vertically driven rather than inclined, which is common practice for offshore wind jacket structures. However, inclined piles would endure lower pile loads because these effectively have a wider base. Inclined piles are however currently not the preferred in this field of engineering. Equipping a jacket with inclined piles requires the piles to be driven trough the jacket's legs, thereby drastically changing its design.

Analogue to the procedure depicted in Figure 3. 17, pile optimization is conducted as follows; firstly pile top loading is estimated using basic equilibrium relations. Note that top loads are not part of an optimization loop since these are assumed constant rather than being a function of pile geometry. Pile dimensions are found solely from internal loads and soil interactions. An iterative process is used to address pile geometry by finding accompanying pile wall thickness and length for diameters picked by the optimization algorithm. For such a diameter, wall thickness is determined using two criteria; firstly a yield check is performed and second a minimal diameter over wall thickness ratio is used to take into account buckling during pile driving. Finally, required pile length (L) is determined by balancing axial and lateral soil resistance with pile top loads. Obviously, as is true for all optimization sequences in this engineering model, the optimal pile geometry is found for the lowest volume that passes all design criteria.

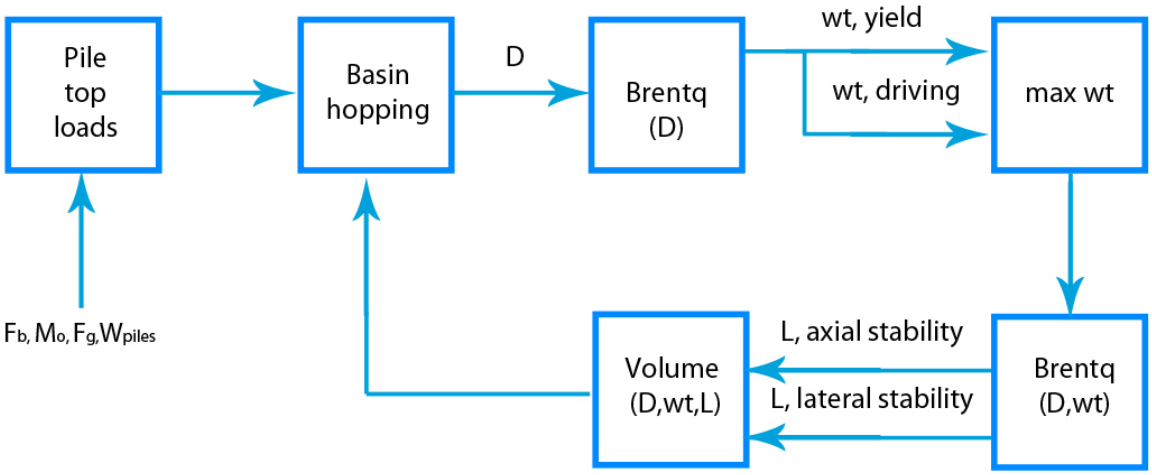

Figure 3. 17 - Pile design optimization loop

3.6.2 Pile top loading

Pile top loads serve as the baseline to determine internal pile loads. At this point however, some basic understanding of foundation design is required to gain better insight in subsoil load interaction. Firstly, symmetry axes are established to simplify pile design. These are a result of two vertical symmetry planes around the center axis of the structure; one parallel and one perpendicular to wind/wave direction. Figure 3. 18 shows these symmetry planes for a vertical cross section about the mudline.

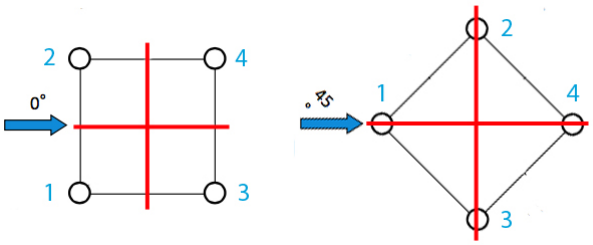

Figure 3. 18 – Top view of symmetry planes (red) at mudline for two inflow scenarios

From symmetry relations it follows that pile top forces, resulting from the gravitational load and base shear, are equally divided over each pile (e.q.: (3.52) and (3.53)). Subscript 't' and 'a' indicate loading direction being either transversal or axial with respect to the pile's local coordinate system. Additionally, subscript 'Fb' and 'Fg' (and 'Mo' and 'Mt' later in this paragraph) indicate load origin. Numbers indicate at what pile top these loads are present. Load *relations* shown above are equal for both inflow scenarios. Obviously, base shear (F_b) load intensity does still differ per inflow angle and load case.

$$F_{t-Fb,1234} = \frac{F_b}{4} \tag{3.52}$$

$$F_{a-Fg,1234} = \frac{F_g}{4} \tag{3.53}$$

There is however an additional phenomena that affect axial and transversal pile load distribution. As discussed in the previous paragraph, when member loads where estimated at the bottom cross-section of a bay, a different set of member loads where found. This turned out to be caused by difference in reaction loads. For each bay, this effect is taken into account by balancing internal member loads found at the top cross section with external loads at the bottom cross section. The resulting load difference was then taken into account as an effective additional external residual load.

Now obviously this effect is taken into account for pile loads as well. Therefore, for each pile, an extra term is added. This term takes into account the above-discussed difference in load distribution from reaction loads. Note that this residual load term differs between the front and back of a bay since nodal loads are different.

$$F_{t,1234} = F_{t-Fb,1234} + F_{t,residue} \tag{3.54}$$

$$F_{a,1234} = F_{a-Fg,1234} + F_{a,residue} \tag{3.55}$$

Analogue to overturning moments about the vertical cross sections of jacket bays, piles are exposed to an equal but opposite axial load as a result from overturning moment. The following local axial pile loading relations are found, where subscripts 0 and 45 indicate respective inflow origins:

$$F_{a-Mo0,12} = -F_{a-Mo0,34} = \frac{M_{o0}}{2 \cdot W_{piles}} \tag{3.56}$$

$$F_{a-Mo45,1} = -F_{a-Mo45,4} = \frac{M_{o45}}{2 \cdot \sqrt{2} \cdot W_{piles}} \tag{3.57}$$

$$F_{a-Mo45,23} = 0 \tag{3.58}$$

Subscripts Mo0 and Mo45 indicate whether overturning moments apply to the respective 0- or 45-degree inflow case.

At this point however, equilibrium conditions still have not been fulfilled. Namely, transversal loads acting on the pile top induce a moment as well. To determine this transversal moment (M_t), its respective lever arm needs to be known. This raises a problem since the connection between foundation piles and the soil is far from perfect. It's dependent on the loading situation, pile geometry and soil properties. A simplified approach is needed to model the connection and determine lever length.

According to Vugts (Vugts 2002), the effective lever arm length used to establish moments caused by transversal pile top loading is corresponding to the distance from mudline to the first point where internal pile moment is zero. This is the so-called inflection depth (d_e). However, this still does not help since the transversal moment is the parameter that's looked for in the first place. Vugts states however that the inflection point is located at a depth of roughly three times the pile diameter. Thus, in order to determine the moment induced by transversal pile loads, the pile diameter needs to be known. The following relation is used to determine the external moment at the pile's top:

$$M_{t,1234} = F_{t,1234} \cdot d_e \tag{3.59}$$

Since both the transversal moment as inflection depth are unknown their respective value is iteratively determined starting with an initial guess pile diameter of one meter. Then, using the moment resulting from the initial guess diameter, optimal pile dimensions are found using the analogy shown in Figure 3. 17. Using the diameter resulting from the optimization, a new pile top moment is calculated. And so forth. This iterative process continues up until the resulting pile volume change is less than one percent. At this point the inflection point depth is established from its own induced transversal moment.

Finally, to achieve equilibrium, each pile's neighboring pile experiences an axial load as a result of this transversal moment discussed above. For the zero-degree situation the following relation is found:

$$F_{a-Mt0,12} = -F_{a-Mt0,34} = \frac{2 \cdot M_{t0,1234}}{W_{piles}} \tag{3.60}$$

For the 45-degree angle piles 2 and 4 experience no additional axial load since top moments on pile 1 and 4 balance each other out. Piles 1 and 4 however do experience an additional axial load as a result of this phenomenon:

$$F_{a-Mt45,1} = -F_{a-Mt45,4} = \frac{4 \cdot M_{t45,1234}}{\sqrt{2} \cdot W_{piles}} \tag{3.61}$$

Now, taking into account all of the above, the following pile top loads are found. All loads are taken absolute, plus and minus signs indicate loads being tensile or compressive respectively.

For the 0-degree inflow angle the following pile top loads are found, where all variables are taken absolute in an effort to emphasize loading directionality:

$$F_{t0,1234} = F_{t,1234} \tag{3.62}$$

$$F_{a0,12} = -F_{a-Fg,12} + F_{a-Mo0,12} + F_{a-Mt0,12} \tag{3.63}$$

$$F_{a0,34} = -F_{a-Fg,34} - F_{a-Mo0,34} - F_{a-Mt0,34} \tag{3.64}$$

$$M_{0,1234} = M_{t,1234} \tag{3.65}$$

Using the same methodology, the following relations for the 45-degree scenario are found:

$$F_{t45,1234} = F_{t,1234} \tag{3.66}$$

$$F_{a45,1} = -F_{a-Fg,1} + F_{a-Mo45,1} + F_{a-Mt45,1} \tag{3.67}$$

$$F_{a45,23} = -F_{a-Fg,23} \tag{3.68}$$

$$F_{a45,4} = -F_{a-Fg,4} - F_{a-Mo45,4} - F_{a-Mt45,4} \tag{3.69}$$

$$M_{45,1234} = M_{t,1234} \tag{3.70}$$

By reviewing pile top loads in equation (3.62) trough (3.70), a similar load distribution as for jacket legs are found. Inspecting these equations shows that the largest portion of forces and moments is converted to axial loads due to spatial distribution. This confirms with observations from the jacket structure. Additionally, piles located at the largest distance from line perpendicular to the flow (Figure 3. 18) experience an equal opposite load.

3.6.3 Optimal pile volume

Once top loads for each pile per load case and inflow angle are established, optimal pile volume is found in a two-stage process. For each pile, six distinct loading situations are created, resulting in 24 load scenarios.

For any diameter, firstly required wall thickness to pass each load scenario is determined from a yield- and buckling failure analysis. The yield analysis is analogue to those conducted for the tower and jacket. Axial (F_z), transversal (F_x) and bending moment (M_y) are balanced with internal material resistance (A and I_y) and yield limit (σ_{yield}) (e.q.:(3.1)). Second, a simple diameter over wall thickness relation (e.q.:(3.71)) as proposed by API (API 2007) is used to establish a minimal wall thickness such to prevent buckling when piles are driven.

$$wt_{pile}[m] = 0{,}00634 + \frac{D_{pile}}{100} \tag{3.71}$$

Evidently, as is true for all these analyses, the largest wall thickness among resulting minimal wall thicknesses is picked for diameter forwarded by the optimizer.

For the second phase, diameter and wall thickness combinations serve as input for axial and lateral stability checks to determine the required pile length. Firstly, a minimal length is determined such that it provides enough lateral soil resistance to withstand top loads. Analogue to TeamPlay, lateral soil resistance is found using Blum's method. In this method a critical pile depth is established for walls clamped in the soil (Verruijt (Verruijt 1999)). Second, axial pile resistance is determined in an equal manner to TeamPlay as well. Here the pile's axial stability is addressed by determining shaft friction for cohesionless soil. The total induced shaft friction is determined from the pile's outer contact area with soil plus either axial resistance resulting from the inner pile contact area in contact with the soil or its end-bearing resistance, whichever is the lowest. The largest among minimal required pile lengths is picked from the axial and lateral resistance and combined with respective diameter and wall thickness. This results a specific pile volume for a chosen input diameter. These optimization steps continue until the lowest pile volume is found that fulfills all loading scenarios.

3.6.4 Conclusion

By following the design procedure as discussed in this chapter optimal structure geometry is found. Used theory should however put to practice before statements can be made on SJOEM's accuracy. This is the main topic of the next chapter. Here results for three sample points are tested against those of FEM software.

4

Results and validation

4.1 Introduction

In the previous chapter the methodology used to establish SJOEM was discussed. For the current chapter, the model is put to practice. Firstly, three case studies are formed using data from possible wind farm locations across the North Sea. Second, jacket output is compared against similar models built using finite element engineering software ANSYS. A comparison is made with two different models. In the first one, internal loads as found by the engineering model are compared to a more basic ANSYS model. For this comparison the main focus revolves around checking whether member load distribution as discussed in step three and four of paragraph 3.5.3 is valid. Since the simplification of the three dimensional model to two dimensions involves a lot of geometric relations this design step is prone for errors. In order to achieve a clear comparison, the same set of simplifications as for the engineering model is applied. These include, all members being connected using hinges plus having loads only act on member ends. For the second case, results from the first model are compared to one that complies more with practice. Here member connections are taken as rigid, thereby allowing non-axial member loads. Thirdly, case study results are discussed. This output ranges from structure geometry through description of external and internal load distribution. Finally, findings for both analyses are discussed, resulting in a list of advantages and limitations of the engineering model.

4.2 Sample points

Validity of the engineering model is checked by comparison of SJOEM to ANSYS using three sample points across the North Sea (Figure 4. 1). For the first and second sample case, site properties are adopted from existing wind farm locations. These represent the Princess Amalia (1) and Alpha Ventus (2) farm. The third farm however, represents an extreme far-shore scenario of the non-existing farm dubbed 'SJOEMF' for Simple Jacket Optimization Engineering Model Farm (3).

Case 1: Princess Amalia

This farm, named after the Dutch king's firstborn child, is located 23 kilometer from the Dutch coastline and is visible from shore when standing at the beach near Amsterdam. The farm occupies a total area of 14 square kilometer and is equipped with 60 Vestas V-80 turbines of 2 MW. Since the farm is so close to shore, it has an average water depth of only 20 meters. Another advantage of placing these structures so close to shore is that this patch of sea is quite tranquil. The Princes Amalia farm is therefore the representative of a farm exposed to mild environmental conditions. Jackets designed for this location should have a geometry resulting in the lowest weight among the three cases.

Case 2: Alpha Ventus

Germany's first offshore wind farm 'Alpha Ventus' is situated just over the Dutch-German coastal border near the island of Borkum. This large-scale offshore wind research facility is the result of cooperation of a large group of institutions and corporations. The large distance from shore (45 km) marks much rougher environmental conditions, both in terms of wind and wave activity. The farm is equipped with REPower 5M (5 MW) turbines, allowing much higher energy yields as for Princes Amalia. Due to the larger depth this structures are equipped with a jacked rather than a monopile. As a result of the relatively rough environmental conditions and large turbine, Alpha Ventus is chosen as medium intensity test case.

Case 3: SJOEMF

In an effort to show the engineering model's versatility, the thirdly chosen sight marks an extreme far-shore scenario. Located 250 kilometers from shore, the farthest patch of Dutch territorial waters is characterized by extreme weather conditions and a depth of approximately 50 meters. In order to gain the maximum power output, this imaginary sight is equipped with Siemen's 6-megawatt SWT6 turbine. Obviously this third case is the most violent one and will most likely result in a structure whose weight is the largest of the three.

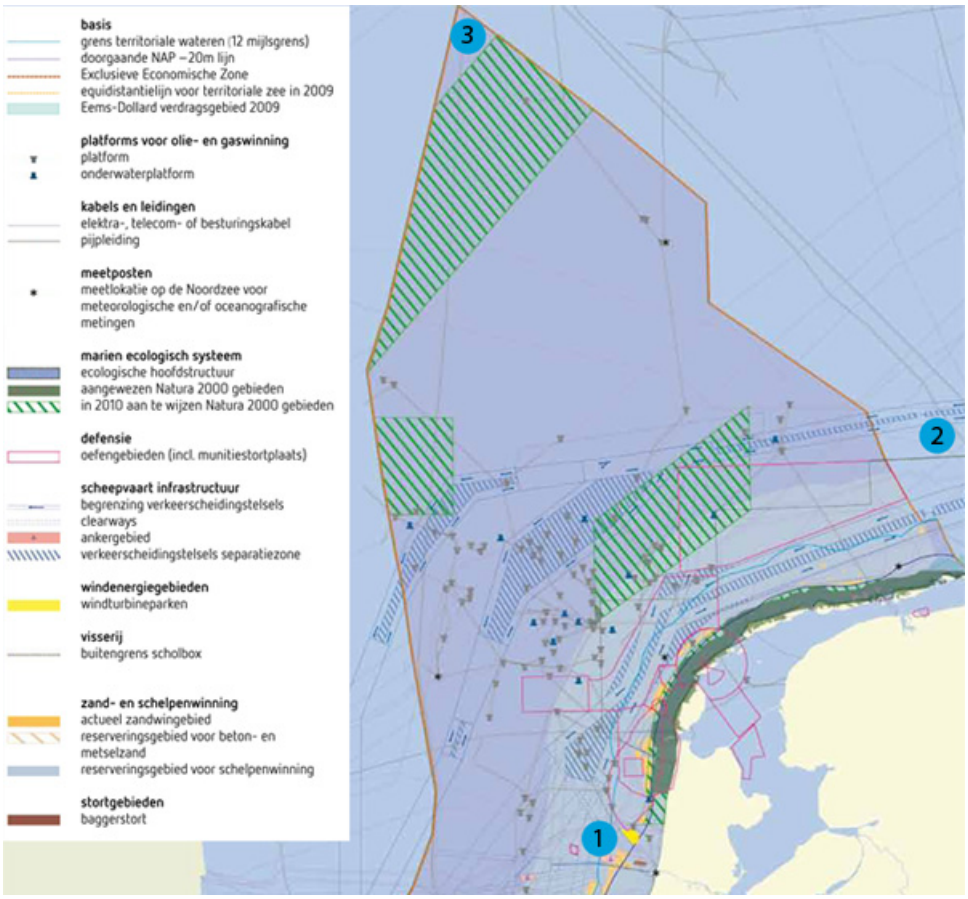

Figure 4. 1 - Test sample points (Source: Noordzeeloket)

From the above-discussed sites, the following data is extracted and used as input for the engineering model (Table 4. 1). These input parameters where introduced at the beginning of chapter three. For the first column the type of input parameter is given. The three middle columns show the value for this parameter for each of the sample points. Thirdly, the right column shows respective map number of appendix A that is used to gather data.

Data from the first four rows is taken from datasheets of the chosen turbine as discussed in each case introduction. Since no data could be found for the wind shear exponent (α) an educated guess is made. One-year significant wave height is found by linear approximation of 50-year significant wave height using relations extracted from the Dutch Offshore Wind Energy Project (DOWEC) (Bierbooms 2002). Soil friction angle (θ_{soil}) and density (ρ_{soil}) are determined from soil type using simplified relations obtained from the Geotech soil properties database (Geotechdata 2015). Note that data merely serves as approximation of average properties. It should not be used for any other purpose outside of this thesis.

Symbol	Test case			Chart number Appendix A
	Princes Amalia	Alpha Ventus	SJOEMF	
D_{rotor} (m)	80	126	154	n.a.
M_{rna} (kg)	1.29E+05	4.40E+04	3.60E+05	n.a.
$C_{d\text{-}rotor}$ (-)	0.4	0.4	0.4	n.a.
V_{rated} (m/s)	14	13	12	n.a.
W_{scale} (m/s)	10	10.5	11	1
W_{shape} (-)	2.1	2.4	2.3	1
H_{ref} (m)	90	90	90	1
α (-)	0.1	0.07	0.05	n.a.
H_{depth} (m)	22	30	50	2
HAT (m)	1.5	2	1	3
H_{surge} (m)	3	2.25	2	4
H_1 (m)	2.6	3.44	4.3	5
H_{50} (m)	4.8	6.4	8	5
ρ_{water} (kg/m^3)	1025	1025	1025	n.a.
θ_{soil} (deg)	35	40	25	6
ρ_{soil} (kg/m^3)	1.90E+04	2.10E+04	1.80E+04	6
σ_{yield} (N/m^2)	2.50E+08	2.50E+08	2.50E+08	n.a.
E_d (N/m^2)	2.10E+12	2.10E+12	2.10E+12	n.a.

Table 4. 1 - Sample point data

4.3 Model validation

Since the core task of this thesis is the design of a jacket structure, only space frame loads are evaluated. Thus RNA, Tower and pile analysis are checks are not checked for correctness. SJOEM's output is evaluated for two cases. Firstly, internal member forces are compared to an ANSYS FEM model built from truss elements. The truss model is built in such a way that the same set of assumptions as in SJOEM is maintained, one of which being that member connections are modeled as hinges, allowing free rotation. Focus revolves around whether mathematical relations of step three and four (paragraph 3.5.3) are implemented correctly and if accuracy losses resulting from modeling the 3D structure as beings 2D are acceptable. Emphasis is put on these design steps since these are most susceptible to errors due to usage of extensive geometric relations. Second, the truss model is compared to one that complies more to how a jacket structure would be constructed in reality. For this model, beam elements are used rather than trusses. The advantage of beam elements over trusses is that beams are able to transfer non-axial loads and member connections can be modeled as rigid. By checking the differences between the truss and beam structure first insight is gained in one of the core simplifications. Namely, the assumption that a real world jacket structure with rigid member connections can be modeled as one where members are connected by joints. Comparing SJOEM to these ANSYS models does however still not consider all simplifications. One of which, for example, is estimation of hydrodynamic loads on a single diameter equivalent monopile rather than from the members in a bay. This and other simplifications are discussed at the end of the paragraph.

4.3.1 Nodal loads

Since member loads in FEM models are not evaluated using the cross-sectional method introduced in chapter three a different load description is needed. For each bay, forces acting on nodes at the top of the bay are found using step one and two of paragraph 3.5.3. Then, these external loads are spread over the four nodes of a cross section. This way rather than balancing member loads with the accumulated external loads for a cross section and completely neglecting everything above, the structure is considered as a whole. Meaning member loads for some bay i are found from combination of external loads only acting on that bay plus internal member loads of everything above.

This procedure is further clarified using Figure 4. 2. This image shows, from left to right, external environmental forces at nodal height (1), a jacket structure (2), un-accumulated horizontal external loads (3), horizontal force load distribution on jacket (F_b) (4) and overturning moment distribution resulting from horizontal loads (M_{oe}) (5). Vertical load distribution due to structure weight is not shown here but has a similar form as horizontal force distribution. This is extensively discussed in chapter 3.

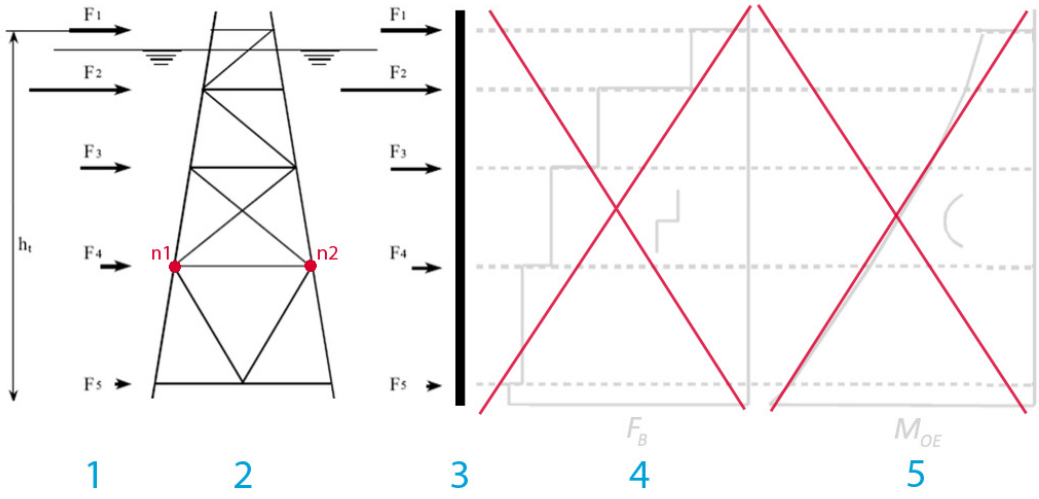

Figure 4. 2 - Ansys nodal loads creation from environmental loads

To obtain the load distribution for the ANSYS model only one to three are used rather than going trough one to five for SJOEM. External loads found under (3) are now divided over each of the four using similar relations as for the engineering model only this time without any frame conversion steps as used in step three of paragraph 3.5.3. Thus for a certain cross section i at nodal height the following expressions are found for front (n1) and back (n2) nodes of the zero degree inflow angle. Subscripts 'Fx' and 'Fz' indicate load being from horizontal force (Morison) or vertical force (weight), respectively. Finally, 'H_{bay}' and 'W_{bay}' are used for bay height and width.

$$F_{n1,horizontal,i} = F_{n2,horizontal,i} = \frac{F_{x,i}}{4} \tag{4.1}$$

$$F_{n1,vertical,i} = -\frac{F_{z,i}}{4} + \frac{\left(\sum_{k=1}^{i-1} F_{x,k}\right) \cdot H_{bay}}{2 \cdot W_{bay}} \tag{4.2}$$

$$F_{n2,vertical,i} = -\frac{F_{z,i}}{4} - \frac{\left(\sum_{k=1}^{i-1} F_{x,k}\right) \cdot H_{bay}}{2 \cdot W_{bay}} \tag{4.3}$$

For the 45-degree inflow angle nodal loads are found using similar procedures. Here nodes located about the center of the structure are however not exposed to any bending moments. Furthermore, for obvious reasons, vertical forces resulting from the overturning moment of a bay are divided by the square root of two times bay width rather than by two times the bay width.

4.3.2 Ansys truss model

To achieve a similar structure as the one used for SJOEM, the FEM model is build using ANSYS's 'link180' components. Link180 members are three-dimensional truss elements. Trusses can only transfer axial loads as a result of they way they're loaded and connected to the outside world. Namely, trusses can only be loaded at their edges and are connected to the outside world using joints. Since these two properties are the core assumptions of the engineering model, trusses are obviously the best choice to evaluate SJOEM's output of step three and four to FEM results.

The truss model is compared to SJOEM by means of internal member loads. Since for both models members are only axially loaded and members have the same cross-sectional area, comparing internal member loads would yield the same results as when comparing member stresses. No buckling check is performed since buckling engineering models as described by the used standards differ greatly from buckling theory used in FEM software. Therefore, large differences in buckling loads could be observed solely as a result of using different models. Additionally, since stress concentrations can only form in rigid member connections, these cannot be evaluated for the current model.

Figure 4. 3 to Figure 4. 5 show member loads for the princess Amalia farm for DLC 1 to 3 respectively. In each of these images, the 0-degree inflow is depicted on the left hand side while the 45-degree inflow scenario is depicted on the right. Here compressive loads are indicated with a negative sign and blue flag, tensile loads are shown with a positive number and red color. For each of the images symmetry is observed in equal form to that of the engineering model. Furthermore, comparison of truss model loads of these figures to member loads of SJOEM reveals a similar form of load distribution over the structure. Appendix B1 to B9 show larger plots of the struck model for each sample points. Furthermore, Appendix B35 to B43 depict jacket member loads from SJOEM output, these images will be discussed extensively in paragraph 4.3.

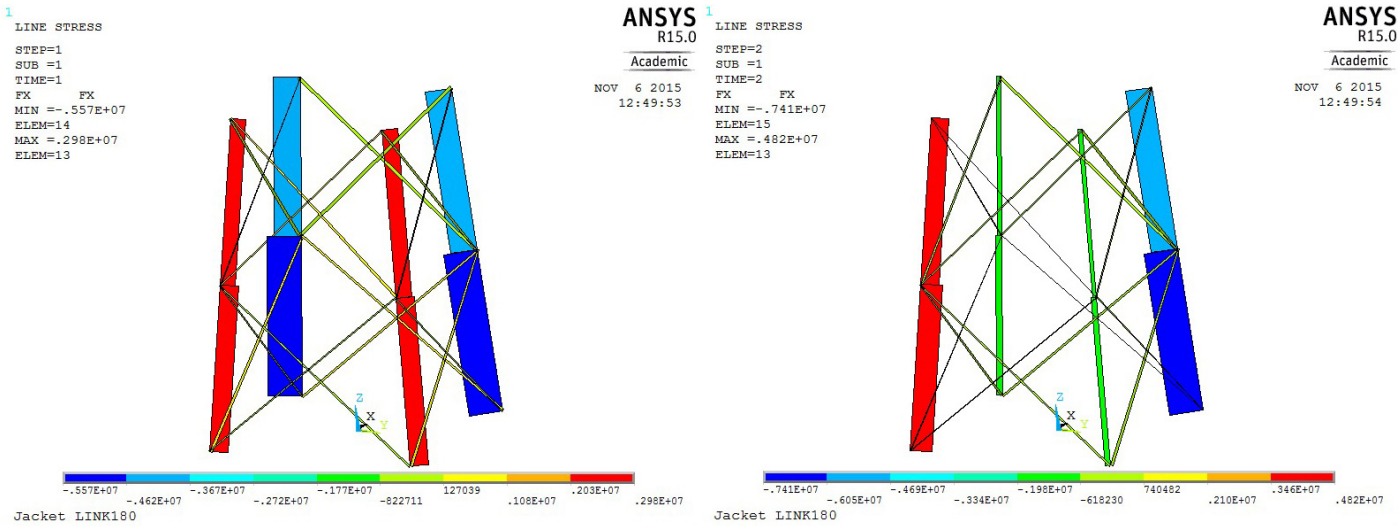

Figure 4. 3 - Ansys member force distribution for DLC 1 for 0-degree inflow angle (left) and 45-degree inflow angle (right)

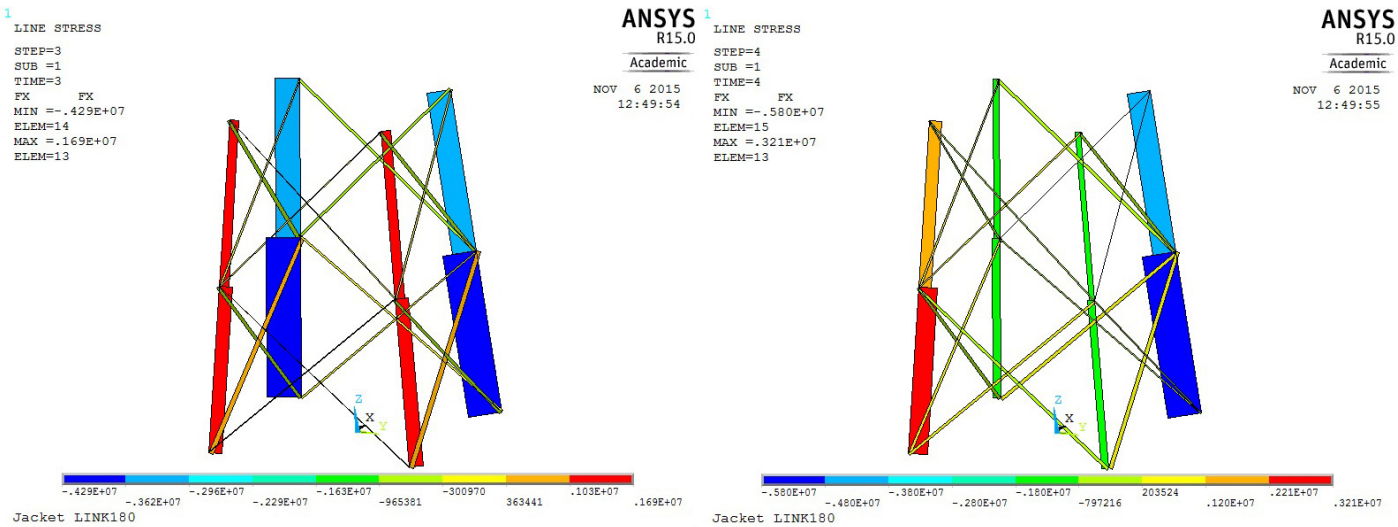

Figure 4. 4 - Ansys member force distribution for DLC 2 for 0-degree inflow angle (left) and 45-degree inflow angle (right)

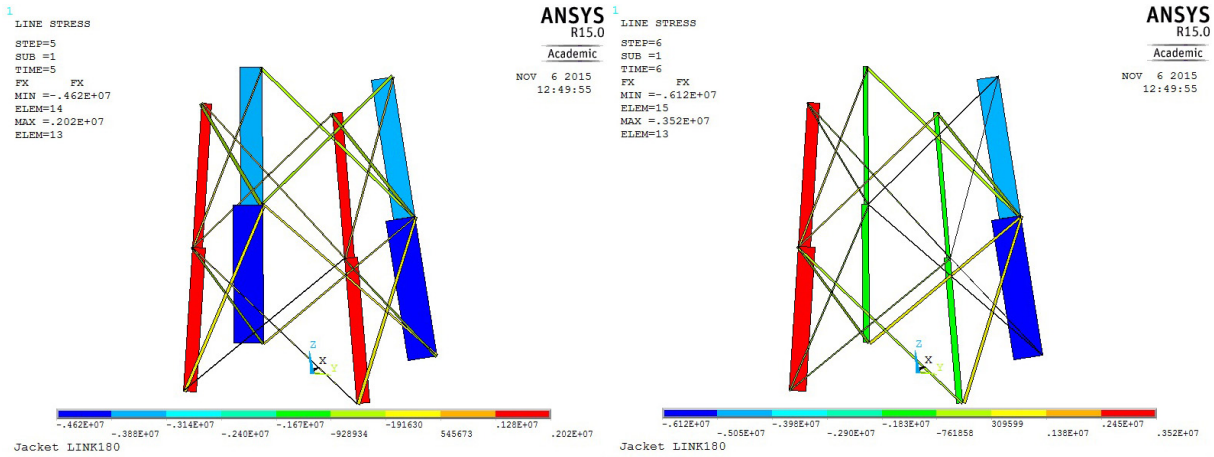

Figure 4. 5 - Ansys member force distribution for DLC 3 for 0-degree inflow angle (left) and 45-degree inflow angle (right)

Obviously, these images only serve as a general indication of member load distribution. A more accurate insight is achieved when numerical member loads are compared. Table 4. 2 shows maximum compressive and tensile loads for SJOEM and the ANSYS truss model per bay for legs and braces per bay. The third column shows for which DLC this design driving load occurs. Locations of the members where these loads occur are best explained using Figure 4. 6 where anticipated inflow jacket planes are depicted with respect to flow direction (blue arrow). The 'Angle' column shows at which of the three general locations the member is located; 0-degree plane, 45-degree plane left part or 45-degree plane right part. Furthermore, the 'Side' column shows whether the member is located on either the left (red) or right (green) side of the plane. For example, the first load maximum is found in the right side of the right part of the 45-degree inflow plane at bay one. This member is pointed out in Figure 4. 6 using the blue target sign. Looking back at Table 4. 2, there are three remaining columns on the right. Here the first two columns give maximum member loads for SOME and the ANSYS truss model respectively. For the outermost right column the difference between these values is compared.

Bay	Member	Location			Load			
		Load case	Angle	Side	Direction	SJOEM (N)	Ansys (N)	Diff (%)
1	Leg	1	45 Right	Right	Compressive	6.25E+06	5.84E+06	6.93
1	Leg	1	45 Left	Left	Tensile	4.24E+06	3.98E+06	6.53
1	Brace	1	45 Right	Right	Compressive	5.52E+05	5.52E+05	0.15
1	Brace	1	45 Left	Left	Tensile	3.32E+05	3.32E+05	0.15
2	Leg	1	45 Right	Right	Compressive	8.19E+06	7.41E+06	10.53
2	Leg	1	45 Left	Left	Tensile	5.31E+06	4.82E+06	10.18
2	Brace	2	45 Left	Left	Compressive	5.62E+05	4.68E+05	20.02
2	Brace	2	45 Right	Right	Tensile	7.19E+05	6.26E+05	14.90
							Average error	8.60

Table 4. 2 - Maximal load comparison of Ansys and Engineering model for Princes Amalia farm

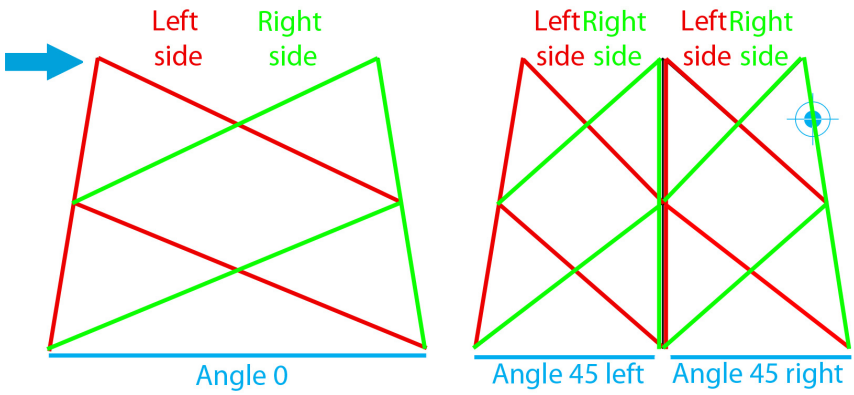

Figure 4. 6 - Member location

When ANSYS and SJOEM member loads are inspected, maximum loads are found at the same locations. This observation is true for all sample points. The size of maximal loads does however differ when ANSYS results are compared to the engineering model. An increase in error is observed for each new bay as the observer moves towards the bottom bay. This increasing fault is the result of error accumulation. Each bay has a certain error, but since loads for each bay are found as a function of loads of the previous bay, the error in load distribution is added to the new bay. The source of these errors is traced back to simplification in angular notations. Namely, external loads on each node are assumed aligned with the bay plane while these are actually at a small angle, equal to the batter angle. For clarity reasons this effect is depicted in Figure 4. 7 for an arbitrary bay exposed to a vertical load. The left hand side of the image shows an over exaggerated version of the simplification in three dimensions. Solid lines show the bay configuration as found in practice while dashed lines shows frame as how it's assumed in SJOEM. When inspecting the right side of the image one finds that for the SJOEM simplification member loads can easily be found from the load since this load is aligned with the plane. This is however not the case for the jacket in practice. When this vector is broken down in components aligned with the frame one of these components is perpendicular to it. Since trusses can only experience axial loads it follows that this remaining load vector is not experienced by the plane but rather by the (transparent) braces next to it. Thus by assuming that bay planes are vertical (the dashed plane) these planed become aligned with vertical (and horizontal) loads allowing for a two-dimensional analysis. This is however at the cost of a certain loss of accuracy, the plane alignment does not fully describe practice anymore. This seemingly straightforward effect is currently not taken into account for this simplification was not anticipated to have such an impact on accuracy of results. Most likely this loss of accuracy can be avoided by transforming external loads in such a way that they align with the frame in practice rather than to transform the plane such that they align with loads. Namely, by simply taking the plane as vertical a slightly changed geometry is found. This can also be seen when inspecting Figure 4. 7.

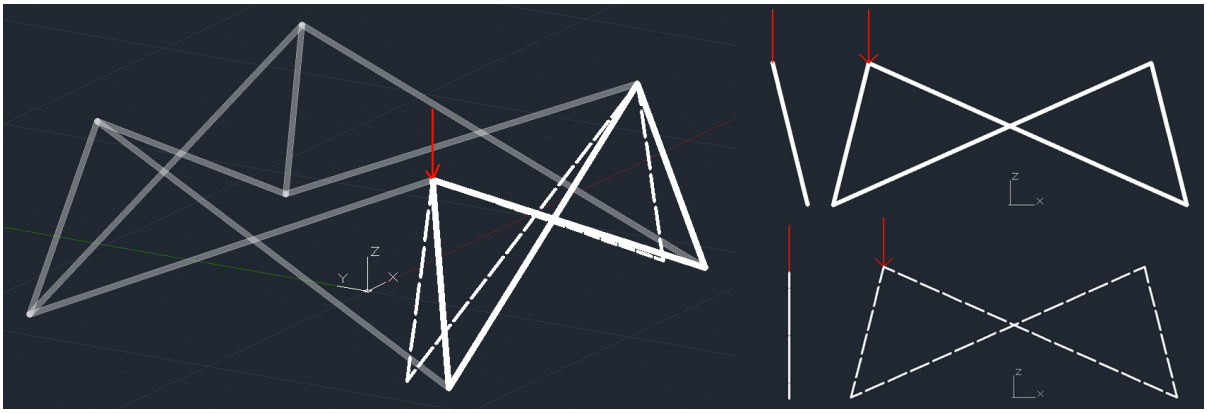

Figure 4. 7 - Simplification of load angle

Since the three-dimensional jacket is modeled as a two-dimensional plane system (Figure 3.6), the load vector perpendicular to the plane is neglected. This vector, which was thought to only have a small effect on member loads, actually proved to have a quite large effect on the load distribution. Fortunately, the inaccurate load distribution as a result of the two-dimensional system only results into a more conservative design. Maximum member loads as estimated by the engineering model are always larger than those found using the Ansys analysis. This result is also observed when comparing maximum member loads in Table 4. 2.

Finally, Appendix B54 and B55 show respective maximum load comparison of Alpha Ventus and SJOEM farm respectively. For these sample points the same phenomenon as discussed above is found with a similar magnitude. Therefore these are not discussed further.

To summarize, estimation of member loads from a 2D idealized member system results in a substantial loss of model accuracy compared to the three-dimensional model in ANSYS. This is the result of taking small angles as zero and taking bay planes as vertical while actually being at a slight angle. Due to accumulation of errors, an increasing accuracy loss is found for each newly additional bay. However, since this error results in a more conservative design, the resulting geometry is still valid for application.

4.3.3 Ansys beam model

In an effort to find out the error as a result of assuming all members are connected using joints, a second model in Ansys is built where member connections are taken as rigid. By using rigid connections members are exposed to non-axial loads in addition to solely axial loading, which is the case for the truss model. Rigid member connections confirm more to the jacket than it would be constructed in practice, members are welded together rather than being connected using hinges or ball joints.

The jacket is modeled using ANSYS's 'beam188' elements. These 3D linear finite strain members are connected to surroundings by two nodes and have six degrees of freedom per node. As a result, the beam188 element can be subjected to shear and torsional stresses in addition to pure tensile or compressive stresses. For the current analysis, only yield stresses are evaluated. Buckling and stress concentrations are not considered for similar reasons as for the truss model.

A comparison is made between; pure axial stresses for the truss model, pure axial (line) stress for the beam model and the von Mises yield criterion. Findings are shown per DLC in Figure 4. 8 to Figure 4. 10 for the Princes Amalia farm. In each image three stress cases are depicted. From top to bottom these are; pure axial stress for truss system, axial stress for beam system and von Mises stress for beam system. The von Mises criterion is used rather than summation since the directionality of internal member stresses has an effect on the amount of strain the material can withstand. Furthermore, at this point it has become evident that largest internal stresses occur at the 45-degree inflow case. Therefor only these cases are depicted. Finally, since the beam model only serves as a quick check only (graphical) stress plots of the jackets are investigated rather than comparing numerical results.

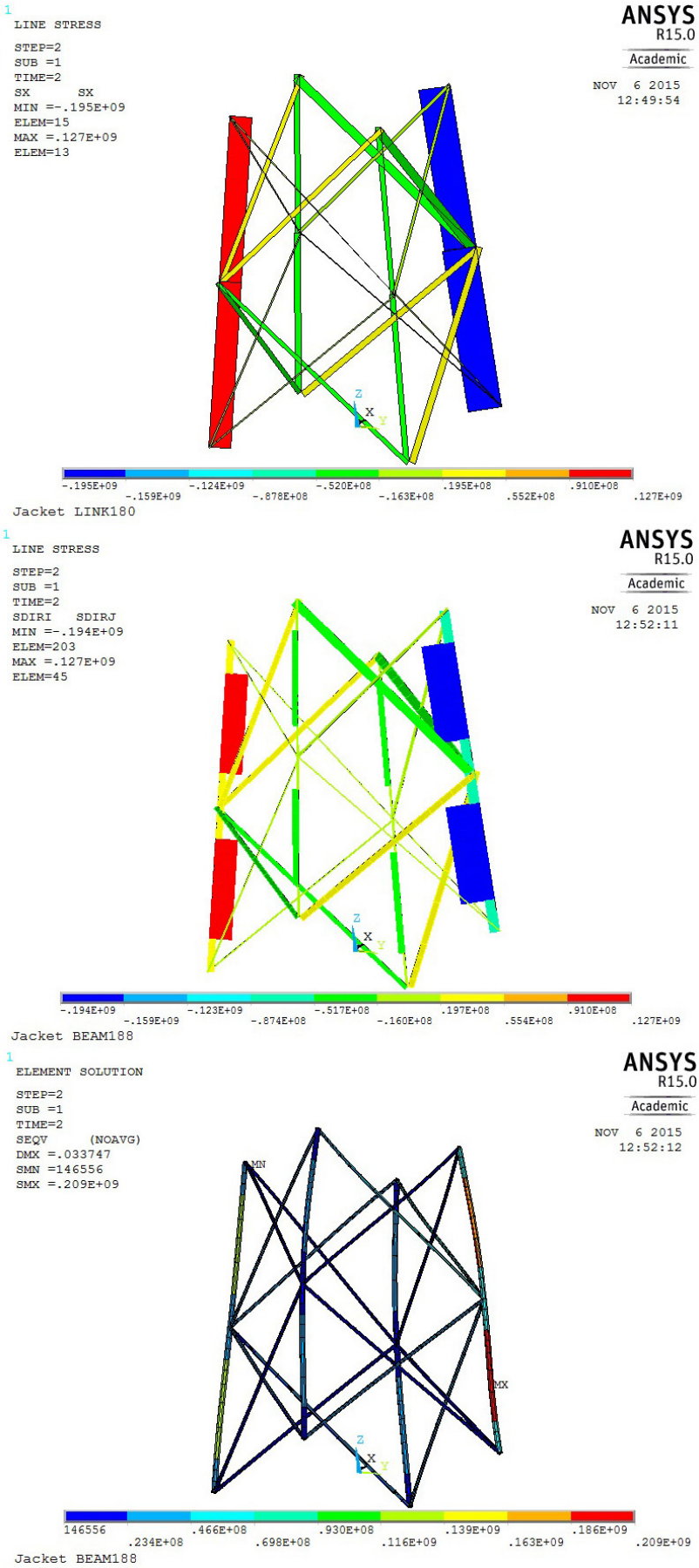

Figure 4. 8 - Princes Amalia internal member stresses for DLC 1.
Axial truss stresses (TOP), Axial beam stresses (MID), Mises beam stresses (BOT)

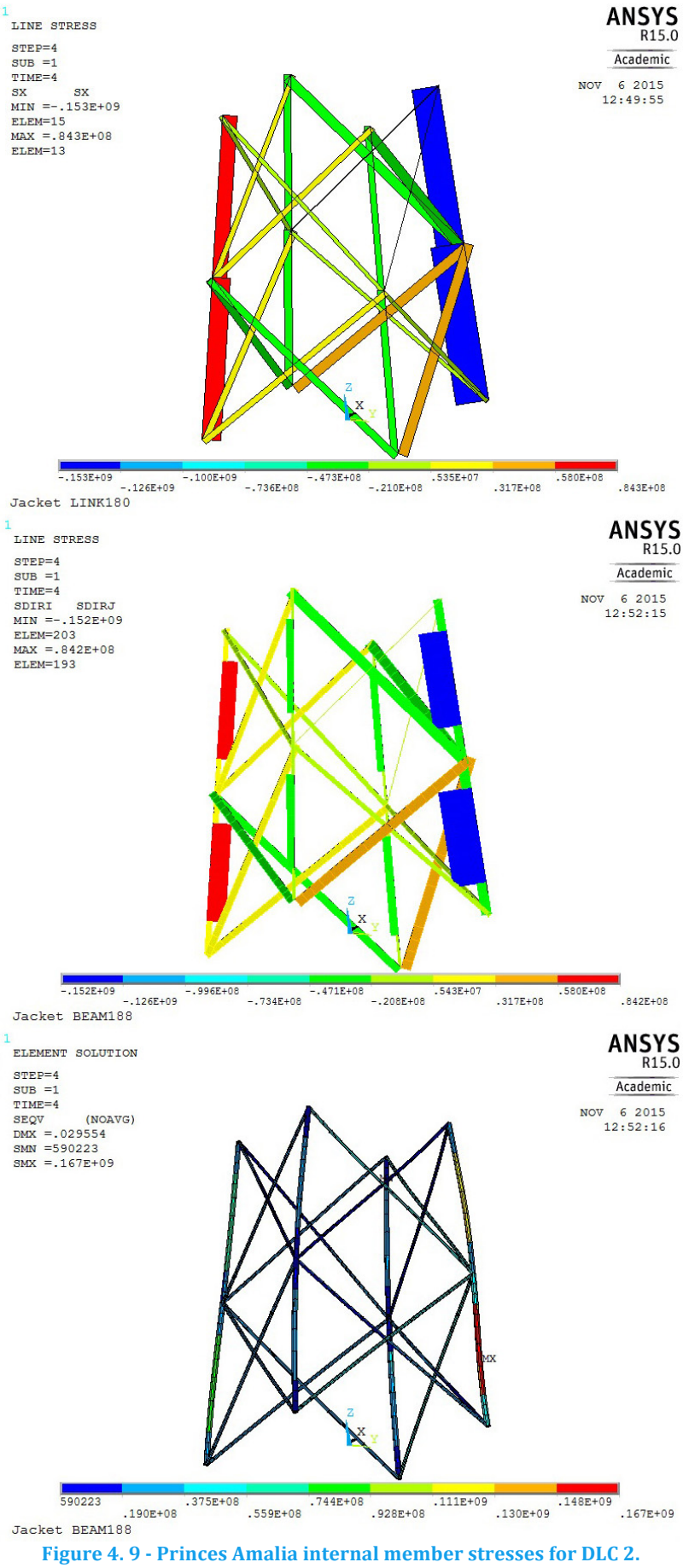

Figure 4. 9 - Princes Amalia internal member stresses for DLC 2.
Axial truss stresses (TOP), Axial beam stresses (MID), Mises beam stresses (BOT)

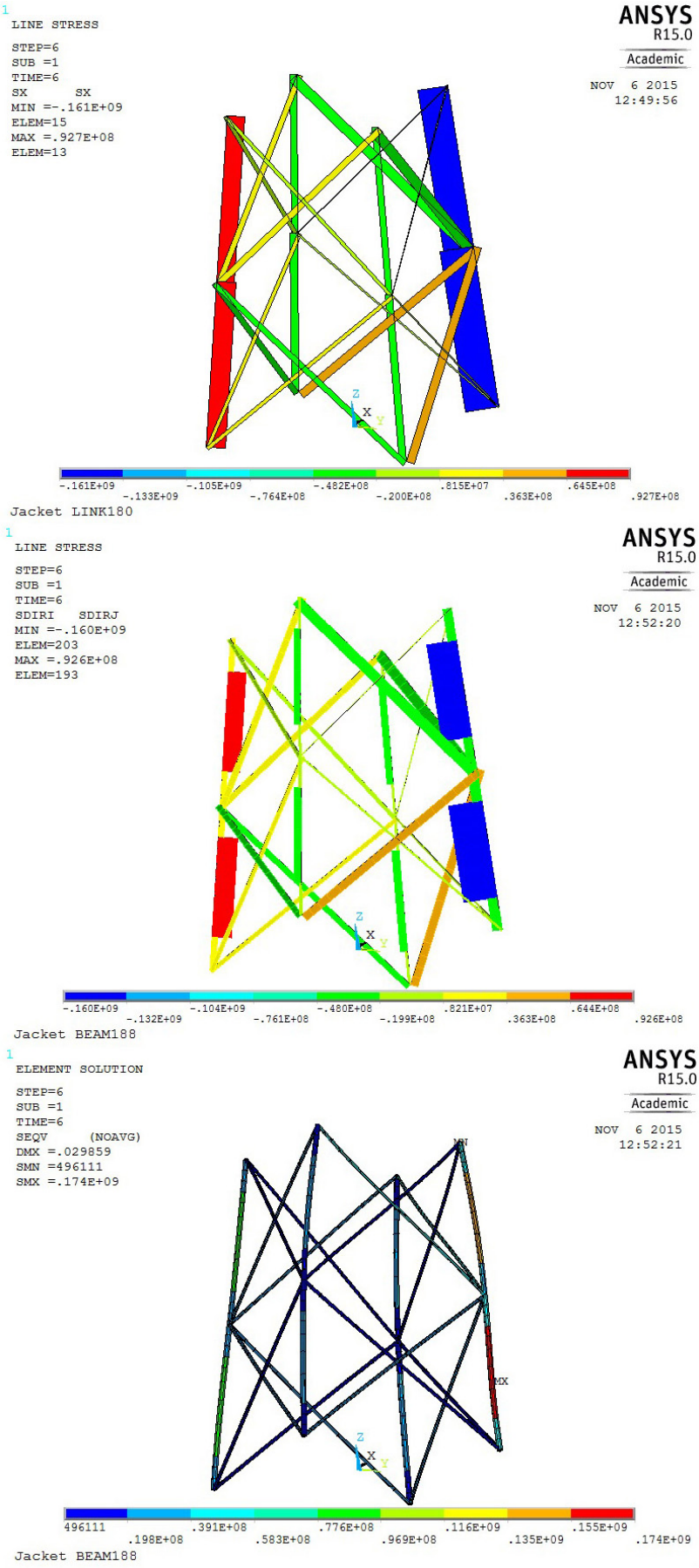

Figure 4. 10 - Princes Amalia internal member stresses for DLC 3.
Axial truss stresses (TOP), Axial beam stresses (MID), Mises beam stresses (BOT)

Table 4. 3 shows maximum structure stresses for the Princes Amalia farm. Inspecting the table shows that when only axial stresses are considered (first two columns), the truss and beam model have a similar result. However, when non-axial loads are taken into consideration the resulting von Mises comparison stresses are up to 9 percent larger. When sample points for Alpha Ventus and SJOEMF are observed, a similar load difference is found. Maximum structure loads for these locations are given in Appendix B57 and B58.

DLC	Truss axial	Beam axial	Beam Mises	Diff (%)
1	1.95E+08	1.94E+08	2.00E+08	3.0
2	1.53E+08	1.52E+08	1.67E+08	9.0
3	1.61E+08	1.60E+08	1.74E+08	8.0

Table 4. 3 - Princes Amalia maximum stresses

The most logical explanation for these differences is traced back to the way the model is constricted. The two upper plots in Figure 4. 8 to Figure 4. 10 show line stresses while in the bottom plot of these images an element solution is shown. For line stress plots, only average stresses in axial direction are shown. For the element solution however, the whole member is meshed. This way stresses are calculated for each node in the mesh, which allows for estimation of a more precise stress distribution. Since elements in the beam model are rigidly connected, an internal stress distribution is formed in member cross sections. Using the element solution this stress distribution can be shown while the line stress result is unable to show stress variations. When the average stress of this distribution is taken, the same stress as for the line stress result is probably found. This variation is illustrated in Figure 4. 11. In this image a example stress distribution is depicted from the center to the side of a member (R for radius). The whole cross section experiences an average stress (σ_{avg}) while the outsides of the member experience a stress variation due (σ_{var}) to, for example, bending moments.

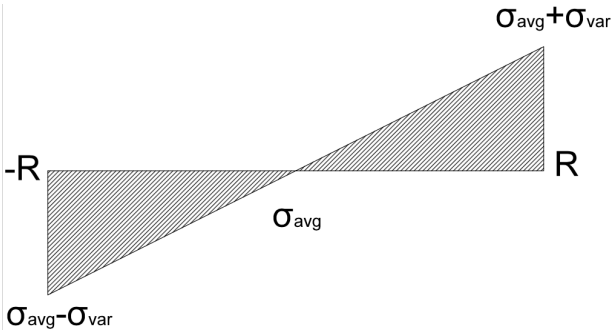

Figure 4. 11 - Stress variation in member cross section

Taking the above into account, it follows that the assumption that members can only experience axial loads and are connected using joints does not result in a great loss of model precision. There is however some loss in accuracy since no cross-sectional stress distribution can be found.

As a final note, further inspection of the beam model shows stresses at member edges being smaller as those the middle of a member. This is due to the increased wall thicknesses of the internal member sleeves. Since for this model no stress concentrations are considered, a lower stress is found.

4.3.4 Untested assumptions

At this point there are still some unverified assumptions. These assumptions are not tested since these lie beyond the scope of this thesis. However, in an effort for completeness of this study, some key simplifications are briefly discussed. Since the focus of this thesis surrounds jacket design, emphasis is put on this part of the structure.

The following key assumptions are not tested for validity:

1. Quasi-static model
2. Airy wave theory
3. Summation of members to single vertical pile
4. Load distribution over nodes
5. Stress concentrations
6. Buckling theory

The quasi-static model
As noted in paragraph 3.5.1, quasi-static in-place behavior of a steel space frame structure is considered. Meaning time dependency on external loads and internal load reactions are not fully addressed in the analysis. This results in a great simplification of the engineering model but also has its downside. Namely, strong time dependent phenomena such as wave slamming and gusts could only be taken into account to a certain extent. If time dependency were to be tested, additional input data is required. One possible way to test the quasi-static model for validity is by comparing results with linear-elastic code programs such as DNV GL's Bladed package.

Airy wave theory
Linear wave theory is often used to get a first insight in intensity of wave loads. However, when a more detailed load description is required, engineers often resort to higher order non-linear wave theory such as Stokes stream functions. These analyses are much more complex to program and are therefore not used in the preliminary design phase, for which the engineering model is created. Airy theory is valid for areas where wave motion is not restrained by the sea floor. Thus, this theory is more valid for areas further from shore. One simple way to check validity of Airy theory is by resorting the wave theory diagram of Figure 11 in chapter 2.

Summation of members to a single vertical pile
Jacket members are combined in one single vertical pile in an effort to reduce load complexity. Application of this trick completely neglects any effects of spatial separation. One further loss of accuracy arises from load reduction from decrease of average flow speed due to flow blockage. When a stream flows past an object a wake is formed. This wake effectively reduced the flow speed. Therefore, any object placed behind another one is exposed to lesser loads than if it were placed in an unobstructed flow. This effect is not taken into account in the current engineering model. The most straightforward way to test this assumption is by modeling these phenomena using computational fluid dynamics (CFD). This is however time consuming and costly and therefore outside the scope of the engineering model.

Load distribution over nodes
One further step to reduce load complexity arises from the way loads are assumed to act on the structure. Namely, rather than members being subjected to a distributed load, the load is summarized and divided over member endings. For (horizontal) external loads, an over estimation of loads arises at the bay top. Obviously, since external loads are summed, load estimation at the bottom of the bay is still correct. However, as a result of load separation over nodes, brace loads are over estimated while leg loads turn out lower. This load over estimation has to do with the brace and leg angle with respect to the flow. Since legs are positioned almost perpendicular to the flow it's loads are almost fully transferred to braches, which are much more aligned with it. Second, vertical loads that result from bay weight are assumed to only act at the bay's bottom. This way braces are not affected by internal forces and moments as due to of their own weight. If gravitational loads were to be spread over the top and bottom of the bay a similar load over estimation would occur as for brace loads for environmental loads. Namely since legs are aligned almost parallel to gravitational loads, these would bear most of gravitational loads from braces as well. The load distributive effects can only be taken into account properly by incorporating load distribution on members in the design. This would however eliminate the possibility to use truss elements due the formation of non-axial member loads.

Stress concentrations
Since these type of locally increased loads are highly un-linear, the only way to model these in a simple manner is by using engineering approximations. Here by 'engineering approximation' is meant an approximation of reality rather than a accurate problem description. Furthermore, since the size of stress concentrations is very dependent on sudden changes in geometry, a more detailed description of joint connections is needed. Stress concentrations can, for example, be investigated by modeling them in FEM software such as ANSYS. Since stress concentrations are only a small part of this thesis, no indication can be given whether stress concentrations are over or under estimated.

Buckling
Analogue to stress concentrations, buckling is a highly non-linear phenomenon as well. In the current engineering model, buckling is only described using simple engineering approximations as prescribed by standards. Large model simplifications are made in order to apply this theory. Simplifications contain, among others, only axial member loading and that member ends are restrained in movement but can still rotate freely.

Since these assumptions differ from reality by a great amount, results from the buckling analysis should be inaccurate. Furthermore, since prescribed buckling theory resulted in large diameters with small wall thicknesses, buckling penalty constrains are used. These constraints, which mainly restrict the diameter over wall thickness ratio, result in (heavy) conservative member designs. A more detailed analysis is needed to gain a better insight in buckling. Non-linear buckling analysis from ANSYS should be able to answer unresolved questions surrounding this phenomenon.

4.4 Model output

In addition to providing optimal output geometry as a result of the implemented design constraints, further output is generated during of the design process. This output helps the user evaluate result by giving a sense of the inner workings of SJOEM. Model outputs are discussed according to the design pathway introduced in chapter three. In an effort to retain clarity, only output of the Princes Amalia farm is discussed unless stated otherwise. Results of the two remaining sample points are found in appendix B and only differences and similarities with the Princes Amalia case are pointed out in the main text.

4.4.1 RNA output

Since the RNA is largely treated as a black box the data is only briefly discussed here. Table 4. 4 shows estimated loads for DLCs introduced in chapter 3. Inspection of the table shows the largest RNA loading is present at DLC 1. This confirms expectations since for this load scenario the turbine is operational thus creating a large thrust force (F_x). This thrust force is much greater than drag loads present during storm conditions for DLC 2 and 3. Since gravitational load is only a function of RNA weight, each of the three vertical loads is equal.

RNA Loads Princes Amalia						
DLC	F_x (N)	F_y (N)	F_z (N)	M_x (Nm)	M_y (Nm)	M_z (Nm)
1	1792208	0	2296864	0	23896109	0
2	833778	0	2296864	0	11117040	0
3	1008871	0	2296864	0	13451619	0

Table 4. 4 - RNA loads sample set 1

When the three sample points are investigated (Appendix B16 to B18) similar observations are made. Finally, when comparing results to each other, the largest structure RNA loading is observed for SJOEMF. This result is expected since this the Siemens turbine has the largest rotor diameter among sample points.

4.4.2 Tower output

Tower geometry is determined for 10 segments along its height. As discussed in the previous chapter, for each of these segments, the minimal cross-sectional area that passes DLC 1 to 3 is used. External loads are balanced with internal stresses by evaluation of yield and buckling. Solely designing by yield and buckling however resulted in large diameters and small wall thickness combinations not observed in practice. Therefore, a diameter over wall thickness penalty constraint is implemented to achieve diameters and wall thickness combinations that conform more to expectations. One explanation for large diameter and small wall thickness combinations is found when looking at equation (4.4). Using this equation the maximum cross-section stress (σ_{max}) is calculated as a function of tower diameter (D) and wall thickness (wt). For this equation, diameter and wall thickness are denoted using parenthesis (e.g. $F_x(D)$) meaning the respective input value for the equation is a function of these variables.

$$\sigma_{max}(D,wt) = \sqrt{\left(\frac{F_x(D)}{A(D,wt)}\right)^2 + \left(\frac{F_z(D,wt)}{A(D,wt)} + \frac{M_y(D)\cdot D}{2\cdot I(D,wt)}\right)^2} \tag{4.4}$$

Stress is the ratio of loads over an area resisting these loads. Roughly speaking, in the equation above loads increase linearly with diameter. For example, when doubling the diameter, twice the drag load is exerted (F_x). Since overturning moment is a function of drag load, only also twice the overturning moment from tower drag is found (M_y).

However, when looking at the resisting area, a different observation is made. The cross-sectional area (A) has a quadratic increase and moment of inertia (I) increases with the power of four. Thus, when wall thickness is not considered, for twice the diameter four times the area and sixteen times the moment of inertia is found. Therefore when wall thickness is not considered the lowest stresses are found for an infinitely large diameter. When this derivation is applied to one containing wall thickness and the minimal area is estimated, this is found for an infinitely large diameter with infinitely small wall thickness.

Since structures with small wall thicknesses are prone to buckle, bucking theory was thought to put a hold to this runoff to extreme. Application of this theory unfortunately still provided undesired results; the runoff was largely maintained but resulting diameter where still much larger as observed in practice. In an effort to put a further constrain on diameter growth, RNA mass eccentricity is taken into account. Namely, tower with bigger diameters need a larger overhang such that blades do not hit the tower. The larger the overhang the greater the overturning moment exerted by it. Implementation of overhang effectively creates an additional load term thereby putting an additional limit on diameter growth. While the RNA overhang term did limit diameter growth resulting diameters where still larger as observed in practice. As a final effort, a diameter over wall thickness ratio penalty constraint of 200 is adopted, this time resulting in acceptable geometries. As discussed in the previous chapter, this ratio is a slightly altered version of the one adopted from TeamPlay.

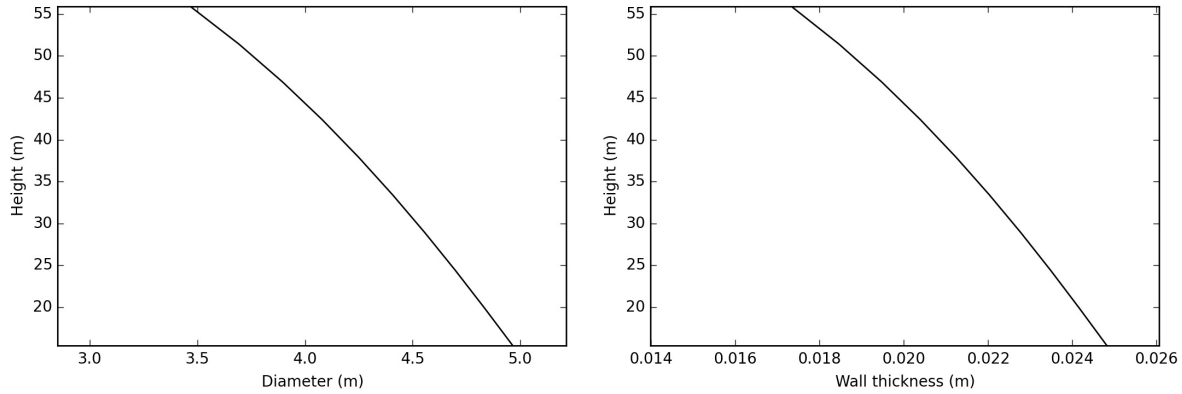

Figure 4. 12 - Princes Amalia tower geometry

Inspection of tower geometry depicted in Figure 4. 12 shows the geometry is constrained to the diameter over wall thickness ratio of 200. This same ratio is found for Alpha Ventus and SJOEMF sample points in Appendix B21 and B22. Additionally, inspection of the tower load distribution as shown in Figure 4. 13 show DLC 1 is the design driving load scenario. This as a result of the large trust force generated at the RNA. For Alpha Ventus (appendix B24) and SJOEM (appendix B25) the more extreme weather conditions cause drag loads on the tower to actually exceed loads induced by thrust force for DLC 1. Inspecting change in transversal loading (F_x) show that drag loads on tower segments are larger for the second and third DLC. This is expected due to the higher wind speeds in these load cases. Appendices C1 and C2 show respective calculations used to address yield and buckling for the base of the tower for DLC 1 of Princes Amalia.

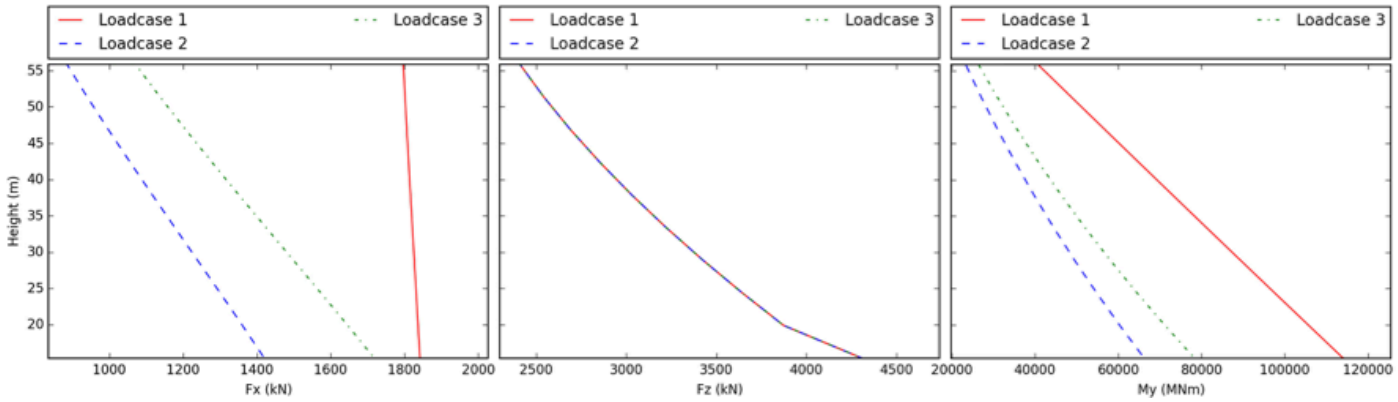

Figure 4. 13 - Princes Amalia tower loads for DLC 1 to 3

4.4.3 Jacket output

Jacket load output is discussed analogue to the design procedure introduced in paragraph 3.5.3:

1. Applied external loads
2. Section loads along height of structure
3. Nodal loads (not discussed)
4. Internal member forces
5. Member geometry
6. Sleeve dimensions

Since the load assessment is extensively treated in chapter three, only model output is discussed here. Furthermore, the process of creating nodal forces from section loads is not discussed since these can be easily found using relations given in chapter three.

4.4.3.1 Applied external loads

For each bay, external loads from wave particle movement are estimated using the Morison equation. This is done in a two-step process. Firstly drag induced forces on a bay are found using a drag equivalent pile diameter. Second, using the equivalent pile diameter for inertia, inertia forces are approximated. Finally, using drag and inertia terms, their induced moments are estimated using basic mechanics relations.

Morison loads are depicted in Figure 4. 14 for Princes Amalia farm. Legend notation 'LC' show respective design load case and 'A0' and 'A45' indicate respective inflow scenarios at zero and forty-five degree with respect to flow direction.

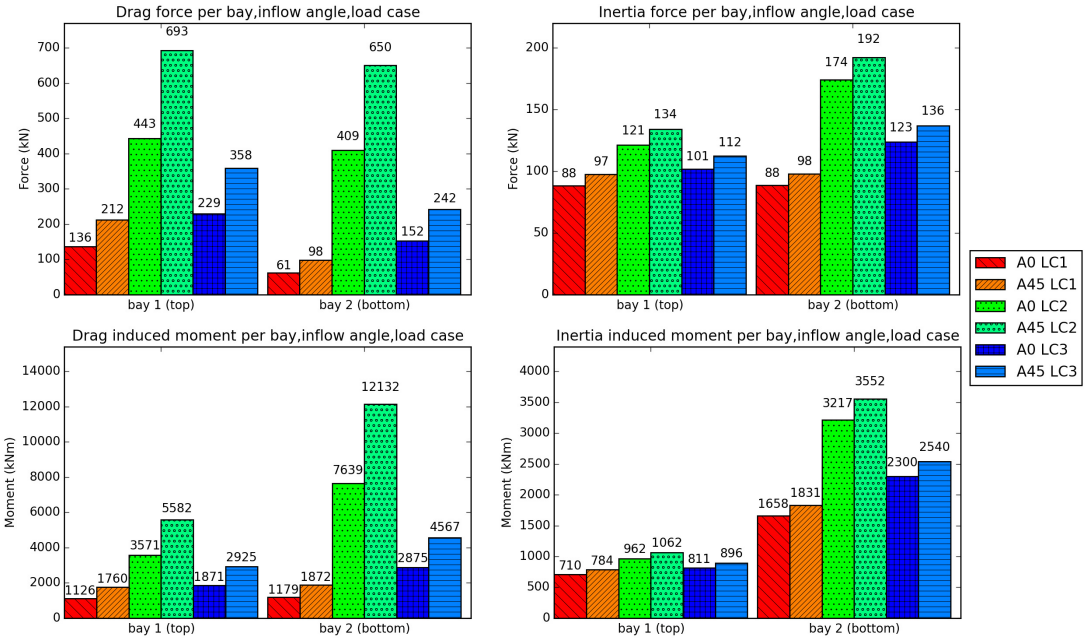

Figure 4. 14 - Princes Amalia external jacket loads for DLC 1 to 3

Observation of the image shows external loads on bottom bays being larger than for upper ones. This goes against expectations since stream speed decreases when moving to the mudline from sea level. However, since the top bay is not fully submerged a lower load is exerted on it. Furthermore, when comparing loads for the two inflow scenarios (A0 and A45), loads for the forty-five degree inflow angle are always higher than for the zero degree one. This is the result of the forty-five degree cases having a larger equivalent diameter as their counterpart as a result of the different member configuration with respect to the flow. Combined loads are found by taking the root sum square of respective drag and inertia loads (Figure 4. 16). Note that while external forces are about the same size, the moments induced on the other hand differ with up to a factor of two between the two bays. This is again the result of the upper bay not being fully submerged.

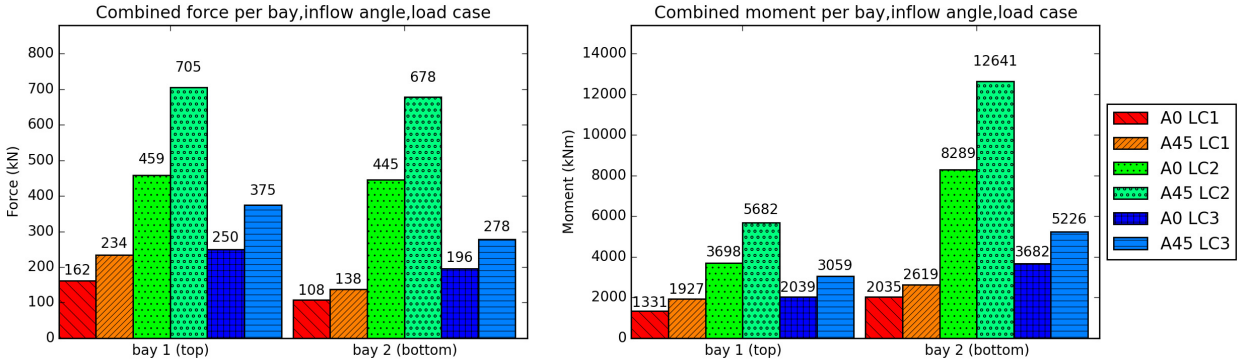

Figure 4. 15 – Princes Amalia combined wave loads per bat for DLC 1 to 3

Appendix B11 to B16 show the above-discussed graphs for each sample point. For the other sample points the same observations are made with the only difference being that SJOEMF has an additional bay. This results from its much larger site water depth with respect to the other sample points.

4.4.3.2 Section loads

By combining external bay loads with tower bottom loads and maintaining the same set of assumptions as those in chapter three, the load distribution along the jacket structure is found. As a result, forces only act on member ends along imaginary cross-sectional planes located at member ends.

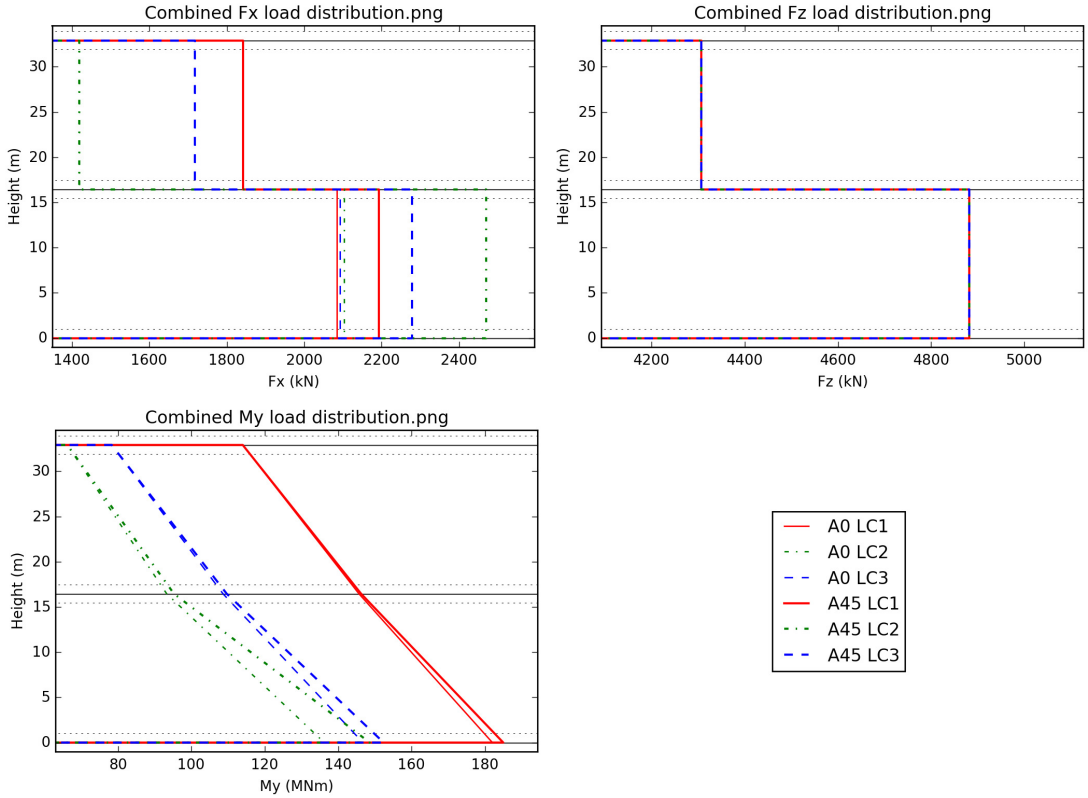

Figure 4. 16 - Princes Amalia section loads along jacket for DLC 1 to 3

Figure 4. 16 shows resulting section loads for the Princes Amalia farm. In this image, solid black horizontal lines indicate the locations of cross sections where external forces are applied. Note that section forces only change along these planes as a result of external loads being transposed to the nodes located at member endings. Horizontal dashed black lines just above and below the solid black ones emphasize locations for force balances. Internal member loads are found using these balances. It follows that for any bay, two load balances (at the top and bottom) of a bay have the same input loads (F_x and F_z) while having a different overturning moment (M_y). As explained in chapter three, difference in member loads from these (two) balances per bay serve as input to establish load reallocation due to coupling of front and back of the structure (Paragraph 3.5.5 step 4).

Further inspection shows that for the Princess Amalia farm, horizontal external loads from DLC 2 and 3 are actually larger at the mudline compared to DLC 1. This observation again confirms expectations since, for DLC 1, the largest horizontal force contribution is made by thrust force on the RNA. As a result of the relatively mild sea state at the Princes Amalia farm, only a small load is added as a result of hydrodynamic activity, which is seen from the smaller load jumps. Since for DLC 2 and 3 much rougher sea states are evaluated, it follows that horizontal forces are much larger here. Inspection of induced overturning moment from environmental loads (M_y) reveals that for the Princes Amalia farm, moments formed in DLC 1 are not surpassed by moments of other load cases. However, the difference between DLC moments does become smaller when moving from the interface level towards the mudline. This is the result of DLC 2 and 3 being exposed to larger wave loads than for DLC 1.

When comparing the external load distribution of each sample point (Appendix B32 to B34), three different maximum load sources are found. As discussed above, for the Princes Amalia farm the design driving DLC is the first one, where a normal sea state and an operating turbine are evaluated. For the top of jacket structures in the Alpha Ventus and SJOEMF farm, maximum external loads are a result of the storm scenario of DLC 3. However, for the bottom of the structure the maximum sea state evaluated in DLC 2 surpasses that of DLC 3.

4.4.3.3 Member loads

Member loads are found by balancing external loads with internal loads. For each load case a member load is found for each inflow scenario, resulting in a total of six load scenarios per sample point. In Figure 4. 17 to Figure 4. 19 internal member loads are displayed for each of these six scenarios. From symmetry relations is follows that only half the structure has to be evaluated of each inflow scenario. Furthermore, green notations indicate loads being tensile while red notations indicate a member exposed to a compressive load.

Further inspection of these images helps give a solid insight in the jacket physics. Firstly, front legs are always subjected to tensile loads while legs at the back are always subjected to compressive loads. This is mainly caused by direction of forces inflicted as a result of the overturning moment. On the upstream side, these loads point in the upward direction while on the back they point downwards. Second, leg loads at the back are always larger than in the front. This is the result of gravity and overturning moment force being counter-directional at the front, partially cancelling each other out, while being co-directional at the back, making them additive. Thirdly, braces connecting the left top-side to bottom right side of a bay are mostly subjected to compressive loads while the other members are mostly subjected to tensile loads. This is a result of the directionality of horizontal loads with respect to the members they act on. On the left side members lay in the same quadrant as the load, thereby forming a compressive load wile on the right side external load lay in opposite quadrants, resulting in a pulling load on the brace. Roughly speaking, the largest loading contribution of legs is a result of vertical loads while the largest contribution of brace loads is a result of horizontal loads since these are most aligned with that respective load direction.

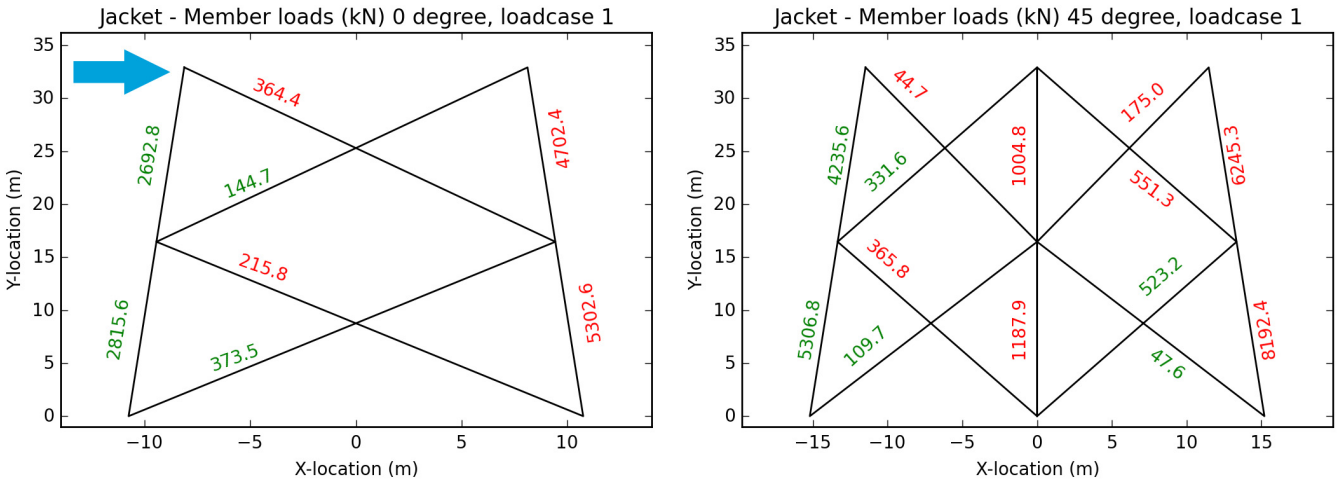

Figure 4. 17 - Princes Amalia jacket member loads for DLC 1

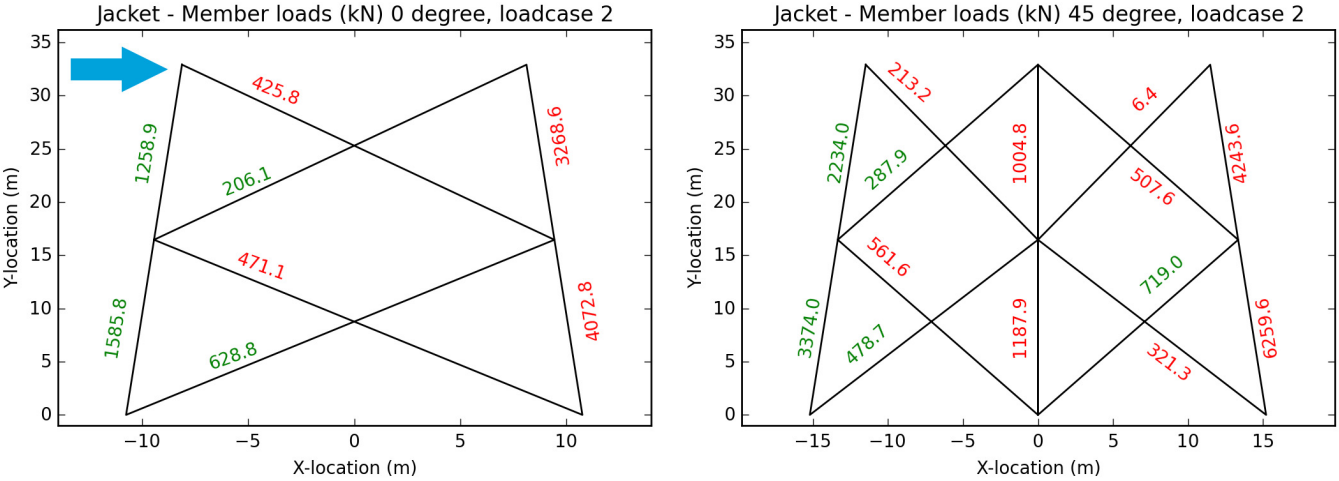

Figure 4. 18 - Princes Amalia jacket member loads for DLC 2

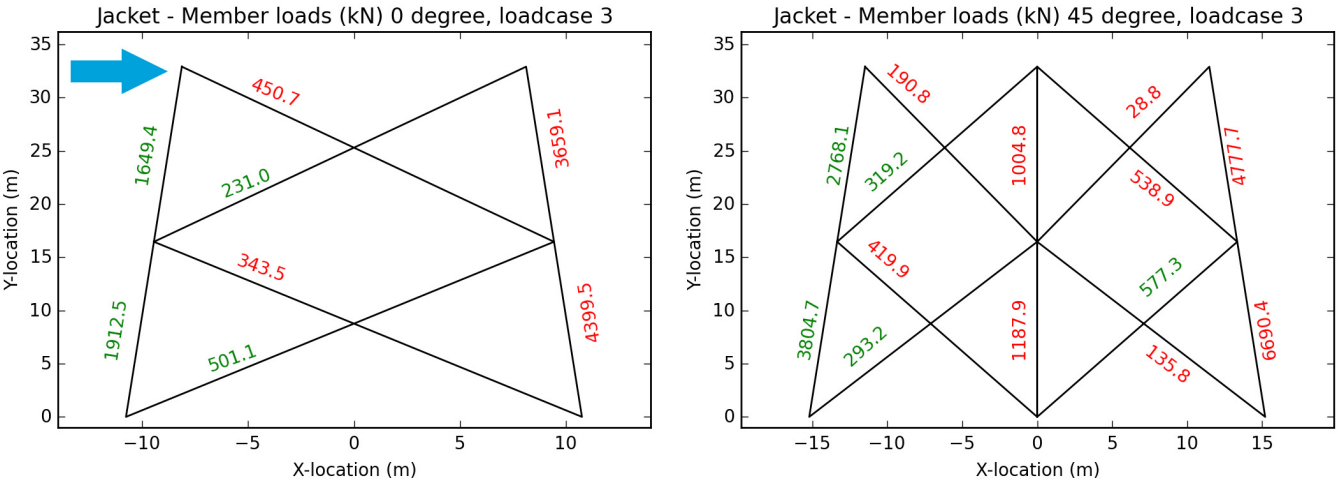

Figure 4. 19 - Princes Amalia jacket member loads for DLC 3

For Alpha Ventus and SJOEMF the same observations are seen and are therefore not discussed. Respective plots are found at appendix B38 to B43.

4.4.3.4 Member dimensions

Using member loads, optimal cross sections are determined using the iterative process introduced in chapter three. Since real-world environmental loads can emerge from any direction, for each bay member geometry is determined from maximum occurring forces.

Table 4.3 shows maximum loads for each bay of the Princes Amalia wind farm. This table is similar to Table 4. 2 but now the outermost right columns removed since this point ANSYS loads are not of interest. The table's mapping is discussed in the previous chapter (using Figure 4. 6) and thus not treated at this point.

Inspection reveals that, for this sample point, all maximum loads occur at the 45-degree inflow case. This confirms expectations. Namely, overturning moment occurring in a bay is withstood by one leg rather than by two, as is the case for the 0-degree scenario. When comparing the origin of maximum loads, different design-drivers are found per bay. For Princes Amalia, roughly speaking, the first DLC is design driving. In contrast, for the sample point located furthest from shore (SJOEMF, Appendix B46), load case three turns out to be design driving. Finally, Alpha Ventus's design is constructed as a function of loads from all DLCs (Appendix B45), which is expected since environmental parameters are larger than for Princes Amalia while not being as extreme as for SJOEMF.

Bay	Member	Location			Load	
		Load case	Angle	Side	Direction	Size (N)
1	Leg	1	45 right	right	Compressive	6.25E+06
1	Leg	1	45 left	left	Tensile	4.24E+06
1	Brace	1	45 right	left	Compressive	5.51E+05
1	Brace	1	45 left	right	Tensile	3.32E+05
2	Leg	1	45 right	right	Compressive	8.19E+06
2	Leg	1	45 left	left	Tensile	5.31E+06
2	Brace	2	45 left	left	Compressive	5.62E+05
2	Brace	2	45 right	right	Tensile	7.19E+05

Table 4. 5 - Princes Amalia maximum member loads per bay

Using these maximum loads, optimal dimensions are extracted from the following three design constraints:

1. Yield check from maximum load of member
2. Global Euler buckling from maximum compressive load of member
3. Local buckling constraint for geometry

By combining maximal loads of Table 4.3 to the above design constraints, the member geometry of Table 4.4 is found. Here columns D_{leg} and D_{brace} show respective leg and brace diameter while wt_{leg} and wt_{brace} show accompanying wall thickness.

Bay	D_{leg} (m)	wt_{leg} (m)	D_{brace} (m)	wt_{brace} (m)	Bay weight (kN)
1	0.51	0.02	0.31	0.012	451
2	0.56	0.022	0.34	0.013	590

Table 4. 6 - Princes Amalia member geometry per bay

Inspecting geometry changes per bay an increase in dimensions is observed when moving from sea level to the mudline. This is obviously the result of load increase in members since external forces are summed along this pathway. Appendices B47 to B49 show a similar geometry increase for each of the sample points. Respective yield, global buckling and local buckling jacket member calculations are given as example in appendix C3 to C5 for the member with the highest load, which is located at the fifth row of Table 4.3. For this example design driving constraints are found at the minima constrained by the local and global buckling limit.

4.4.3.5 Sleeve dimensions

Sleeve dimensions are determined from stress concentration factors (SCF) derived from Efthymiou equations proposed by the American Petroleum Institute (API 2000). Stress concentrations are found from multiplication of axial member stresses and these factors. From these increased stresses an additional member wall thickness is estimated using a yield constraint. Table 4.5 depicts additional required wall thicknesses for these sleeves. Columns 'Δwtleg' and 'Δwtbrace' give the additional required sleeve wall thickness while columns 'Lleg' and 'Lbr' show respective member length. Finally, the two outermost right columns give the SCFs for the respective leg (l) and brace (br). Appendices B50 till B52 show results for each of the three sample points. Finally, Efthymiou equations used to estimate SCFs for the bottom bay of underlying table are given in appendix C6.

Bay	Δ wtleg (m)	Δ wtbrace (m)	Lleg (m)	Lbr (m)	SCFl	SCFbr
1	0.061	0	0.9	0	5.87	3.85
2	0.067	0	0.9	0	5.41	3.48

Table 4. 7 - Sleeve dimensions per by for Princes Amalia farm

A first glance of Table 4. 7 shows that braces have no additional sleeves while still having stress concentrations. This means that if stresses would be equal to the stress concentrations the total stress would still be lower than the material's yield stress. From this it is deduced that the member wall thickness was found as a function of a (single) buckling constraint. As discussed in chapter three, brace diameter is set equal to sixty percent of brace diameter and thus optimum brace cross-sectional area is only a function of one variable (wall thickness) and is therefore not found at the intersection of two design constraints but solely from the largest wall thickness for which all design constraints are fulfilled.

4.4.4 Pile output

Pile loads are estimated as a function of mudline base shear, gravity load, overturning moment and the distance between legs. By combining these loads with basic geometry relations the maximum pile loads are found. The method as proposed by Vugts (Vugts 2002) for un-inclined piles is discussed in chapter three. For the Princes Amalia farm, the pile top-loading scenario as depicted in Figure 4. 20 is found. In this figure pile numbering is equal to that used in chapter three. For clarity reasons this numbering is depicted once more in the bottom right corner of the figure. Appendix B53 to B55 show pile top loads for each sample point.

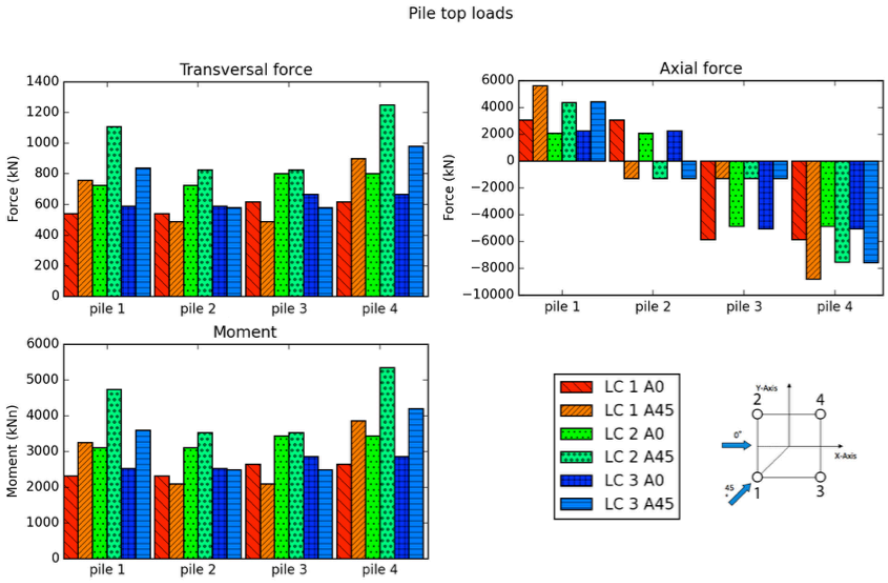

Figure 4. 20 - Princes Amalia pile top loads

Inspecting transversal loads for all three DLCs reveals a difference in load intensity. This does not confirm expectations based on statements by Vugts on pile load distribution (Vugts 2002) since here transversal force is taken as simply the base shear equally divided over the foundation piles. The observed difference is a result of residual loading that are a result of load relocation from reaction loads as discussed in paragraph 3.5.5. The image shows that this effect has an adjective effect on upstream pile while having an additive effect on downstream piles.

Further observation of all loads reveals that for the 0-degree scenario both upstream and both downstream piles are loaded equally. Furthermore, when the same analysis is done for the 45-degree inflow case a similar load allocation is found. The (single) pile upstream is loaded the least while the (single) pile downstream is loaded the most. This is obviously a result of gravitational loads and overturning moment having either an subtractive or additive effect due to being co- or counter- directional. The two middle members have the least axial load since they are not affected by overturning moments.

Pile top loads result in the minimal pile geometry given in Table 4. 8 when constrained to the four design constraints introduced in chapter three. The first two design constraints put a limit on pile wall thickness by means of yield and a minimal required wall thickness to prevent the pile from buckling during pile driving. The remaining constraints limit the pile's length by means of axial and lateral stability equilibrium. Pile geometry for Alpha Ventus and SJOEMF are found in appendix B57 and B58. For these tables and the one shown below, the first to third column give respective pile diameter, wall thickness and length while the final two columns give the estimated inflection point and pile mass.

D_{pile} (m)	wt_{pile} (m)	L_{pile} (m)	$d_{e\ pile\ (m)}$	M_{pile} (kN)
1.43	0.02	15.74	4.3	111

Table 4. 8 - Princes Amalia pile dimensions

Using pile geometry and top loads, design constraints are worked out for the design driving load case in appendix C7 to C10. That is, for DLC 2 at the 45-degree inflow scenario. Inspecting these appendices shows that for the pile in question the design driver for wall thickness is found at the crossing between buckling constraint for pile driving and yield stress while axial stability is the driver for length.

As a final note, pile diameters seem rather large, making a connection between legs and pile rather difficult. This problem could, for example, be avoided by implementation of a maximal leg to pile diameter ratio. A more detailed insight is however needed to estimate a fair ratio.

5

Conclusion

This study set out to create a simple and fast engineering model to aid engineers in their decision-making processes during the preliminary design phase. Such a model is desired since currently only extensive models exist. These models are costly, time consuming and require a large set of input data and are therefore not suited for this design phase. An engineering model is created where optimal offshore wind support structure geometry is estimated of a jacket structure. This optimum is found for the least required structure volume to withstand each of three design load cases. Additionally, the engineer is provided with several graphs and charts that give insight in structure mechanics and load distribution. Using this tool, the engineer is able to quickly compare potential offshore structures for given environmental characteristics.

The offshore wind support structure geometry is estimated in a three-stage process preceded by a simple RNA load assessment. For each stage, emphasis is put on one distinct structure part: tower, jacket structure and foundation piles. Geometry for each of these parts is determined using an integrative process where a balance is found between external and internal loads. Optimal geometry is found for the lowest structure volume that is able to withstand three design load cases. These cases represent likely to occur extreme weather scenarios.

Along the course of the thesis, several complications were identified. First, certain design simplifications adopted from literature based on offshore oil and gas platform design turned out to be less suited for jacket design. This is a result of oil and gas platform designs being guided by structure weight while offshore wind support structures are mostly shaped by environmental loading. Second, optimal tower and jacket geometry were originally thought to be found solely from the equilibrium of external loads with internal stresses by means of yield and buckling constrains. This resulted, against expectations, in very large structure diameters combined with small wall thicknesses. In an attempt to put a halt on diameter growth, a diameter over wall thickness ratio was added as additional design constraint. This resulted in more applicable designs, but at the cost of more conservative geometries. Third, member load distribution proved very sensitive to model simplifications. Namely, in an effort to reduce model complexity, the three-dimensional space frame model was reduced to several two-dimensional plane analyses. In this conversion process, small angles were 'flattened out' by assuming these as straight lines. These simplifications turned out to have a substantial load error in member load distribution, especially on bays further from the interface level as a result of error accumulation. Finally, assuming members being connected using hinges rather than taking these as rigid and assuming loads only act on member ends resulted in a further loss of accuracy. By doing so only average stresses in member cross-sections are found.

In contrast to complications, SJOEM also delivers multiple advantages. Using this engineering model the park designer gains insight in the impact of certain design choices. Thus allowing elimination of unfeasible design combinations on beforehand. Furthermore, when load distribution is observed a first insight is granted in which load cases are design driving for given environmental characteristics. This way more emphasis can be put on these DLCs in the course of the detailed design phase.

In its current state, the engineering model provides sub-optimal results. For future alterations to the model, new or changed design constraints need to be found. Emphasis should be put on forming constraints such that designs are not driven by the current (conservative) diameter over wall thickness ratios. One possible solution lies in a better description of buckling. Buckling theory as described by consulted standards should solely be used as a quick check for correctness rather than an optimization constraint. Apart from design constraints, renewed insight is needed in design simplifications that were adopted from the oil and gas industry. Finally, a clearer internal load description should be found if the engineering model is evaluated as a 3D model rather than a 2D plane simplification.

Taken together, a simple and fast jacket optimization tool has been created. By using this engineering model, offshore wind farm engineers have a new tool to assist them in the decision making process during the preliminary design phase. Since only eighteen easy-to-obtain parameters are required as model input, limited research is needed to check offshore wind structure designs for viability.

Appendix A – Input charts

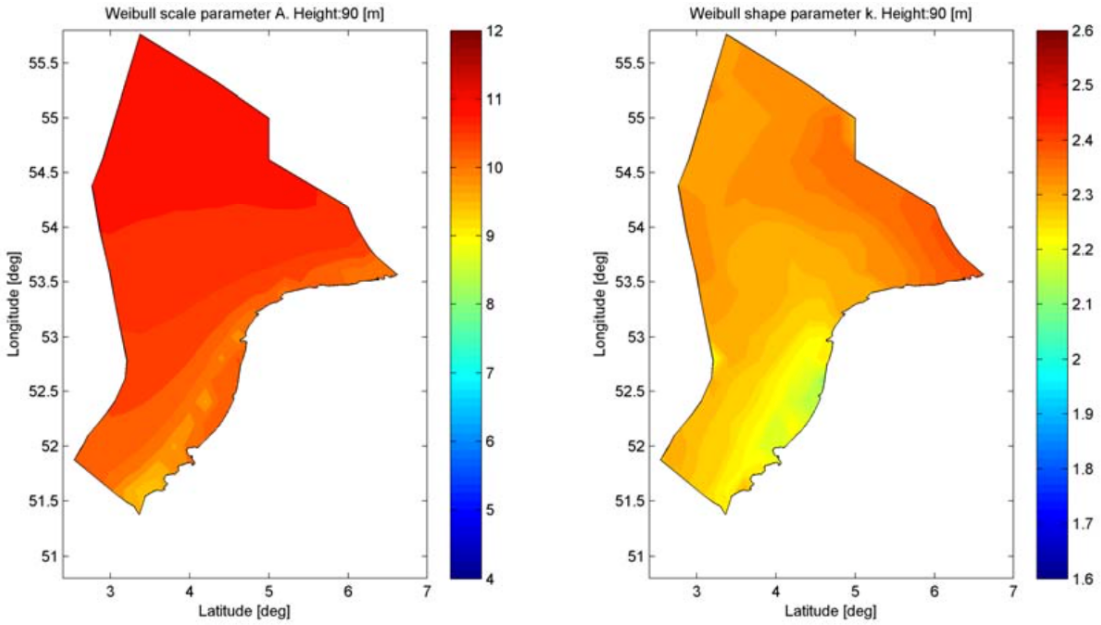

Appendix A. 1 - Weibull scale (left) and shape (right) parameters.
Image taken from: 'Offshore wind atlas of the Dutch part of the North Sea', ECN 2011

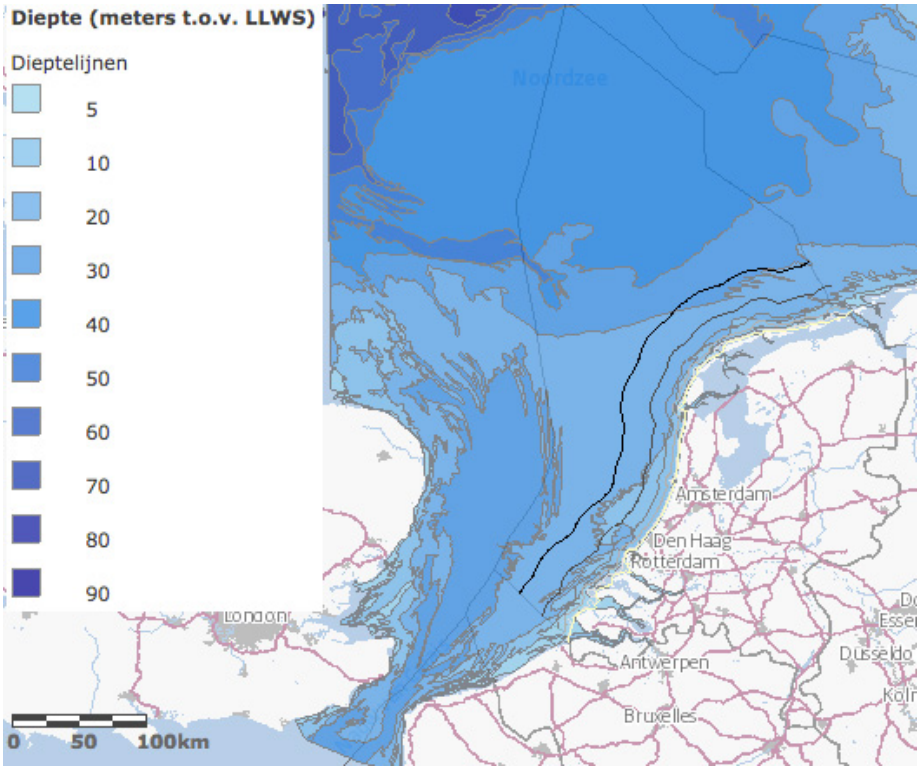

Appendix A. 2 - Depth chart of Dutch Territorial Sea. Image taken from Noordzeeloket (2009)

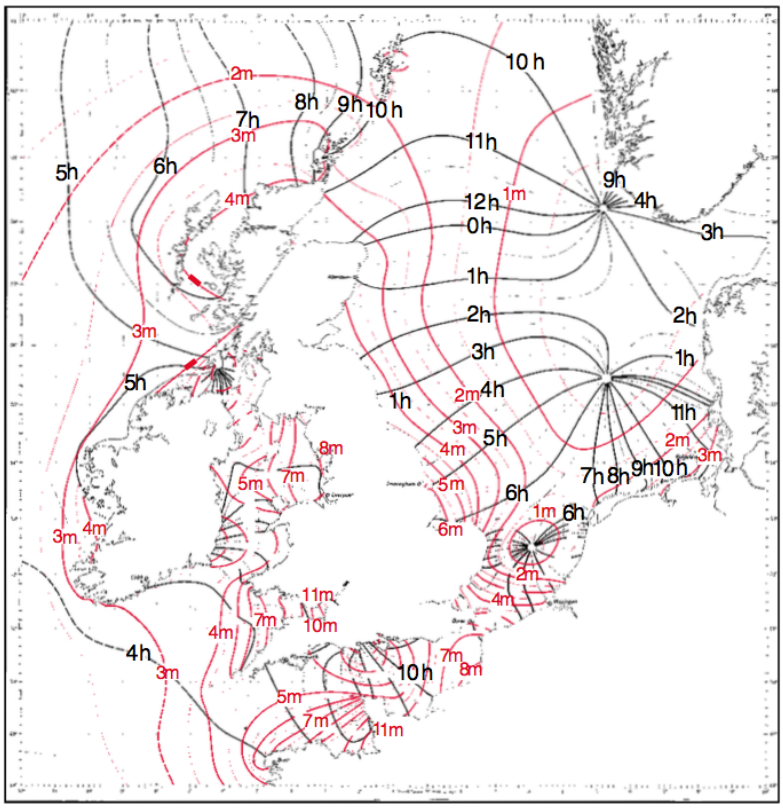

Appendix A. 3 - Mean spring tidal range (red) and tidal intervals with respect to moon's passage at Greenwich (black). Image taken from OSPAR quality status report (2000)

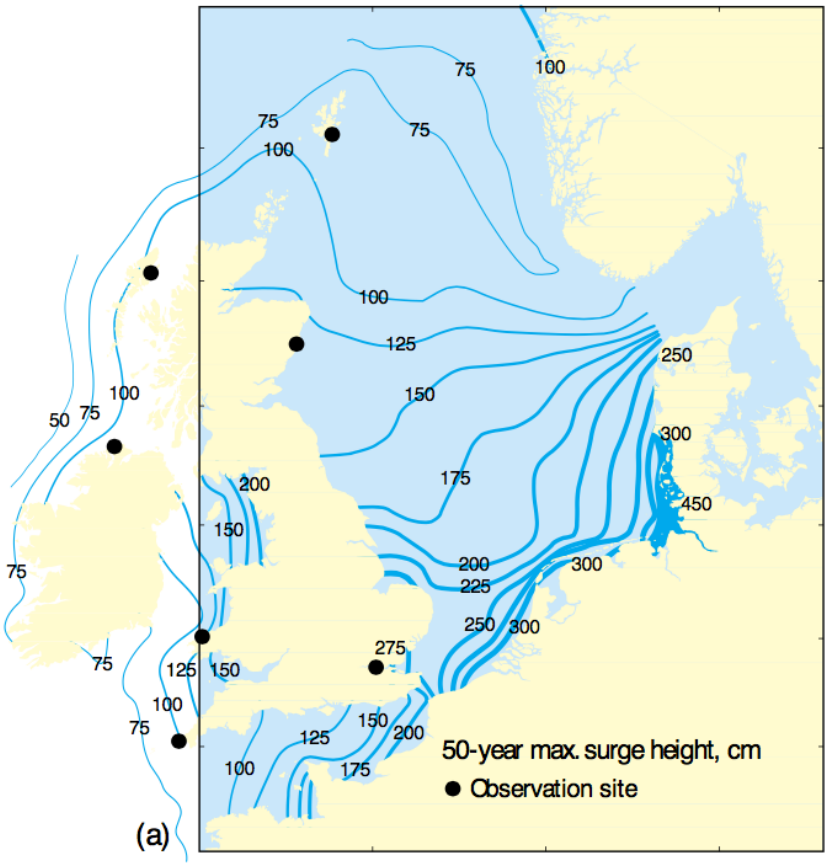

Appendix A. 4 - Estimated 50-year extreme surge height. Image taken from OSPAR quality status report (2000)

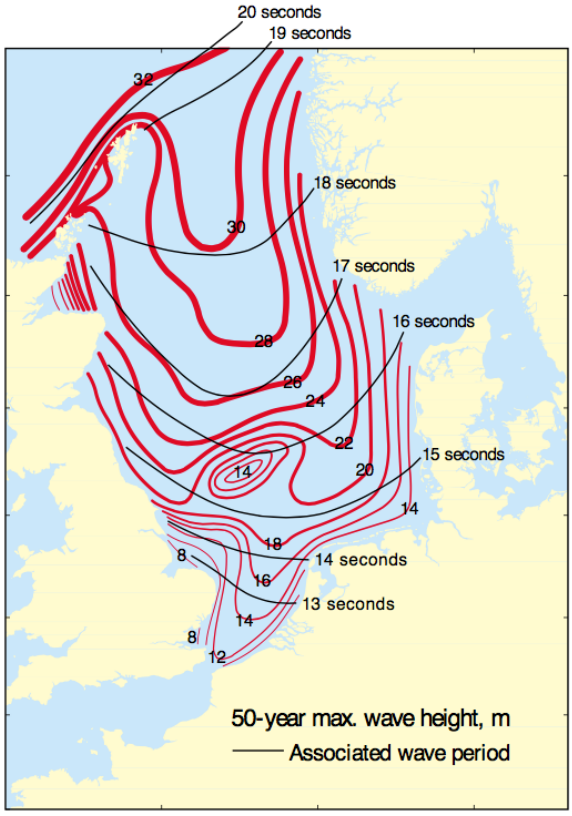

Appendix A. 5 - 50-year maximum wave height (red) and associated wave period (black). Image taken from OSPAR quality status report (2000)

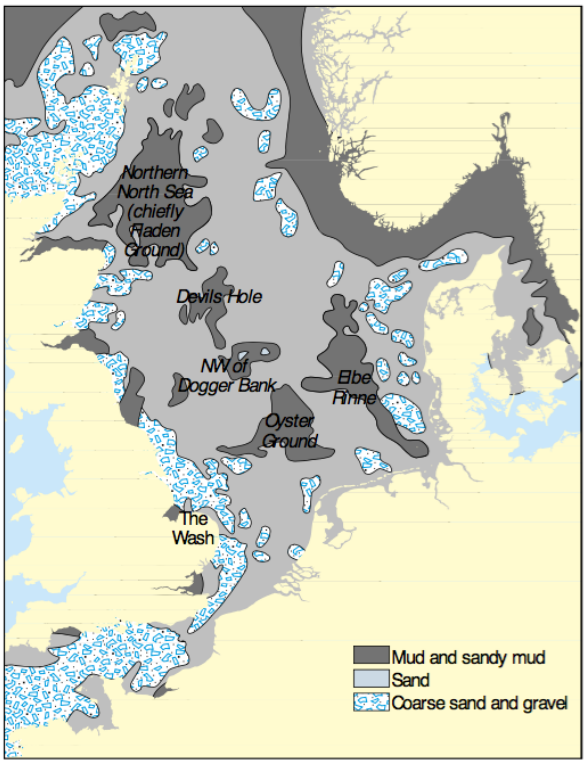

Appendix A. 6 - Soil type. Image taken from OSPAR quality report (2000)

Appendix B – Model output

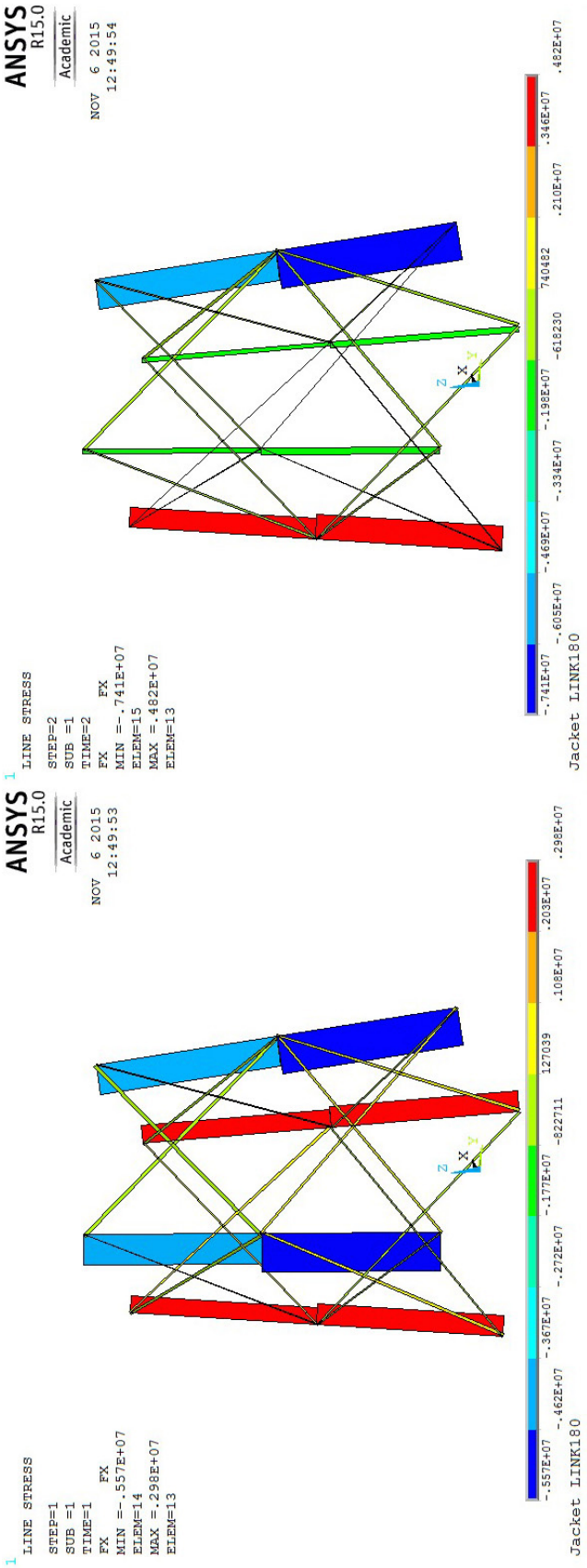

Appendix B. 1 - Ansys member loads for Princes Amalia farm DLC 1. 0-degree inflow (left) and 45-degree inflow (right)

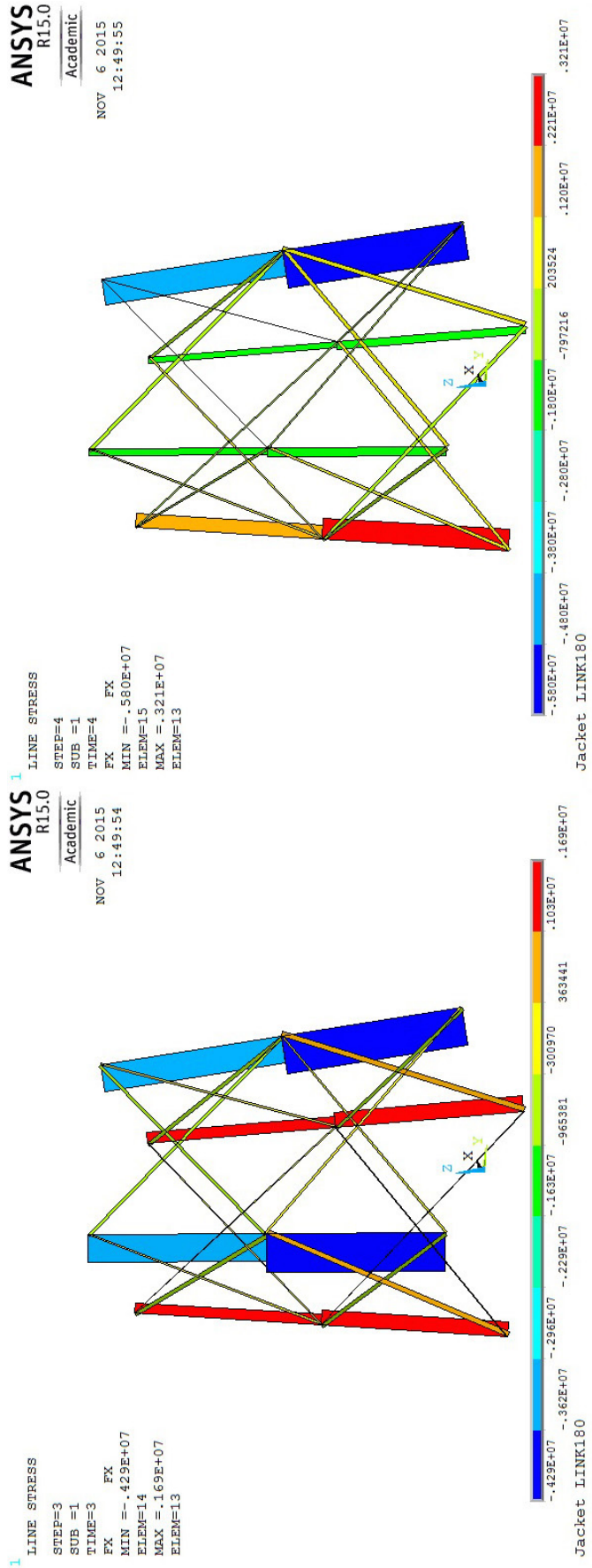

Appendix B. 2 - Ansys member loads for Princes Amalia farm DLC 2.
0-degree inflow (left) and 45-degree inflow (right)

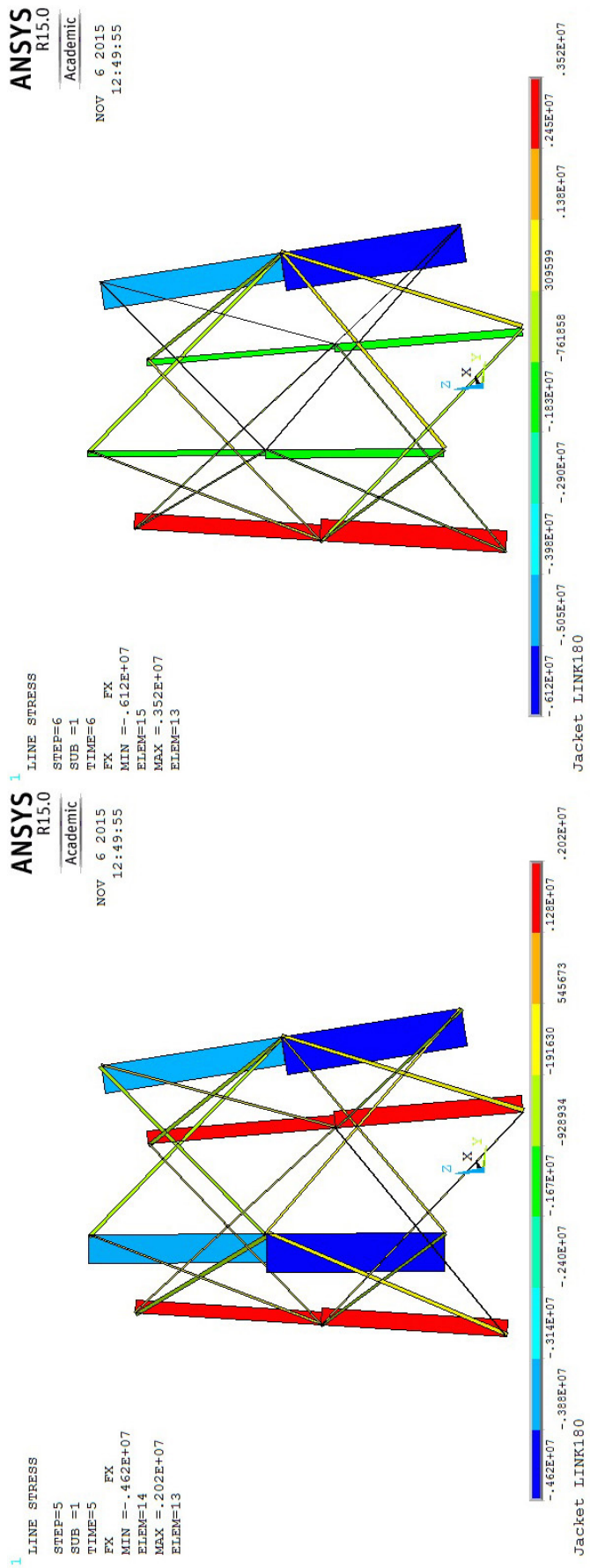

Appendix B. 3 - Ansys member loads for Princes Amalia farm DLC 3.
0-degree inflow (left) and 45-degree inflow (right)

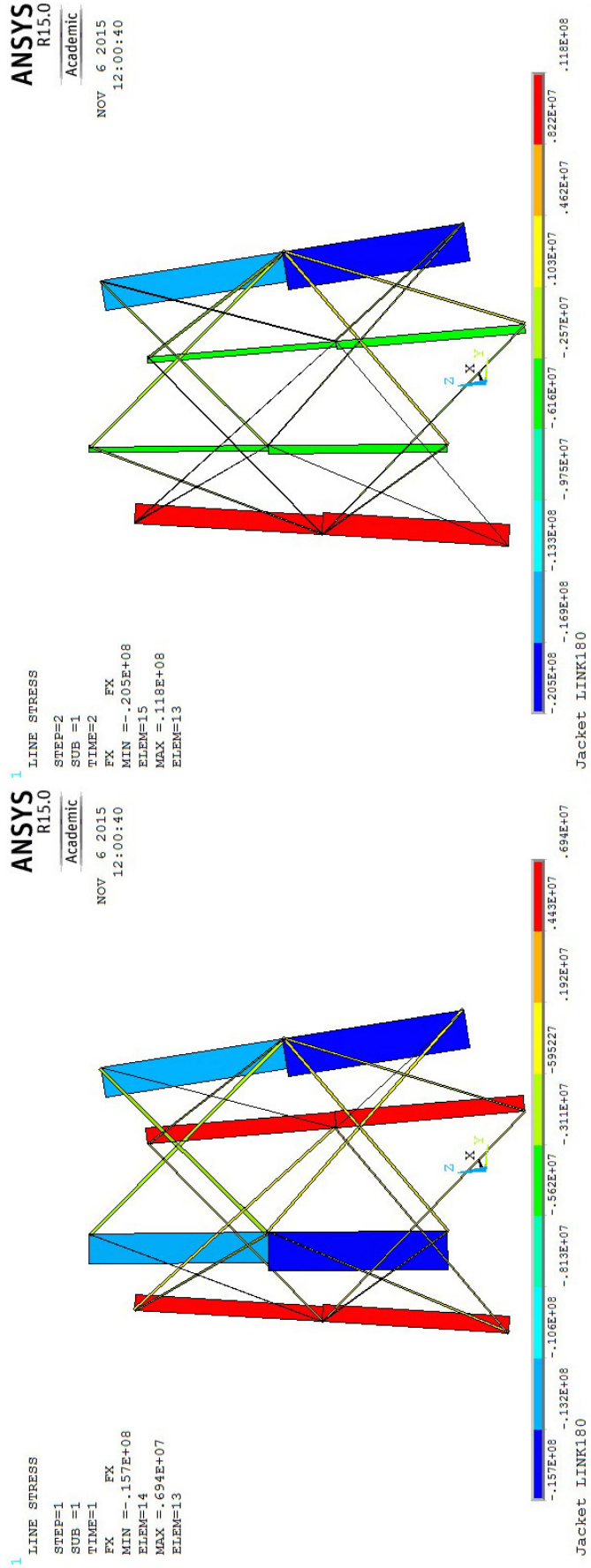

Appendix B. 4 - Ansys member loads for Alpha Ventus farm DLC 1. 0-degree inflow (left) and 45-degree inflow (right)

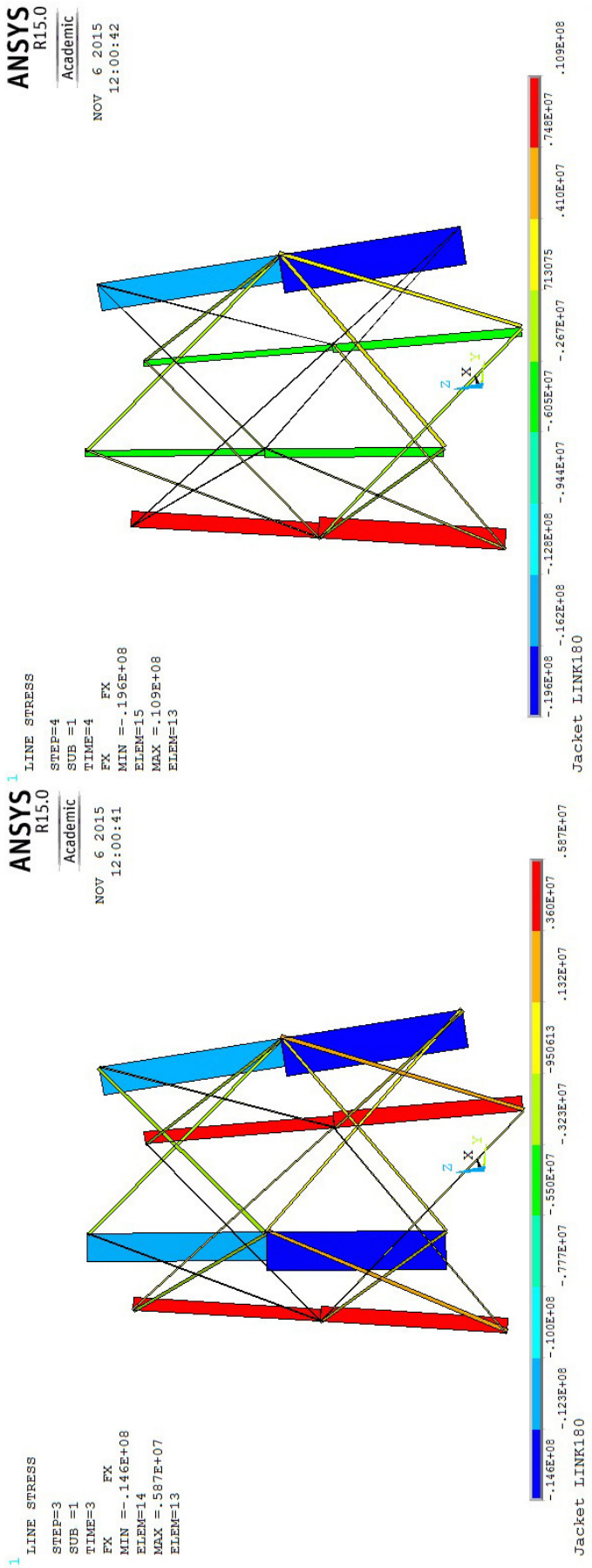

Appendix B. 5 - Ansys member loads for Alpha Ventus farm DLC 2. 0-degree inflow (left) and 45-degree inflow (right)

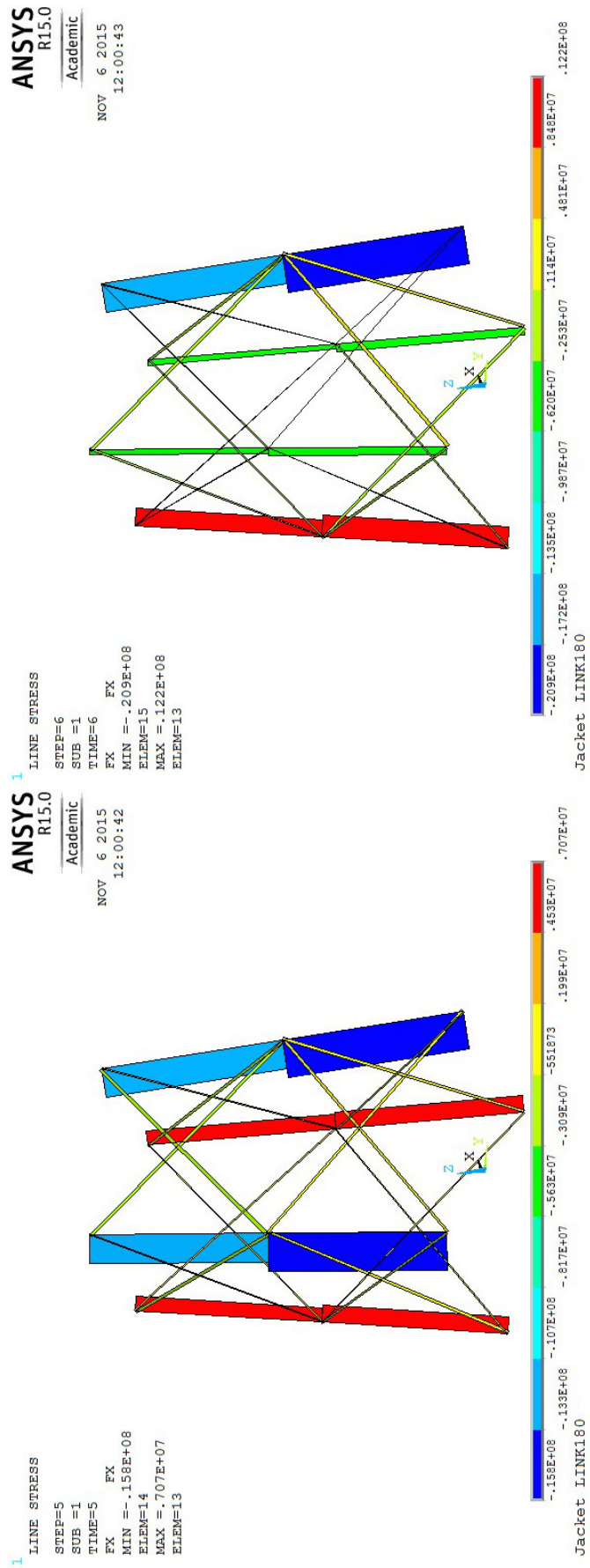

Appendix B. 6 - Ansys member loads for Alpha Ventus farm DLC 3. 0-degree inflow (left) and 45-degree inflow (right)

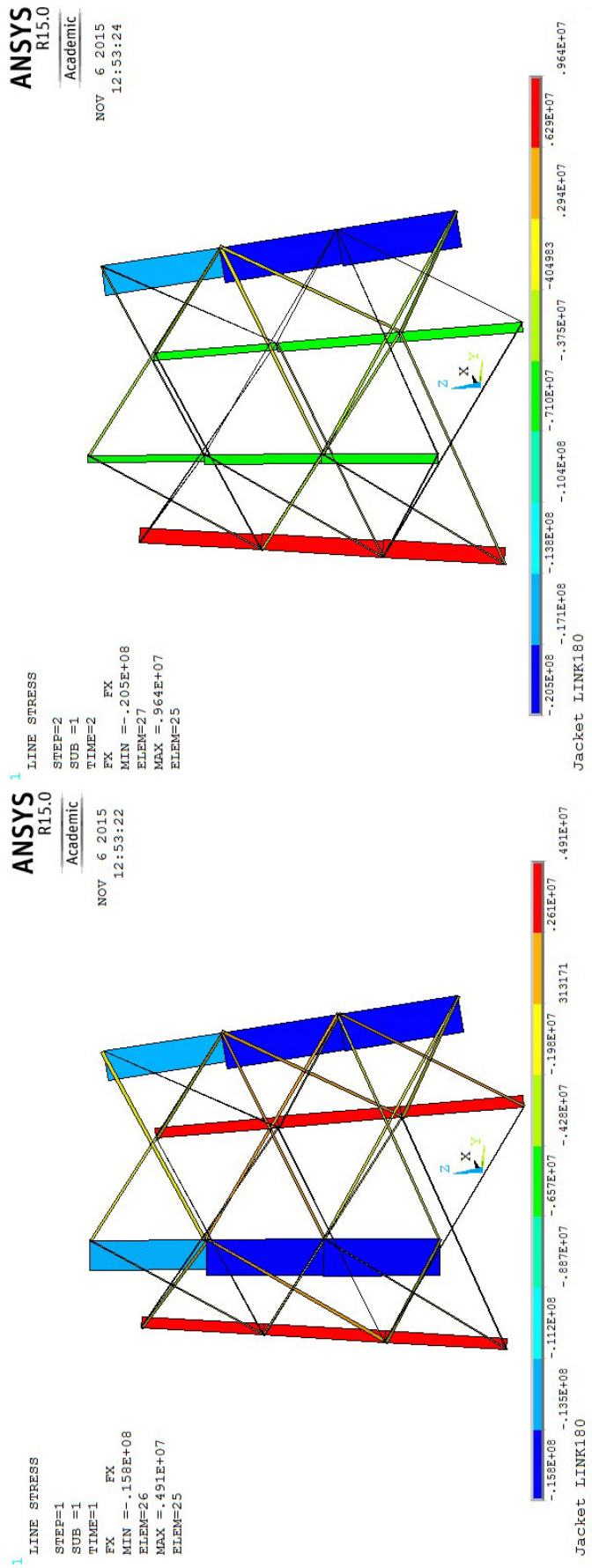

Appendix B. 7 - Ansys member loads for SJOEMF DLC 1. 0-degree inflow (left) and 45-degree inflow (right)

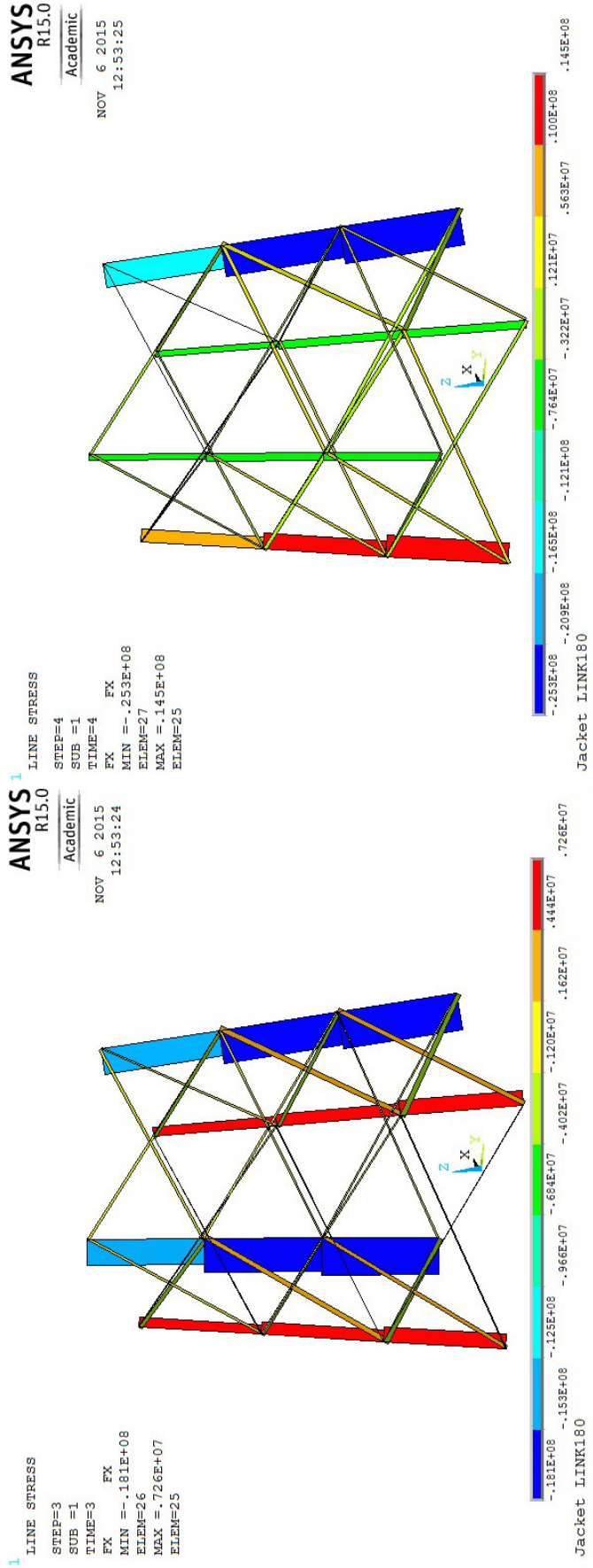

Appendix B. 8 - Ansys member loads for SJOEMF DLC 2. 0-degree inflow (left) and 45-degree inflow (right)

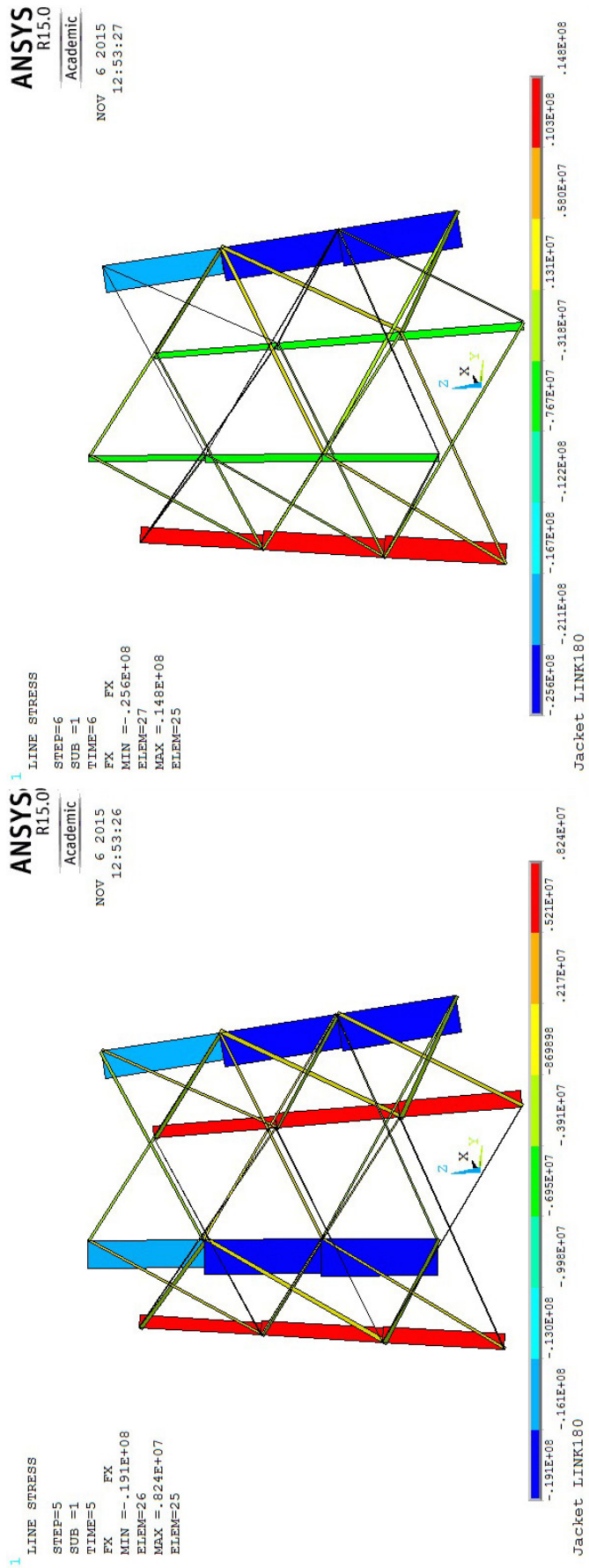

Appendix B. 9 - Ansys member loads for SJOEMF DLC 3. 0-degree inflow (left) and 45-degree inflow (right)

Bay	Member	Location			Load			
		Load case	Angle	Side	Direction	Model (N)	Ansys (N)	Diff (%)
1	Leg	1	45 R	R	Comp	6.25E+06	5.84E+06	6.93
1	Leg	1	45 L	L	Tensile	4.24E+06	3.98E+06	6.53
1	Brace	1	45 R	L	Comp	5.52E+05	5.51E+05	0.15
1	Brace	1	45 L	R	Tensile	3.32E+05	3.31E+05	0.15
2	Leg	1	45 R	R	Comp	8.19E+06	7.41E+06	10.53
2	Leg	1	45 L	L	Tensile	5.31E+06	4.82E+06	10.18
2	Brace	2	45 L	L	Comp	5.62E+05	4.68E+05	20.02
2	Brace	2	45 R	R	Tensile	7.19E+05	6.26E+05	14.90
							Average error	8.60

Appendix B. 10 – Princes Amalia maximum load comparison SJOEM and Ansys

Bay	Member	Location			Load			
		Load case	Angle	Side	Direction	Model (N)	Ansys (N)	Diff (%)
1	Leg	1	45 R	R	Comp	1.78E+07	1.66E+07	7.29
1	Leg	1	45 L	L	Tensile	1.10E+07	1.03E+07	6.89
1	Brace	3	45 R	L	Comp	1.63E+06	1.62E+06	0.17
1	Brace	3	45 L	R	Tensile	8.71E+05	8.70E+05	0.15
2	Leg	3	45 R	R	Comp	2.30E+07	2.09E+07	10.24
2	Leg	3	45 L	L	Tensile	1.33E+07	1.22E+07	9.36
2	Brace	2	45 L	L	Comp	1.52E+06	1.27E+06	20.25
2	Brace	2	45 R	R	Tensile	2.07E+06	1.82E+06	14.03
							Average error	8.47

Appendix B. 11 - Alpha Ventus maximum load comparison SJOEM and Ansys

Bay	Member	Location			Load			
		Load case	Angle	Side	Direction	Model (N)	Ansys (N)	Diff (%)
1	Leg	3	45 R	R	Comp	1.91E+07	1.84E+07	3.99
1	Leg	3	45 L	L	Tensile	1.08E+07	1.04E+07	3.66
1	Brace	3	45 R	L	Comp	2.08E+06	2.08E+06	0.08
1	Brace	3	45 L	R	Tensile	1.32E+06	1.32E+06	0.08
2	Leg	3	45 R	R	Comp	2.48E+07	2.34E+07	6.10
2	Leg	3	45 L	L	Tensile	1.36E+07	1.29E+07	5.40
2	Brace	2	45 L	L	Comp	2.12E+06	1.89E+06	11.90
2	Brace	2	45 R	R	Tensile	2.70E+06	2.47E+06	9.06
3	Leg	3	45 R	R	Comp	2.79E+07	2.56E+07	8.81
3	Leg	3	45 L	L	Tensile	1.59E+07	1.48E+07	7.55
3	Brace	2	45 R	L	Comp	3.67E+06	2.88E+06	27.55
3	Brace	2	45 L	R	Tensile	3.02E+06	2.22E+06	35.70
							Average error	9.96

Appendix B. 12 - SJOEMF maximum load comparison SJOEM and Ansys

DLC	Truss axial	Beam axial	Beam Mises	Diff (%)
1	1.95E+08	1.94E+08	2.00E+08	3.0
2	1.53E+08	1.52E+08	1.67E+08	9.0
3	1.61E+08	1.60E+08	1.74E+08	8.0

Appendix B. 13 - Prinses Amalia maximal stresses

DLC	Truss axial	Beam axial	Beam Mises	Diff (%)
1	2.33E+08	2.33E+08	2.53E+08	7.9
2	2.13E+08	2.12E+08	2.34E+08	9.4
3	2.27E+08	2.26E+08	2.47E+08	8.5

Appendix B. 14 - Alpha Ventus maximal stresses

DLC	Truss axial	Beam axial	Beam Mises	Diff (%)
1	2.10E+08	2.10E+08	2.20E+08	4.5
2	2.27E+08	2.27E+08	2.37E+08	4.2
3	2.40E+08	2.41E+08	2.51E+08	4.0

Appendix B. 15 – SJOEMF maximal stresses

RNA Loads Princes Amalia						
DLC	**Fx (N)**	**Fy (N)**	**Fz (N)**	**Mx (Nm)**	**My (Nm)**	**Mz (Nm)**
1	1792208	0	2296864	0	23896109	0
2	833778	0	2296864	0	11117040	0
3	1008871	0	2296864	0	13451619	0

Appendix B. 16 - RNA loads sample set 1

RNA Loads Alpha Ventus						
DLC	**Fx (N)**	**Fy (N)**	**Fz (N)**	**Mx (Nm)**	**My (Nm)**	**Mz (Nm)**
1	3833365	0	7834266	0	80500673	0
2	2472732	0	7834266	0	51927389	0
3	2992006	0	7834266	0	62832140	0

Appendix B. 17 - RNA loads sample set 2

RNA Loads SJOEMF						
DLC	**Fx (N)**	**Fy (N)**	**Fz (N)**	**Mx (Nm)**	**My (Nm)**	**Mz (Nm)**
1	4879286	0	6409854	0	125235031	0
2	4134923	0	6409854	0	106129706	0
3	5003257	0	6409854	0	128416944	0

Appendix B. 18 - RNA loads sample set 3

Maximum blade deflection (m)	
Princes Amalia	3.2
Alpha Ventus	7.9
SJOEMF	11.9

Appendix B. 19 - Blade deflection

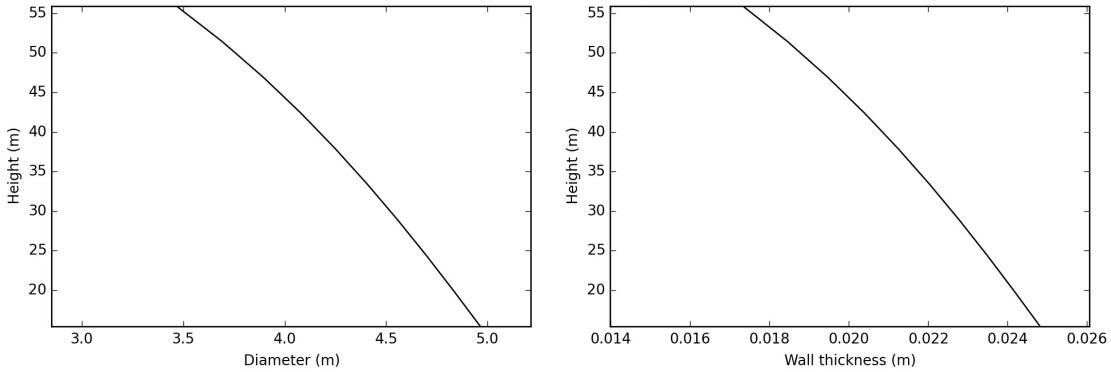

Appendix B. 20 - Princess Amalia tower geometry

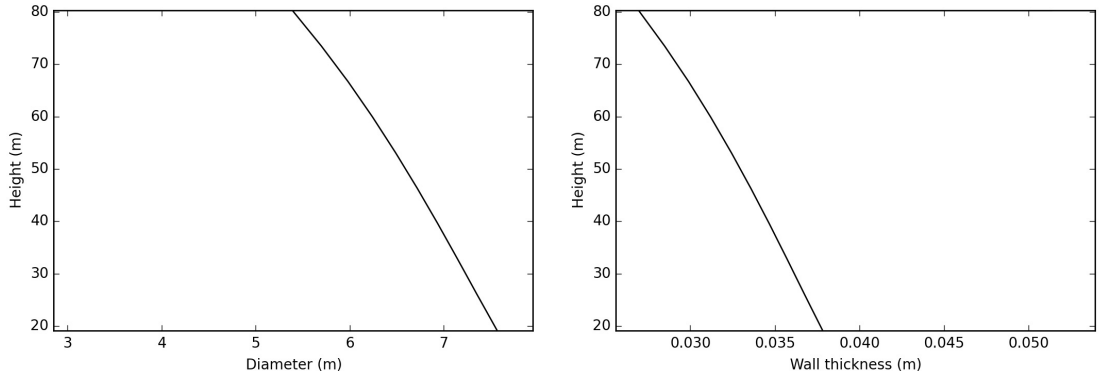

Appendix B. 21 - Alpha Ventus tower geometry

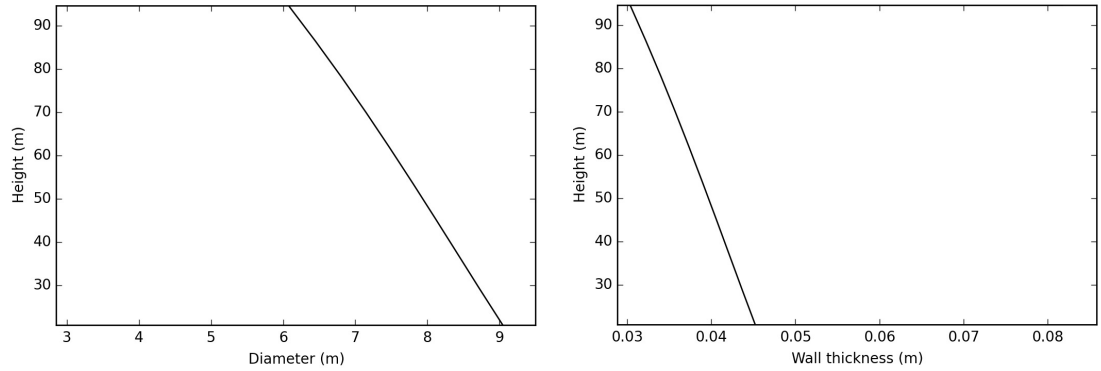

Appendix B. 22 - SJOEMF tower geometry

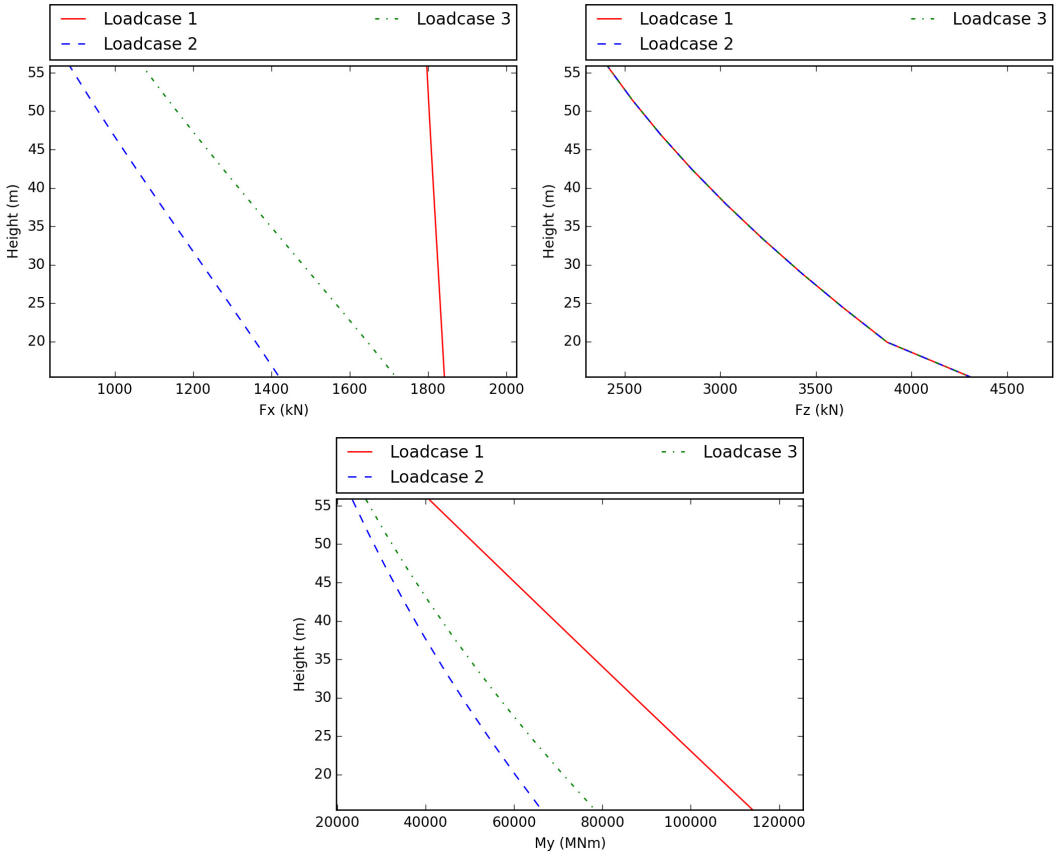

Appendix B. 23 - Princes Amalia tower loads for DLC 1 to 3

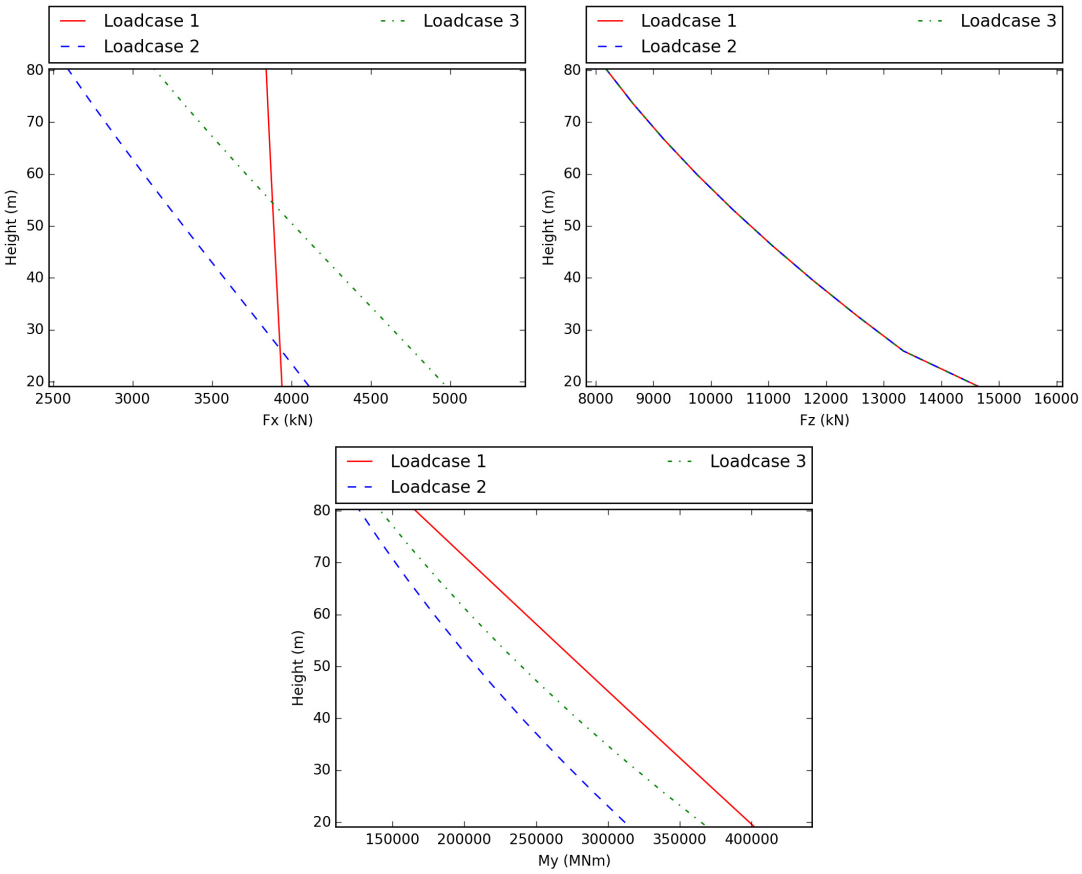

Appendix B. 24 - Alpha Ventus tower loads for DLC 1 to 3

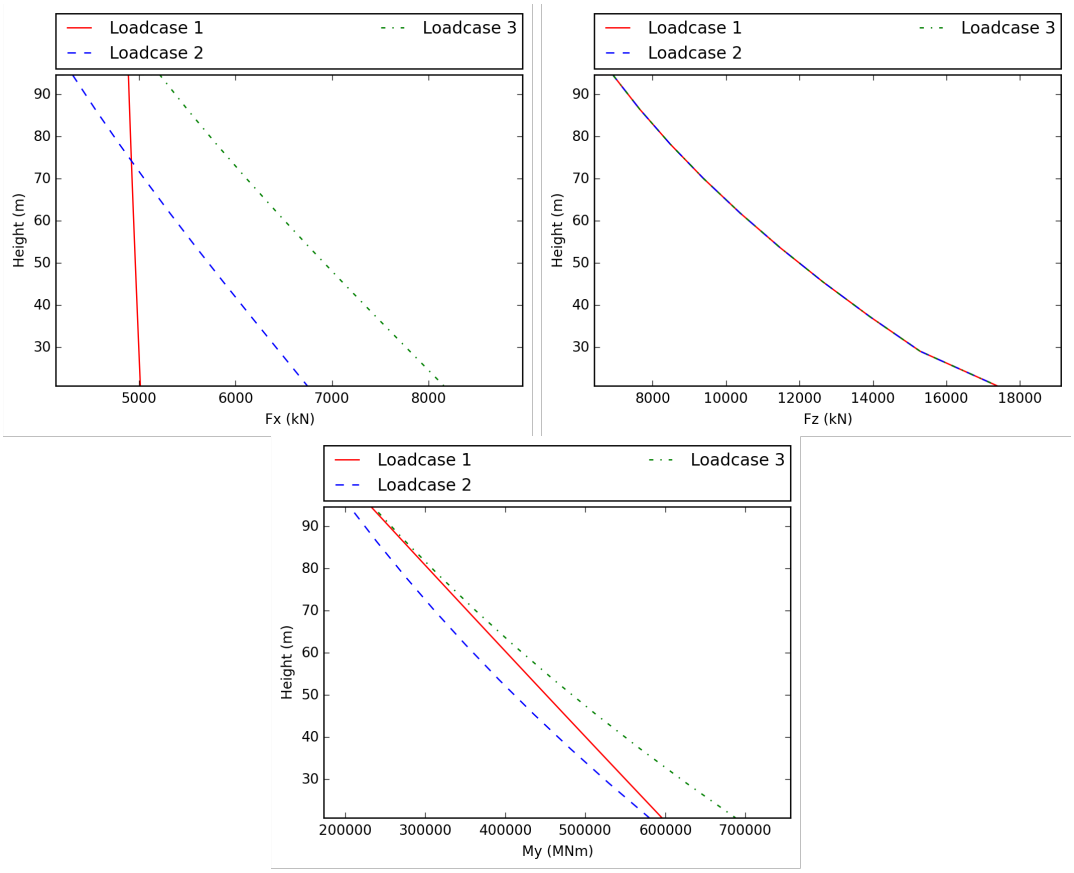

Appendix B. 25 - SJOEMF tower loads for DLC 1 to 3

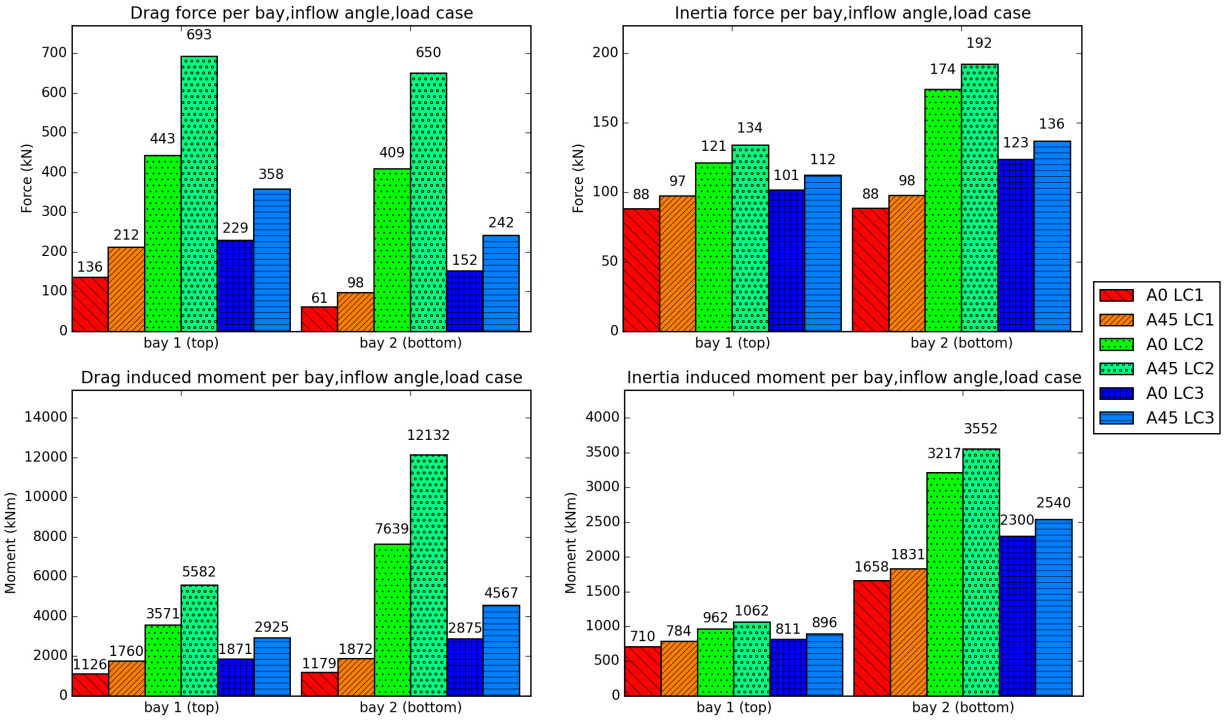

Appendix B. 26 - Princes Amalia jacket external loads for DLC 1 to 3

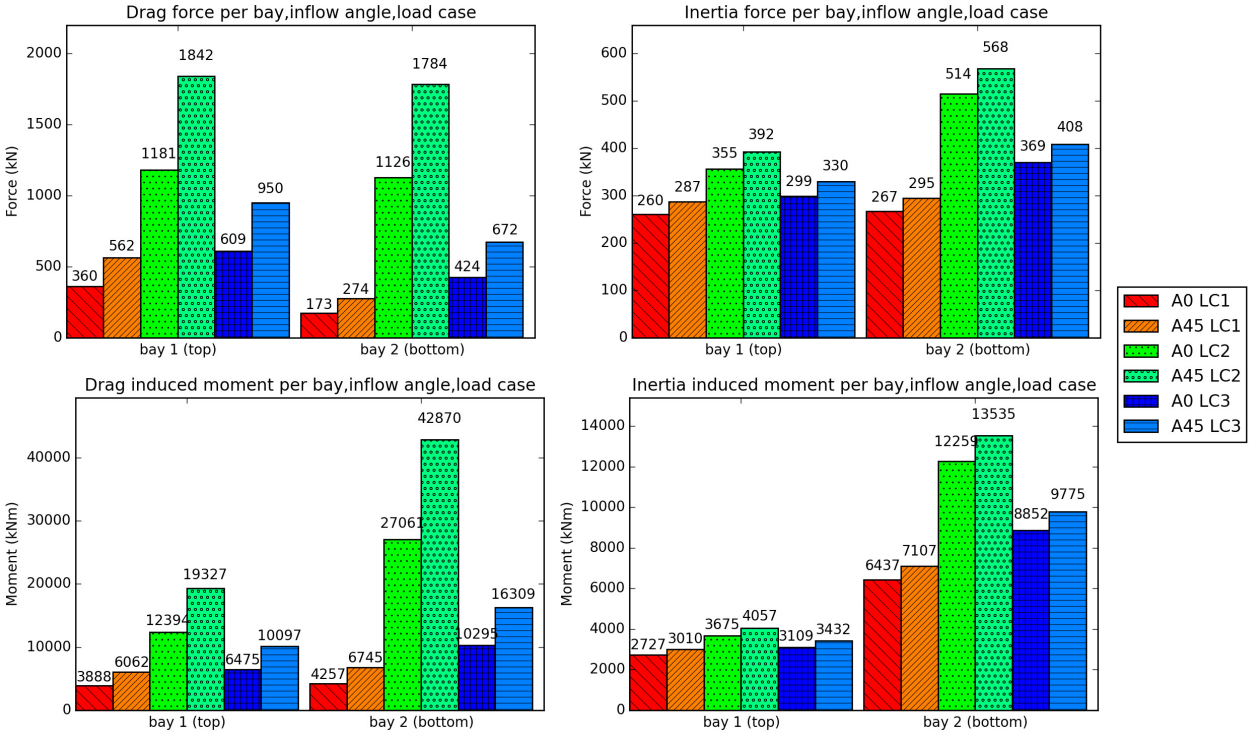

Appendix B. 27 - Alpha Ventus jacket external loads for DLC 1 to 3

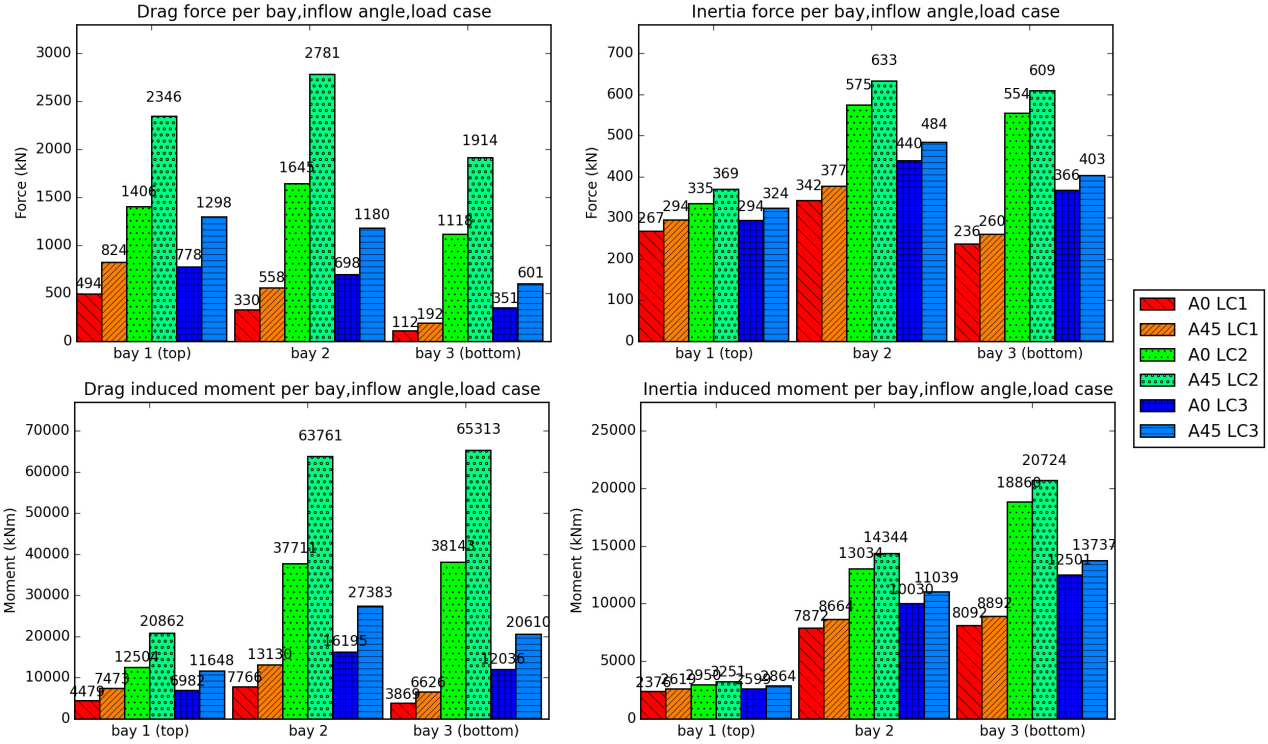

Appendix B. 28 - SJOEMF jacket external loads for DLC 1 to 3

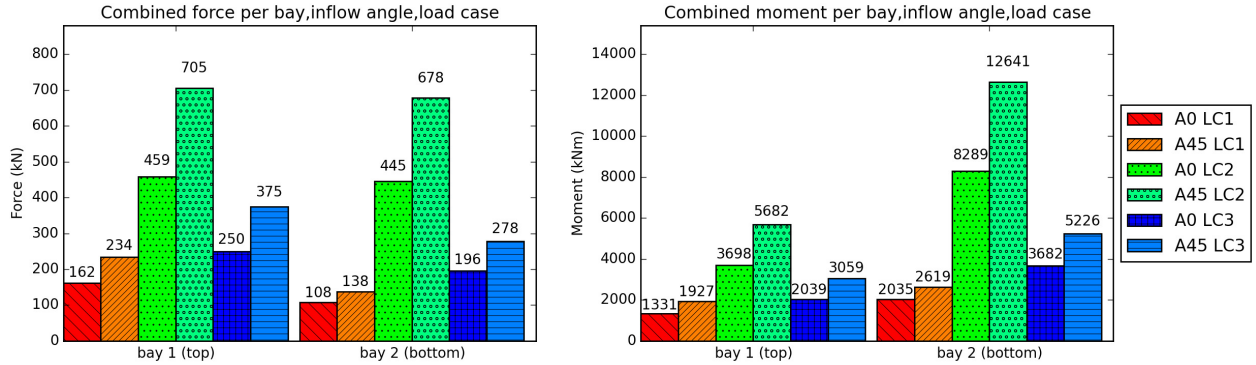

Appendix B. 29 - Princes Amalia combined wave loads for DLC 1 to 3

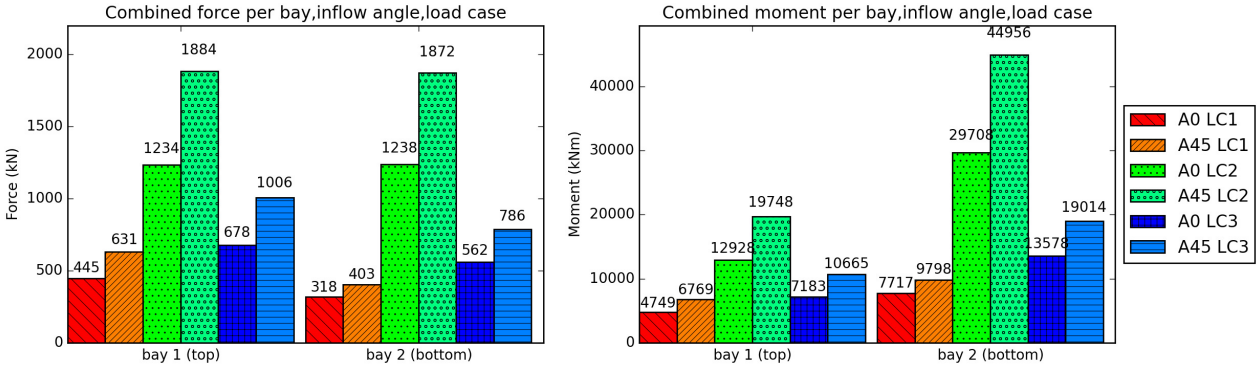

Appendix B. 30 - Alpha Ventus combined wave loads for DLC 1 to 3

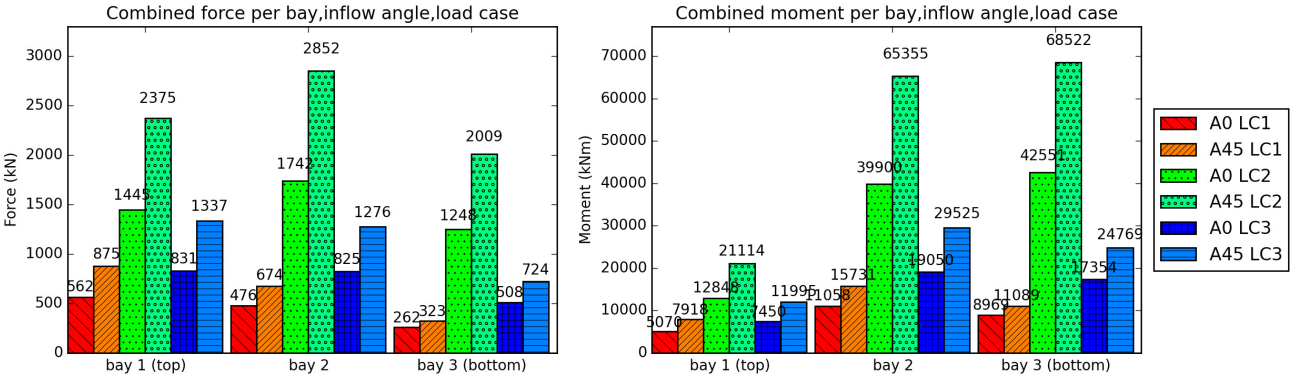

Appendix B. 31 - SJOEMF combined wave loads for DLC 1 to 3

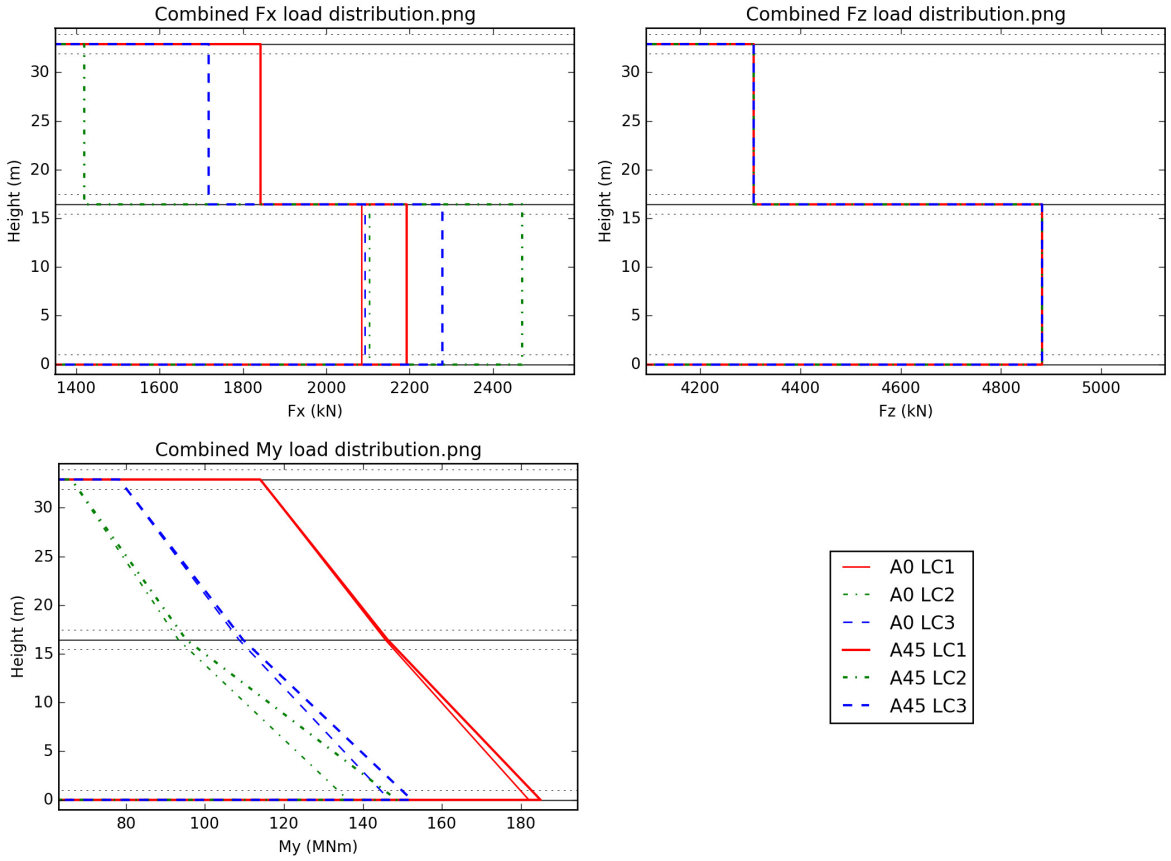

Appendix B. 32 - Princes Amalia jacket section loads for DLC 1 to 3

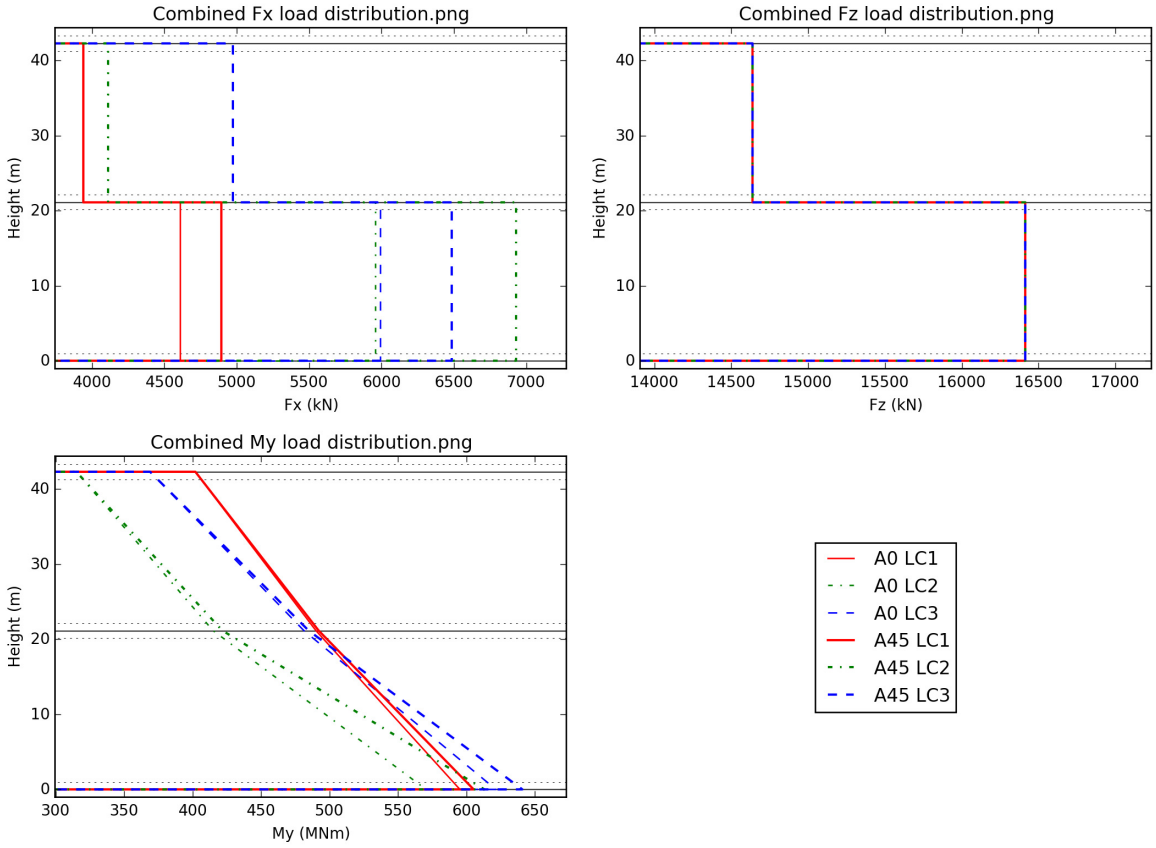

Appendix B. 33 - Alpha Ventus jacket section loads for DLC 1 to 3

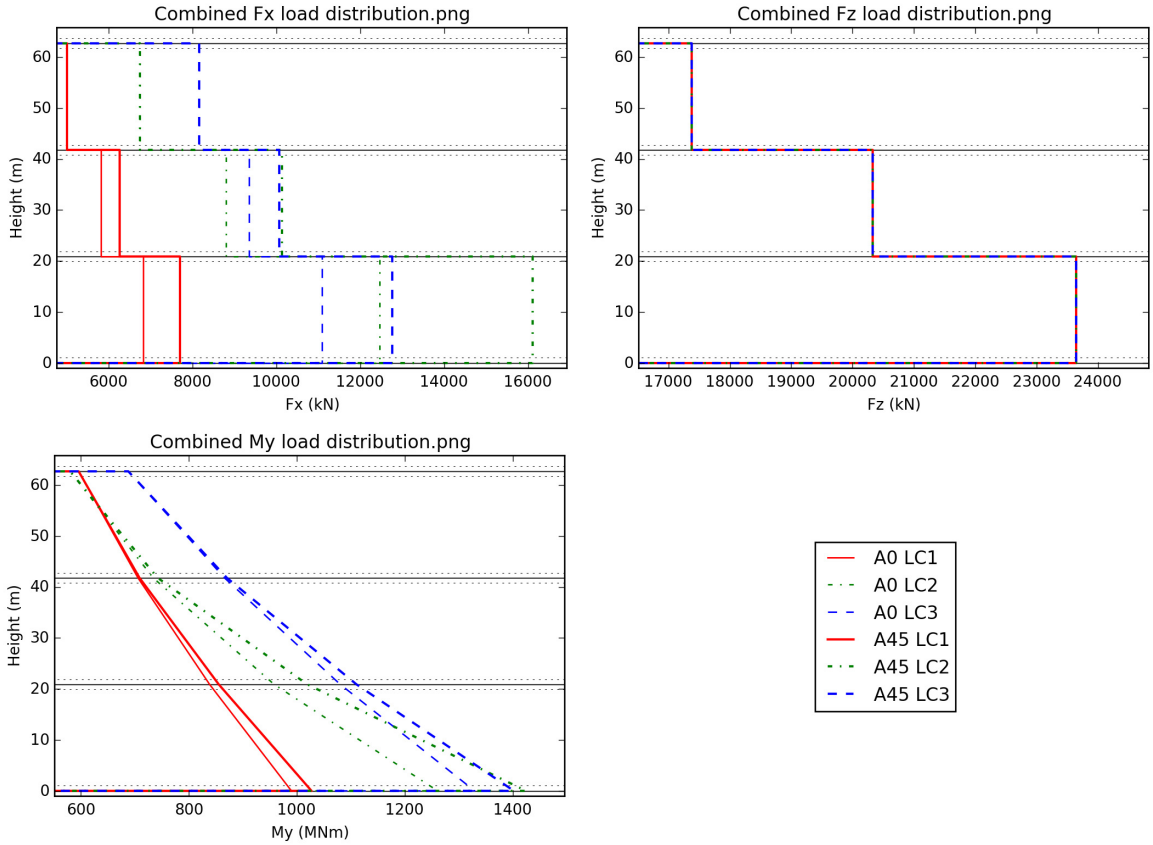

Appendix B. 34 - SJOEMF jacket section loads for DLC 1 to 3

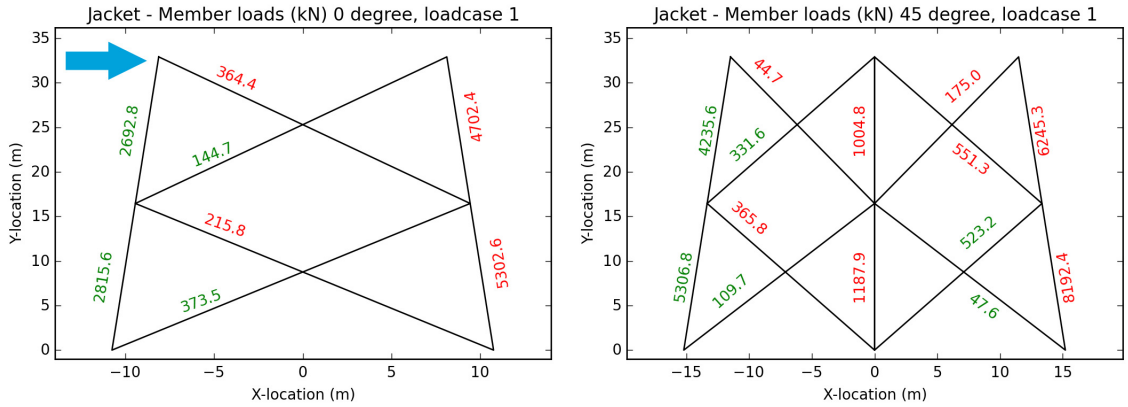

Appendix B. 35 - Princes Amalia jacket member loads for DLC 1

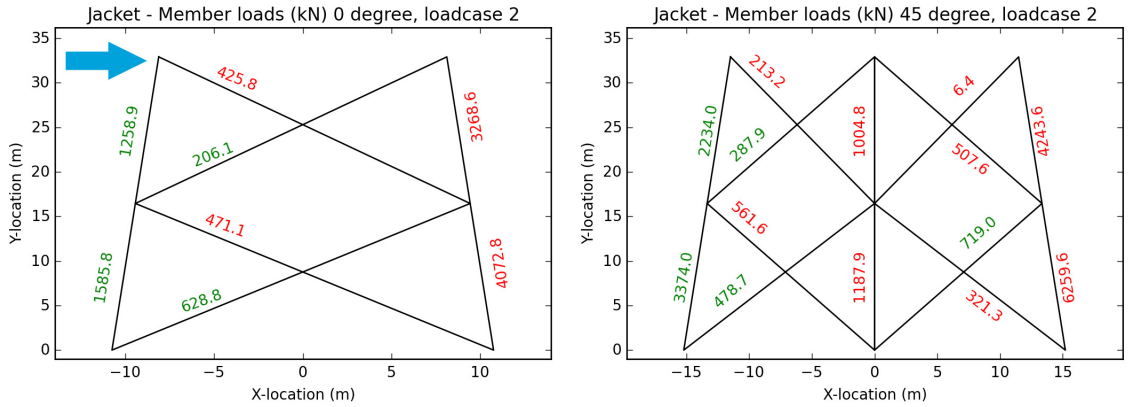

Appendix B. 36 - Princes Amalia jacket member loads for DLC 2

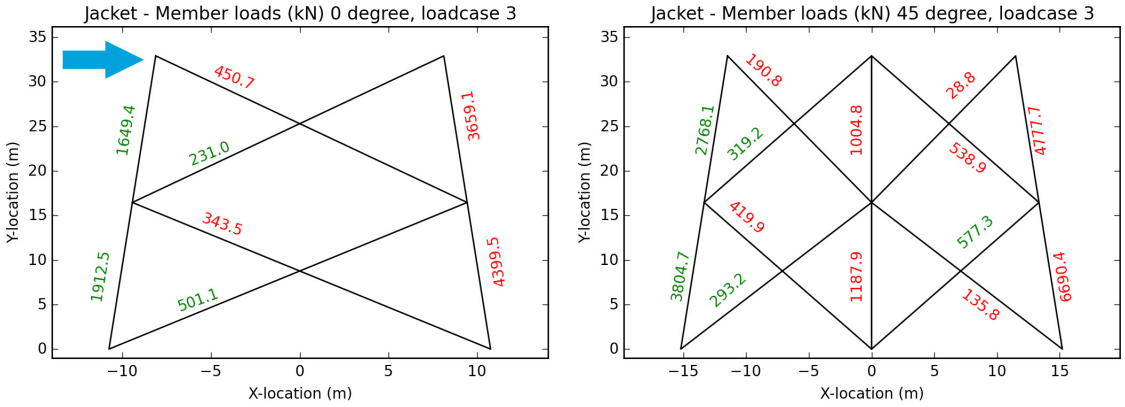

Appendix B. 37 - Princes Amalia jacket member loads for DLC 3

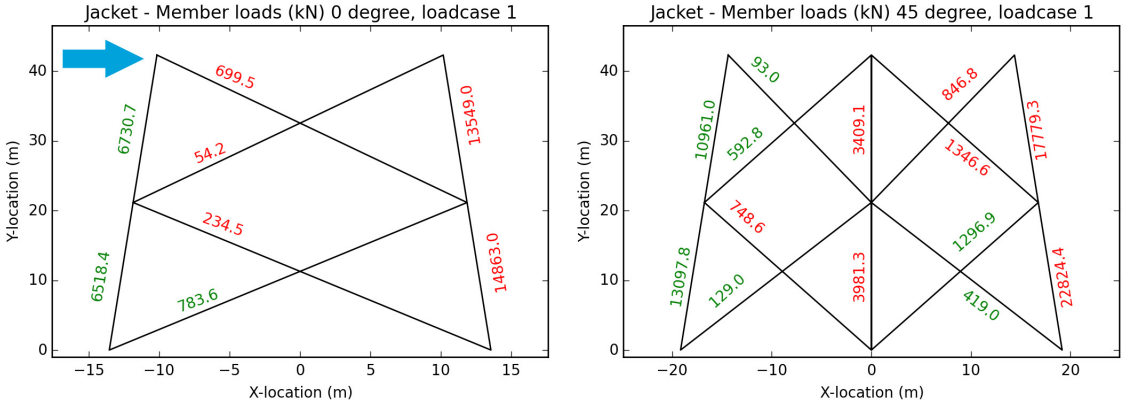

Appendix B. 38 - Alpha Ventus jacket member loads for DLC 1

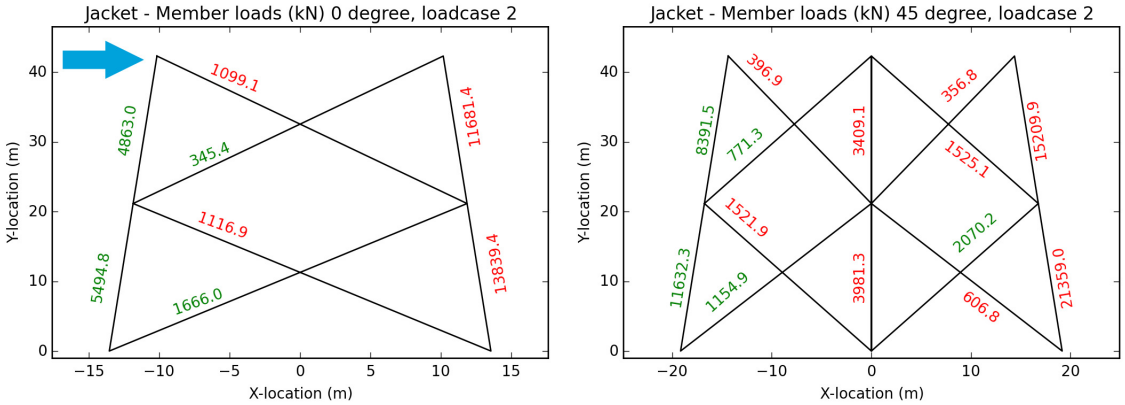

Appendix B. 39 - Alpha Ventus jacket member loads for DLC 2

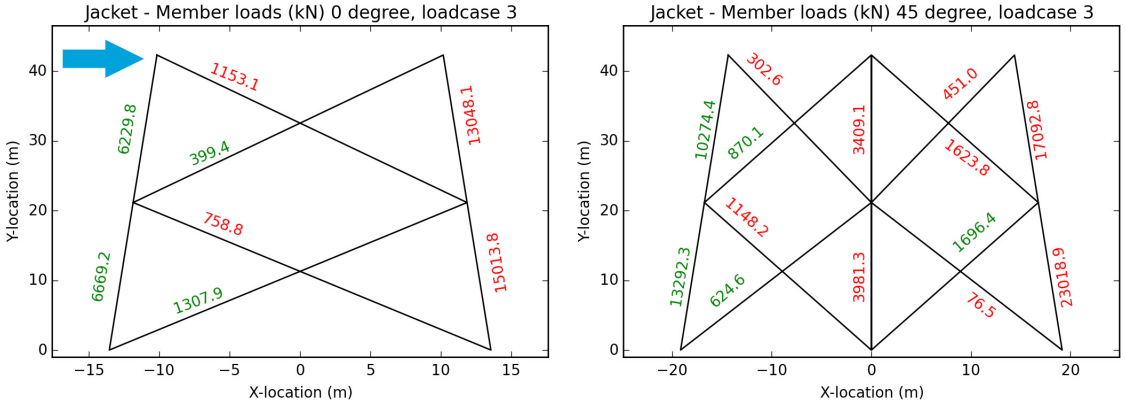

Appendix B. 40 - Alpha Ventus jacket member loads for DLC 3

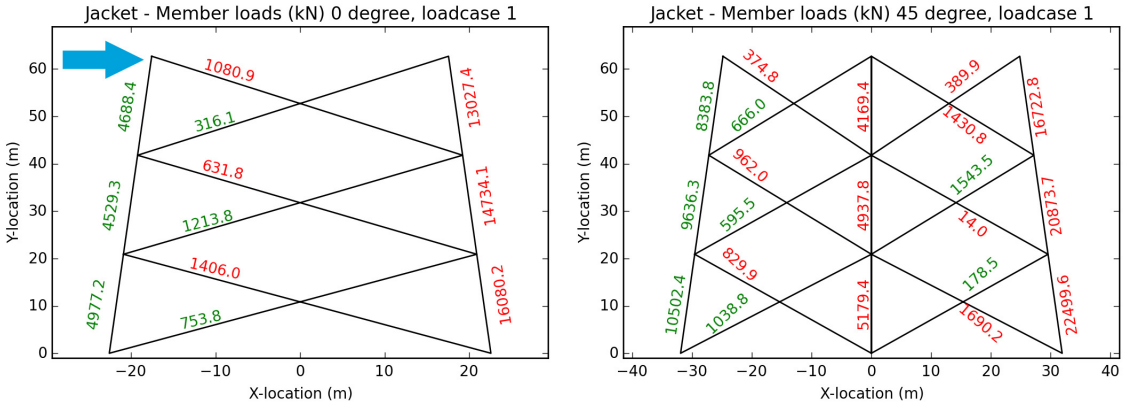

Appendix B. 41 - SJOEMF jacket member loads for DLC 1

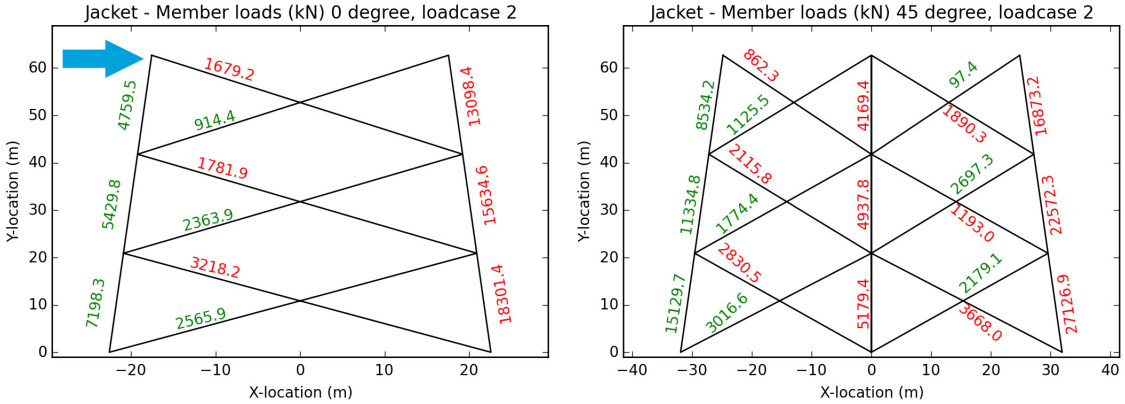

Appendix B. 42 - SJOEMF jacket member loads for DLC 2

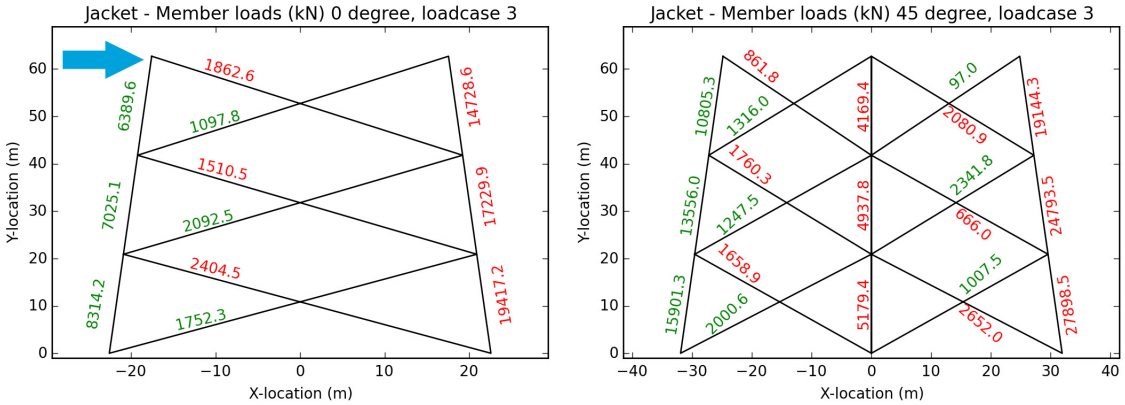

Appendix B. 43 - SJOEMF jacket member loads for DLC 3

Bay	Member	Location			Load	
		Load case	Angle	Side	Direction	Size (N)
1	Leg	1	45 right	right	Compressive	6.25E+06
1	Leg	1	45 left	left	Tensile	4.24E+06
1	Brace	1	45 right	left	Compressive	5.51E+05
1	Brace	1	45 left	right	Tensile	3.32E+05
2	Leg	1	45 right	right	Compressive	8.19E+06
2	Leg	1	45 left	left	Tensile	5.31E+06
2	Brace	2	45 left	left	Compressive	5.62E+05
2	Brace	2	45 right	right	Tensile	7.19E+05

Appendix B. 44 - Princes Amalia jacket maximum member loads per bay

Bay	Member	Location			Load	
		Load case	Angle	Side	Direction	Size (N)
1	Leg	1	45 right	right	Compressive	1.78E+07
1	Leg	1	45 left	left	Tensile	1.10E+07
1	Brace	3	45 right	left	Compressive	1.62E+06
1	Brace	3	45 left	right	Tensile	8.70E+05
2	Leg	3	45 right	right	Compressive	2.30E+07
2	Leg	3	45 left	left	Tensile	1.33E+07
2	Brace	2	45 left	left	Compressive	1.52E+06
2	Brace	2	45 right	right	Tensile	2.07E+06

Appendix B. 45 - Alpha Ventus jacket maximum member loads per bay

Bay	Member	Location			Load	
		Load case	Angle	Side	Direction	Size (N)
1	Leg	3	45 right	right	Compressive	1.91E+07
1	Leg	3	45 left	left	Tensile	1.08E+07
1	Brace	3	45 right	left	Compressive	2.08E+06
1	Brace	3	45 left	right	Tensile	1.32E+06
2	Leg	3	45 right	right	Compressive	2.48E+07
2	Leg	3	45 left	left	Tensile	1.36E+07
2	Brace	2	45 left	left	Compressive	2.12E+06
2	Brace	2	45 right	right	Tensile	2.70E+06
3	Leg	3	45 right	right	Compressive	2.79E+07
3	Leg	3	45 left	left	Tensile	1.59E+07
3	Brace	2	45 right	left	Compressive	3.67E+06
3	Brace	2	45 left	right	Tensile	3.02E+06

Appendix B. 46 - SJOEMF jacket maximum member loads per bay

Bay	D_{leg} (m)	wt_{leg} (m)	D_{brace} (m)	wt_{brace} (m)	Bay weight (kN)
1	0.51	0.02	0.31	0.012	451
2	0.56	0.022	0.34	0.013	590

Appendix B. 47 - Princes Amalia member dimensions

Bay	D_{leg} (m)	wt_{leg} (m)	D_{brace} (m)	wt_{brace} (m)	Bay weight (kN)
1	0.77	0.031	0.46	0.018	1296
2	0.85	0.036	0.51	0.02	1765

Appendix B. 48 - Alpha Ventus member dimensions

Bay	D_{leg} (m)	wt_{leg} (m)	D_{brace} (m)	wt_{brace} (m)	Bay weight (kN)
1	0.78	0.033	0.47	0.031	2426
2	0.86	0.036	0.52	0.029	2842
3	0.94	0.037	0.57	0.051	4884

Appendix B. 49 - SJOEMF member dimensions

Bay	Δ wtleg (m)	Δ wtbrace (m)	Lleg (m)	Lbr (m)	SCFl	SCFbr
1	0.061	0	0.9	0	5.87	3.85
2	0.067	0	0.9	0	5.41	3.48

Appendix B. 50 - Princes Amalia sleeve dimensions

Bay	Δ wtleg (m)	Δ wtbrace (m)	Lleg (m)	Lbr (m)	SCFl	SCFbr
1	0.12	0	1.1	0	5.89	3.88
2	0.11	0	1.1	0	4.74	3.21

Appendix B. 51 - Alpha Ventus sleeve dimensions

Bay	Δ wtleg (m)	Δ wtbrace (m)	Lleg (m)	Lbr (m)	SCFl	SCFbr
1	0.12	0	1.2	0	6.04	3.18
2	0.09	0	1.2	0	4.15	2.5
3	0.17	0	1.2	0	6.81	3.2

Appendix B. 52 - SJOEMF sleeve dimensions

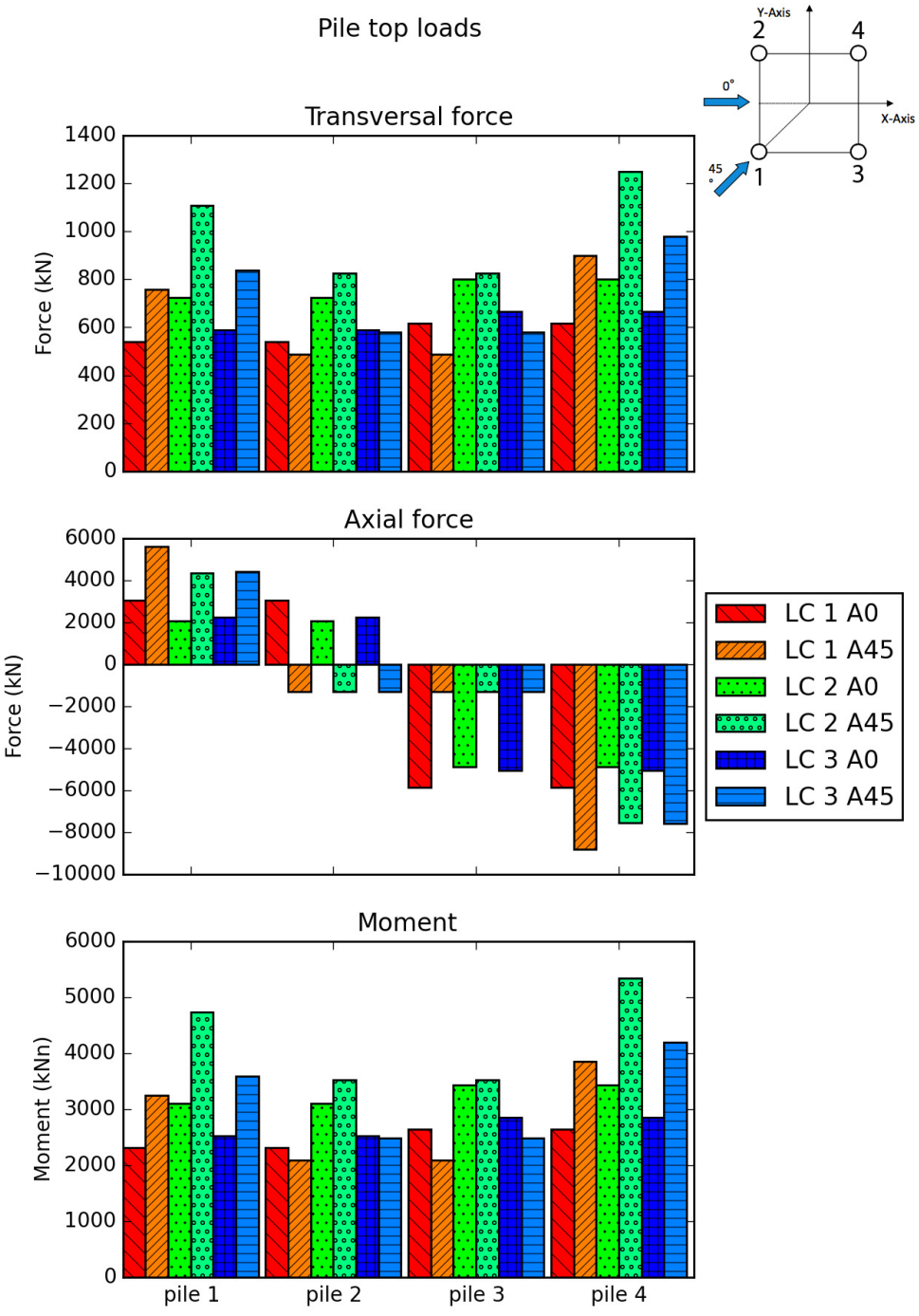

Appendix B. 53 - Princes Amalia pile top loads

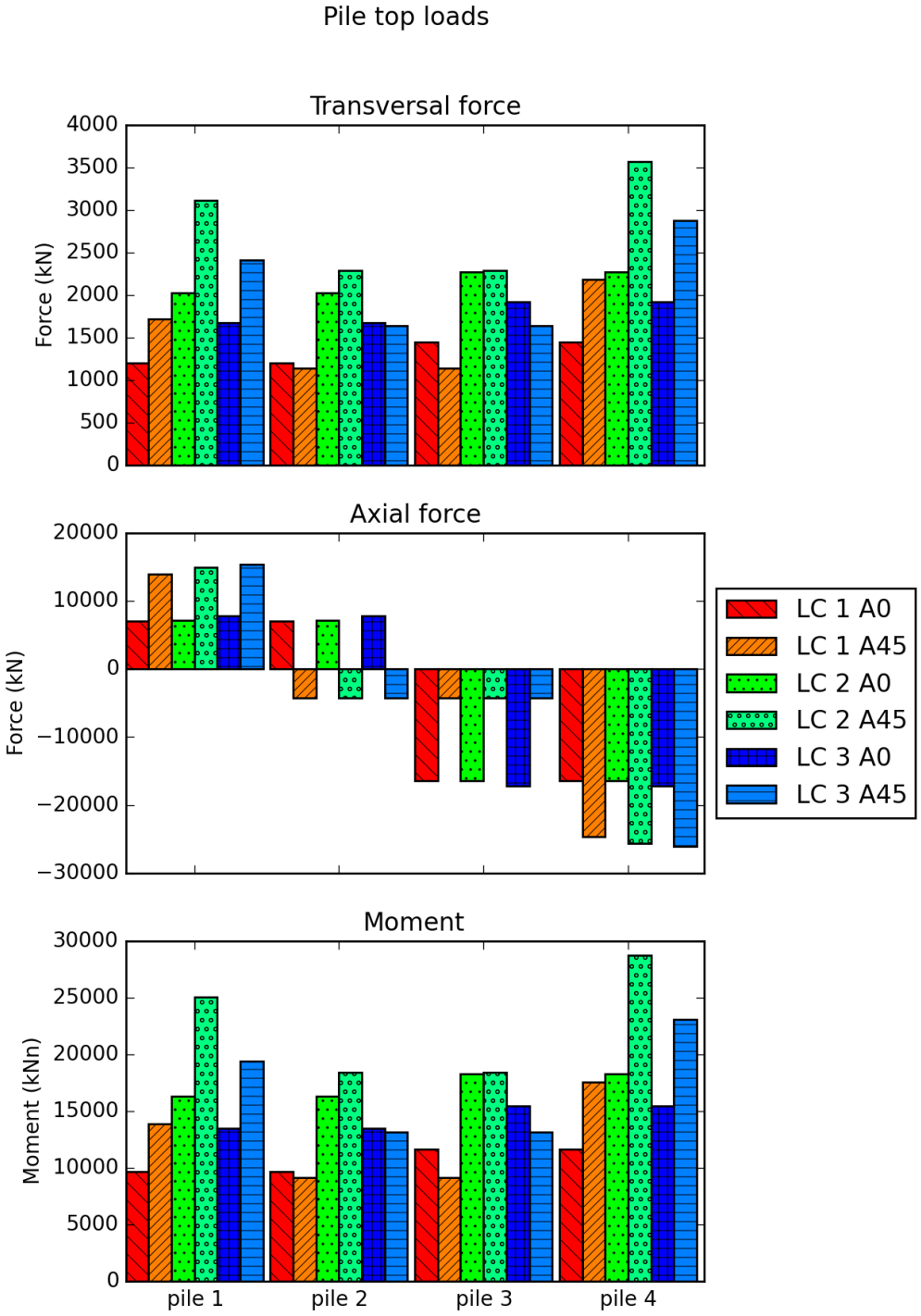

Appendix B. 54 - Alpha Ventus pile top loads

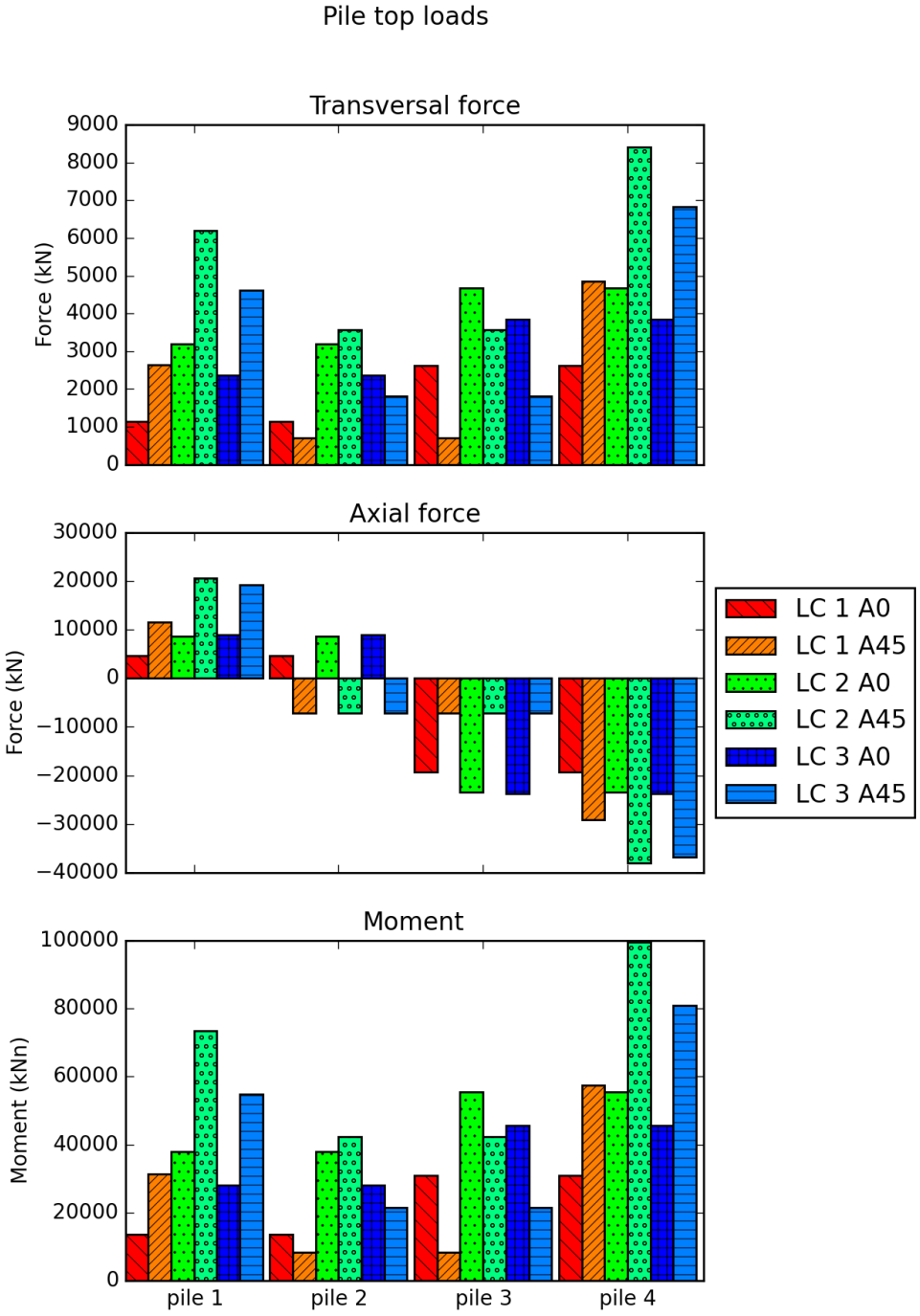

Appendix B. 55 - SJOEMF pile top loads

D_{pile} (m)	wt_{pile} (m)	L_{pile} (m)	$d_{e\ pile}$ (m)	M_{pile} (kN)
1.43	0.02	15.74	4.3	111

Appendix B. 56 - Princes Amalia pile dimensions

D_{pile} (m)	wt_{pile} (m)	L_{pile} (m)	$d_{e\ pile}$ (m)	M_{pile} (kN)
2.69	0.033	12.86	8.06	275

Appendix B. 57 - Alpha Ventus pile dimensions

D_{pile} (m)	wt_{pile} (m)	L_{pile} (m)	$d_{e\ pile}$ (m)	M_{pile} (kN)
3.96	0.05	24.34	11.78	1042

Appendix B. 58 - SJOEMF pile dimensions

Appendix C – Load calculations

Appendix C1 – Tower bottom yield stress for Princes Amalia farm DLC 1

$F_x = 1841377\,N$

$F_z = 4307130\,N$

$M_y = 113993873\,Nm$

$D = 4.96\,m$

$wt = 0.025\,m$

$\sigma_{steel} = 2{,}5 \cdot 10^8\,N/m^2$

$$A = \frac{\pi}{4} \cdot (D^2 - (D - 2 \cdot wt)^2) = 0.388\,m^2$$

$$I_y = \frac{\pi}{64} \cdot (D^4 - (D - 2 \cdot wt)^4) = 1.18\,m^4$$

$$\sigma_{yield} = \sqrt{\left(\frac{F_x}{A}\right)^2 + \left(\frac{F_z}{A} + \frac{M_y \cdot D}{2 \cdot I_y}\right)^2} = 2{,}5 \cdot 10^8\,N/m^2$$

$\sigma_{steel} - \sigma_{yield} = 0\,N/m^2 \rightarrow pass$

Appendix C2 – Tower bottom buckling stress for Princes Amalia farm DLC 1 as described in 'Guideline for design of wind turbines' (DNV, 2002) (DNV 2002).

$$\sigma_{ad} = \frac{F_z}{\pi \cdot D \cdot wt} = 1.2 \cdot 10^7\,N/m^2$$

$$\sigma_{bd} = \frac{4 \cdot M_y}{\pi \cdot D^2 \cdot wt} = 2.4 \cdot 10^8\,N/m^2$$

$$\varepsilon_a = \frac{0.83}{\sqrt{1 + 0.01 \cdot \frac{D}{2 \cdot wt}}} = 0.586$$

$$\varepsilon_b = 0.1887 + 0.8113 \cdot \varepsilon_a = 0.665$$

$$\varepsilon = \frac{\varepsilon_a \cdot \sigma_{ad} + \varepsilon_b \cdot \sigma_{bd}}{\sigma_{ad} + \sigma_{bd}} = 0.66$$

$E_d = 2.1 \cdot 10^{11}\,N/m^2$

$\nu = 0.3$

$$\sigma_{el} = \frac{E_d}{\frac{D}{2 \cdot wt} \cdot \sqrt{3 \cdot (1 - \nu^2)}} = 1.3 \cdot 10^8\,N/m^2$$

$$\lambda_a = \sqrt{\frac{\sigma_{steel}}{\varepsilon \cdot \sigma_{el}}} = 0.55$$

$$\sigma_{cr} = (1.5 - 0.913 \cdot \sqrt{\lambda_a}) \cdot \sigma_{steel} = 2.2 \cdot 10^8\,N/m^2$$

$$H = 45\,m$$

$$N_{el} = \frac{\pi^2 \cdot E_d \cdot \pi \cdot D^3 \cdot wt}{32 \cdot H^2} = 3.1 \cdot 10^8\,N$$

$$\lambda_r = \sqrt{\frac{\sigma_{cr}}{\frac{N_{el}}{\pi \cdot D \cdot wt}}} = 0.51$$

$$k = \frac{D}{4} = 1.24\,m$$

$$e = 0.34 \cdot (\lambda_r - 0.2) \cdot k = 0.13$$

$$e = e - \frac{2}{1000} \cdot H = 0.04$$

$$\frac{F_z}{\pi \cdot D \cdot wt} + \frac{N_{el}}{N_{el} - F_z} \cdot \frac{4 \cdot (M_y + F_z \cdot e)}{\pi \cdot D^2 \cdot wt} - \sigma_{cr} = -1.9 \cdot 10^7\,N/m^2 \rightarrow pass$$

Appendix C3 – Maximum yield stress for leg of bottom bay of Princes Amalia farm.

$$F_{max} = 7368648\,N$$

$$D = 0.56\,m$$

$$wt = 0.022\,m$$

$$A = \frac{\pi}{4} \cdot \left(D^2 - \left(D - 2 \cdot wt \right)^2 \right) = 0.037\,m^2$$

$$\sigma_{max} = \frac{F_{max}}{A} = 1.9 \cdot 10^8\,N/m^2$$

$$\sigma_{steel} - \sigma_{max} = 5 \cdot 10^7\,N/m^2 \rightarrow pass$$

Appendix C4 – Global Euler buckling check for leg of bottom bay of Princes Amalia farm according to Vugts (Vugts 2002)

$$L = 17.6\,m$$

$$K_{eff} = 1 \text{ (both sides simply supported)}$$

$$I = 0.0013$$

$$A = 0.037$$

$$R_{gyra} = \sqrt{\frac{I}{A}} = 0.187$$

$$\lambda = K_{eff} \cdot \frac{L}{R_{gyra}} = 94$$

$$\lambda_e = \pi \cdot \sqrt{\frac{E_d}{\sigma_{steel}}} = 93$$

$$\lambda_r = \frac{\lambda}{\lambda_e} = 1.02$$

$$\sigma_{buck} = \frac{\sigma_{steel}}{\lambda_r^2} = 2.4 \cdot 10^8\,N/m^2$$

$$\sigma_{buck} - \sigma_{max} = 5 \cdot 10^7\,N/m^2 \rightarrow pass$$

Appendix C5 – Local buckling constraint for leg of bottom bay of Princes Amalia farm according to GL 6.6.5.6 (GL 2012)

$$l = 17.6m$$

$$r = \frac{D - wt}{2} = 0.269m$$

$$\eta = 1 \text{ (both ends simply supported)}$$

$$C_x = max[1 - \frac{0.4 \cdot \frac{2 \cdot l}{r} \cdot \sqrt{\frac{wt}{r}} - 0.2}{\eta}, 0.6] = 0.6$$

$$wt = \frac{40 \cdot r \cdot \sigma_{steel}}{E_d \cdot C_x} = 0.022m \rightarrow pass$$

Appendix C6 – Stress concentration factors for bottom bay of Princes Amalia farm according to API C.5.3.2 (API 2000)

$$\beta = \frac{D_{brace}}{D_{leg}}$$

$$\gamma = \frac{D_{leg}}{2 \cdot wt_{leg}}$$

$$\tau = \frac{wt_{brace}}{wt_{leg}}$$

$$\zeta = tan(\theta_{brace})$$

$$SCF_{leg} = \tau^{0.9} \cdot \gamma^{0.5} \cdot (0.67 - 1.16 \cdot \beta) \cdot sin(\theta_{brace}) \cdot (1.64 + 0.29 \cdot \beta^{-0.38} \cdot atan(8 \cdot \zeta)$$

$$SCF_{leg} = 7.65$$

$$SCF_{brace} = 1 + SCF_{leg} \cdot (1.97 - 1.57 \cdot \beta^{0.25}) \cdot \tau^{-0.14} \cdot sin(\theta_{brace})^{0.7} + \beta^{1.5 \cdot \gamma^{0.5} \cdot \tau^{-0.14} \cdot sin(\theta_{brace})} \cdot atan(14 \cdot \zeta + 4.2 \cdot \beta)$$

$$SCF_{brace} = 3.4$$

Appendix C7 – Stress in pile 4 for inflow angle of 45 degrees at DLC 2.

$$D_{pile} = 1.37\,m$$

$$wt_{pile} = 0.02m$$

$$L_{pile} = 15.55\,m$$

$$F_{ax} = 6904523N$$

$$F_{tr} = 1171691N$$

$$M_y = 4807795\,Nm$$

$$A = \frac{\pi}{4}\cdot\left(D_{pile}^2 - \left(D_{pile} - 2\cdot wt_{pile}\right)^2\right) = 0.085\,m^2$$

$$I = \frac{\pi}{64}\cdot\left(D_{pile}^4 - \left(D_{pile} - 2\cdot wt_{pile}\right)^4\right) = 0.019\,m^2$$

$$\sigma_{ax} = \frac{F_{ax}}{A} + \frac{D_{pile}\cdot M_y}{2\cdot I} = 2.6\cdot 10^8\,N/m^2$$

$$\sigma_{tr} = \frac{F_{tr}}{A} = 1.4\cdot 10^7\,N/m^2$$

$$\sigma_{tot} = \sqrt{\sigma_{ax}^2 + \sigma_{tr}^2} = 2.5\cdot 10^8\,N/m^2$$

$$\sigma_{steel} - \sigma_{tot} = 0N/m^2 \rightarrow pass$$

Appendix C8 – Pile drive wall thickness for buckling not to occur according to API (API 2000).

$$wt_{piledrive} = 0.00634 + \frac{D_{pile}}{100} = 0.02m$$

$$wt_{pile} = wt_{piledrive} \rightarrow pass$$

Appendix C9 – Pile length to withstand transversal loads according to Blum's theory as used by Zaaijer (Zaaijer 2013)

$$\theta_{soil} = 35\,deg$$

$$\rho_{soil} = 19000kg/m^3$$

$$\theta_{PE} = 0.8$$

$$n = 2$$

$$K_p = \frac{1+\sin(\theta_{soil})}{1-\sin(\theta_{soil})}$$

$$K_a = \frac{1-\sin(\theta_{soil})}{1+\sin(\theta_{soil})}$$

$$\theta_{PE}\cdot n\cdot(K_p - K_a)\cdot\rho_{soil}\cdot D_{pile}\cdot L_{pile}^2 = 6\cdot\left(F_{tr} + \frac{M_y}{L_{pile}}\right) \rightarrow L_{pile} = 8.14m$$

$$L_{pile} = 1.3\cdot L_{pile} = 10.6m \rightarrow pass$$

Appendix C10 – Pile length to withstand axial loads as used by Zaaijer (Zaaijer 2013).

$$K_0 = 0.8$$

$$\delta = \theta_{soil} - 10 = 25\,deg$$

$$F_{outside} = 0.5 \cdot K_0 \cdot \tan(\delta) \cdot \rho_{soil} \cdot \pi \cdot D_{pile}^2 \cdot L_{pile}^2 = 5.0 \cdot 10^6\,N$$

$$F_{inside} = 0.5 \cdot K_0 \cdot \tan(\delta) \cdot \rho_{soil} \cdot \pi \cdot (D_{pile} - 2 \cdot wt_{pile})^2 \cdot L_{pile}^2 = 4.7 \cdot 10^6\,N$$

$$S_q = 1 + \sin(\theta_{soil})$$

$$N_q = \frac{1 + \sin(\theta_{soil})}{1 - \sin(\theta_{soil})} \cdot e^{\pi \cdot \tan(\theta_{soil})}$$

$$P_0 = L_{pile} \cdot \rho_{soil}$$

$$Q_c = S_q \cdot N_q \cdot P_0 = 1.6 \cdot 10^7\,N / m^2$$

$$A_{plug} = \frac{\pi}{4} \cdot D_{pile}^2 = 1.47\,m^2$$

$$F_{end} = Q_c \cdot A_{plug} = 2.3 \cdot 10^7\,N$$

$$F_{resistance} = \theta_{PE} \cdot \left(F_{outside} + F_{inside}\right) = 7.8 \cdot 10^6\,N \quad (since\ F_{inside} < F_{end})$$

$$F_{resistance} - F_{axial} = 8.6 \cdot 10^5\,N \rightarrow pass$$

Bibliography

ABS (2011). Design standards for Offshore Wind farms.
API (2000). Recommended Practice for Planning, Designing and Constructing Fixed Offshore Platforms. Working Stress Design.
API (2007). Working Stress Design. Recommended Practice for Planning, Designing and Constructing Fixed Offshore Platforms.
Bendat, J. S. and A. G. Piersol (1980). "Engineering applications of correlation and spectral analysis."
Bierbooms, W. (2002). DOWEC - Wind and wave conditions.
Brent, R. P. (1973). Algorithms for Minimization Without Derivatives.
DNV (2002). Guidelines for design of Wind Turbines.
DNV (2013). "Design of Offshore Wind Turbine Structures DNV-OS-J101."
Donkers, J. A. J. (2010). Update Offshore Wind Atlas - Implementing a variable sea surface roughness.
El-Reedy, M. A. (2012). Offshore structures - Design, Construction and Maintenance, Elsevier.
EWEA (2013). The European offshore wind industry - key trends and statistics 2012. A. Arapogianni.
EWEA (2014). "Wind energy factsheet."
FraunhoferISE (2012). Study - Levelized cost of electricity renewable energies.
Geotechdata. (2014). "Soil propperties." from http://www.geotechdata.info/.
Geotechdata. (2015). "Geotech." from http://www.geotechdata.info/index.html.
GL (2012). Guideline for the Certification of Offshore Wind Turbines.
GLrenewables (2012). "Guideline for the Certification of Offshore Wind Turbines."
IEC (2009). "International standard 61400."
Journée, J. M. J. and W. W. Massie (2001). Offshore hydromechanics, Delft University of Technology.
Lourens, E. M. (2014). OE5665 Offshore wind support structures - Monopile design 1. TU Delft.
Lourens, E. M. (2014). OE5665 Offshore wind support structures - Multi-member structures.
Muskulus, M. (2014). "Design Optimization of Wind Turbine Support Structures - A Review."
NREL (2009). "Definition of a 5MW Reference wind turbine for offshore system development."
Oceania (2012). Siesmic for Offshore Wind vs Seismic for Fossil Fuels.
Oord, v. (2014). OE5665 Offshore wind support structures - Soil-structure interaction, TU Delft.
Tempel, J. v. (2006). "Design of Support Structures for Offshore Wind Turbines."
Verruijt, A. (1999). Laterally Loaded Pile. Milieu-Effect Rapport Locatiekeuze Demonstratieproject Near Shore Windpark (in Dutch). Den haag, Ministerie van Economische Zaken.
Vugts, J. H. (2001). "Hydrodynamic loading on monotower support structures for preliminary design."
Vugts, J. H. (2002). Handbook of bottom founded offshore structures.
Zaaijer, M. B. (2013). Great expectations for offshore wind turbines. Doctoral, TU Delft.
Zaaijer, M. B. (2014). Introduction to wind energy practical session 5.